INTERACTION OF TWO-DIMENSIONAL NON-ISOTHERMAL COUNTER-FLOWING IMPINGING JETS IN A CHANNEL

ABSTRACT

THESIS

Submitted for the award of the degree of

Doctor of Philosophy

in

MECHANICAL ENGINEERING

By

SALEEM ANWAR KHAN

UNDER THE SUPERVISION OF

DR. NADEEM HASAN

DEPARTMENT OF MECHANICAL ENGINEERING
Z. H. COLLEGE OF ENGINEERING AND TECHNOLOGY
ALIGARH MUSLIM UNIVERSITY
ALIGARH (INDIA)

Abstract

A numerical investigation of interaction of non-isothermal counterflowing impinging jets / streams of different miscible fluids (same phase) in a 2D adiabatic channel in the mixed convection laminar flow regime, is carried out by treating the fluid as a binary mixture. It is concluded from the literature reviewed that the chosen problem has not been investigated earlier. Both thermal and intrinsic buoyancy have been considered through Boussinesq approximation. The two buoyancy forces give rise to thermal and intrinsic Richardson numbers, Ri_T and Ri_C, respectively as the important dimensionless numbers governing the problem. A semi-explicit pressure correction scheme with a finite difference type of discretization, on a structured colocated Cartesian mesh, has been employed for the purpose of the numerical study.

The geometry of the flow domain along with the dimensionless form of the governing equations and chosen boundary conditions, shows that the flow is dependent on eight dimensionless numbers / groups, namely, 1) Reynolds number, Re, 2) Thermal Richardson number, Ri_T, 3) Concentration Richardson number, Ri_C, 4) Prandtl number, Pr, 5) Schmidt number, Sc, 6) channel height, h, 7) half of channel length, ℓ and 8) Velocity ratio, VR. In order to obtain physically realizable solutions, the values of Pr and Sc are fixed at 0.7 and 0.8 respectively. The geometric parameters are kept fixed with h = 2 and ℓ = 100. The channel is taken long enough such that the effect of exit boundary conditions is not felt on the flow solutions. At a fixed Pr and Sc, the numerical simulations are carried out over a range of Ri_T and Ri_C spanning the interval [0– 1.5]. To examine the effect of difference of flow rate and momentum of the two jets, three different cases of velocity ratios, VR, are considered, typically, 0.5, 1 and 2. The present work focuses on both fundamental aspects of fluid flow as well as the practical

applications of jet mixing. Therefore, the objectives of the present study are to inspect the effect of change of Ri_T, Ri_C and VR on the flow dynamics as well as the thermal and physical mixing characteristics of the two streams.

The changes in the flow structure both in the spatial and the temporal domains, as the different parameters are varied, have been studied through two distinct methods of analysis. In the first approach, the computational data obtained from the numerical simulations is examined by generating the plots of streamline, isotherm pattern and iso-concentration patterns, profiles of temperature, concentration and velocity at different axial locations, wall-pressures and time histories of unsteady flows. In the second approach, proper orthogonal decomposition (POD) has been employed for unsteady flows, in order to identify the dominant structures. Several scalar meaures such as Mixing Indices, Mixing Lengths and Buoyancy Mixing Effectiveness are introduced and utilized to quantitatively characterize the the mixing characteristics.

For the range of parameters considered, the flows (steady as well as unsteady) always exhibit a symmetry about the mid-plane x = 0. This can be attributed to symmetry of boundary conditions and the absence of any symmetry breaking, oscillating or flapping jets / streams instabilities for the chosen set of parameters. The instability leading to a transition from a symmetric steady state to an asymmetric steady state for the forced flow at VR = 1, is *suppressed* by buoyancy and for unequal velocities of the two jets. Within the parametric range of the present study two different flow regimes are obtained–long term *steady flow* regime and *unsteady flow* regime having *oscillatory* behavior with vortex-shedding. Using Landau theory, it is established that the transition from steady to unsteady flow regime is a supercritical Hopf bifurcation. A complete regime map identifying the steady and unsteady flow regimes, within the parametric space of the present study, is obtained by plotting the neutral curves of Ri_C and Ri_T (obtained using

Landau theory) for different values of VR. Within the parametric domain of Ri_T and Ri_C, the bifurcation causing transition from steady to unsteady flow regime is found to be absent at VR = 0.5.

The instability associated with unsteady flows is of *convective type*, as the unstable perturbation or mode appears as a spatially growing disturbance *along the flow direction only*. POD analysis of the unsteady flows at VR = 1, establishes the presence of *standing* waves. The presence of degenerate pairs in the POD eigenspectrum confirms the presence of *travelling* waves in the unsteady flows at VR = 2. The space–time symmetry of the degenerate pair of modes is utilized to estimate the average translational wave speeds in unsteady regime at VR = 2.

In the context of the present problem, the physical action of the two buoyancy forces is to accelerate the two fluid streams as the direction of the net buoyancy force aids the fluid inertia. This is directly inferred from the observed trends in lengths of recirculation zones on the top and bottom walls. In the steady flow regime, for all velocity ratio cases, the thermal and concentration fields are approximately *reflectionally symmetric with respect to each other,* so that the dynamics is only weakly sensitive to the individual values of Ri_T and Ri_C for a given level of combined buoyancy, but is strongly controlled by the combined buoyancy ($Ri_T + Ri_C$).

The thermal and physical mixing process along *the channel length* can be effectively monitored by the scalar measure termed as 'mixing index' utilized in the present work. For the purpose of design and performance assessment of such mixing devices or systems a 'Mixing Length' parameter is proposed in the present work. The parameter is shown to be effective in characterizing the overall mixing process. In the steady flow regime, the mixing length is not very sensitive to the two Richardson numbers. For the unsteady periodic flow with standing waves (VR = 1), the mixing process is significantly enhanced

with the mixing lengths reducing by almost 70% at (Ri_T + Ri_C) = 3 with respect to the forced flow values. The formation of standing waves leads to a sinuous flow pattern with the fluid particles following a wavy path which greatly enhances the mixing of two streams. For unsteady cases involving the formation of travelling wave (VR = 2), the enhancement in mixing over the forced flow scenario is relatively less as compared to unsteady cases where standing wave is present (VR = 1).

A quantitative measure which quantifies the effectiveness of buoyancy, termed as 'Buoyancy Mixing Effectiveness' (e_m) is also proposed. For unsteady cases at VR = 1, both thermal and physical Buoyancy Mixing Effectiveness is almost 10 times than that for the steady cases. Increase in buoyancy in the unsteady regime, further enhances mixing and nearly 60 % increase in effectiveness at (Ri_T + Ri_C) = 3 as compared to (Ri_T + Ri_C) = 2, is observed at VR = 1.

INTERACTION OF TWO-DIMENSIONAL NON-ISOTHERMAL COUNTER-FLOWING IMPINGING JETS IN A CHANNEL

THESIS

Submitted for the award of the degree of

Doctor of Philosophy

in

MECHANICAL ENGINEERING

By

SALEEM ANWAR KHAN

UNDER THE SUPERVISION OF

DR. NADEEM HASAN

DEPARTMENT OF MECHANICAL ENGINEERING
Z. H. COLLEGE OF ENGINEERING AND TECHNOLOGY
ALIGARH MUSLIM UNIVERSITY
ALIGARH (INDIA)

Certificate

This is to certify that the thesis entitled **Interaction of Two-Dimensional Non-Isothermal Counter-Flowing Impinging Jets in a Channel** being submitted by **Saleem Anwar Khan** to the **Zakir Hussain College of Engineering and Technology, Aligarh Muslim University, Aligarh (India)** for the award of the degree of Doctor of Philosophy in **Mechanical Engineering Department** is a bonafide research work carried out by him under my supervision and guidance. The research reports and the results presented in this thesis have not been submitted in parts or in full to any other University or Institute for the award of any degree or diploma.

Nadeem Hasan, Ph. D.

Assistant Professor
Mechanical Engineering Department,
Z. H. College of Engg. & Tech.,
Aligarh Muslim University, Aligarh (India).

Acknowledgements

All praises be to Almighty *ALLAH,* (S. W. T.) who is the creator of all things and, who has given us brain to explore His mysterious and challenging world. And peace be upon His prophet *MUHAMMAD* (S. A. W.), who has shown us the right path to do so.

First and foremost, I offer my sincerest gratitude to my supervisor, **Dr. Nadeem Hasan**, who has supported me throughout my thesis with his patience, knowledge and providing appropriate suggestions as and when required. I attribute the level of my work to his encouragement and effort and without him this thesis, too, would not have been completed or written. The presentation of the work has been largely shaped by his expertise and experience. One simply could not wish for a better or friendlier supervisor.

I would like to express my deep sense of gratitude to *Dr. S. Mahdi. A. Rizvi*, Professor and Chairman, Mechanical Engineering Department, for extending all kinds of Departmental facilities required for the completion of the work. I am also thankful to Dr. Altamush Siddiqui, and Dr. Jamil Ahmad in particular, and other teaching staff of the department of Mechanical Engineering in general, for their valuable suggestions during the course of my research work. I am grateful to non-teaching staff of department of Mechanical Engineering, my colleagues and friends for their assistance in the compilation of the thesis.

I would like to take this opportunity to thank my parents for their cooperation and the support, especially in some difficult and testing times. A lot of thanks to my wife for standing by me in some difficult phases and, shouldering a lot of responsibilities of the family, thereby allowing me to concentrate on the research.

Saleem Anwar Khan

Abstract

A numerical investigation of interaction of non-isothermal counterflowing impinging jets / streams of different miscible fluids (same phase) in a 2D adiabatic channel in the mixed convection laminar flow regime, is carried out by treating the fluid as a binary mixture. It is concluded from the literature reviewed that the chosen problem has not been investigated earlier. Both thermal and intrinsic buoyancy have been considered through Boussinesq approximation. The two buoyancy forces give rise to thermal and intrinsic Richardson numbers, Ri_T and Ri_C, respectively as the important dimensionless numbers governing the problem. A semi-explicit pressure correction scheme with a finite difference type of discretization, on a structured colocated Cartesian mesh, has been employed for the purpose of the numerical study.

The geometry of the flow domain along with the dimensionless form of the governing equations and chosen boundary conditions, shows that the flow is dependent on eight dimensionless numbers / groups, namely, 1) Reynolds number, Re, 2) Thermal Richardson number, Ri_T, 3) Concentration Richardson number, Ri_C, 4) Prandtl number, Pr, 5) Schmidt number, Sc, 6) channel height, h, 7) half of channel length, ℓ and 8) Velocity ratio, VR. In order to obtain physically realizable solutions, the values of Pr and Sc are fixed at 0.7 and 0.8 respectively. The geometric parameters are kept fixed with $h = 2$ and $\ell = 100$. The channel is taken long enough such that the effect of exit boundary conditions is not felt on the flow solutions. At a fixed Pr and Sc, the numerical simulations are carried out over a range of Ri_T and Ri_C spanning the interval [0– 1.5]. To examine the effect of difference of flow rate and momentum of the two jets, three different cases of velocity ratios, VR, are considered, typically, 0.5, 1 and 2. The present work focuses on both fundamental aspects of fluid flow as well as the practical

applications of jet mixing. Therefore, the objectives of the present study are to inspect the effect of change of Ri_T, Ri_C and VR on the flow dynamics as well as the thermal and physical mixing characteristics of the two streams.

The changes in the flow structure both in the spatial and the temporal domains, as the different parameters are varied, have been studied through two distinct methods of analysis. In the first approach, the computational data obtained from the numerical simulations is examined by generating the plots of streamline, isotherm pattern and iso-concentration patterns, profiles of temperature, concentration and velocity at different axial locations, wall-pressures and time histories of unsteady flows. In the second approach, proper orthogonal decomposition (POD) has been employed for unsteady flows, in order to identify the dominant structures. Several scalar meaures such as Mixing Indices, Mixing Lengths and Buoyancy Mixing Effectiveness are introduced and utilized to quantitatively characterize the the mixing characteristics.

For the range of parameters considered, the flows (steady as well as unsteady) always exhibit a symmetry about the mid-plane x = 0. This can be attributed to symmetry of boundary conditions and the absence of any symmetry breaking, oscillating or flapping jets / streams instabilities for the chosen set of parameters. The instability leading to a transition from a symmetric steady state to an asymmetric steady state for the forced flow at VR = 1, is *suppressed* by buoyancy and for unequal velocities of the two jets. Within the parametric range of the present study two different flow regimes are obtained–long term *steady flow* regime and *unsteady flow* regime having *oscillatory* behavior with vortex-shedding. Using Landau theory, it is established that the transition from steady to unsteady flow regime is a supercritical Hopf bifurcation. A complete regime map identifying the steady and unsteady flow regimes, within the parametric space of the present study, is obtained by plotting the neutral curves of Ri_C and Ri_T (obtained using

Landau theory) for different values of VR. Within the parametric domain of Ri_T and Ri_C, the bifurcation causing transition from steady to unsteady flow regime is found to be absent at VR = 0.5.

The instability associated with unsteady flows is of *convective type*, as the unstable perturbation or mode appears as a spatially growing disturbance *along the flow direction only*. POD analysis of the unsteady flows at VR = 1, establishes the presence of *standing* waves. The presence of degenerate pairs in the POD eigenspectrum confirms the presence of *travelling* waves in the unsteady flows at VR = 2. The space–time symmetry of the degenerate pair of modes is utilized to estimate the average translational wave speeds in unsteady regime at VR = 2.

In the context of the present problem, the physical action of the two buoyancy forces is to accelerate the two fluid streams as the direction of the net buoyancy force aids the fluid inertia. This is directly inferred from the observed trends in lengths of recirculation zones on the top and bottom walls. In the steady flow regime, for all velocity ratio cases, the thermal and concentration fields are approximately *reflectionally symmetric with respect to each other,* so that the dynamics is only weakly sensitive to the individual values of Ri_T and Ri_C for a given level of combined buoyancy, but is strongly controlled by the combined buoyancy ($Ri_T + Ri_C$).

The thermal and physical mixing process along *the channel length* can be effectively monitored by the scalar measure termed as 'mixing index' utilized in the present work. For the purpose of design and performance assessment of such mixing devices or systems a 'Mixing Length' parameter is proposed in the present work. The parameter is shown to be effective in characterizing the overall mixing process. In the steady flow regime, the mixing length is not very sensitive to the two Richardson numbers. For the unsteady periodic flow with standing waves (VR = 1), the mixing process is significantly enhanced

with the mixing lengths reducing by almost 70% at (Ri_T + Ri_C) = 3 with respect to the forced flow values. The formation of standing waves leads to a sinuous flow pattern with the fluid particles following a wavy path which greatly enhances the mixing of two streams. For unsteady cases involving the formation of travelling wave (VR = 2), the enhancement in mixing over the forced flow scenario is relatively less as compared to unsteady cases where standing wave is present (VR = 1).

A quantitative measure which quantifies the effectiveness of buoyancy, termed as 'Buoyancy Mixing Effectiveness' (e_m) is also proposed. For unsteady cases at VR = 1, both thermal and physical Buoyancy Mixing Effectiveness is almost 10 times than that for the steady cases. Increase in buoyancy in the unsteady regime, further enhances mixing and nearly 60 % increase in effectiveness at (Ri_T + Ri_C) = 3 as compared to (Ri_T + Ri_C) = 2, is observed at VR = 1.

Contents

Acknowledgements ii

Abstract iii

Table of contents vii

List of figures ix

List of tables xii

Nomenclature xv

1 Introduction and literature review 1

1.1 Introduction 1

1.2 Previous Studies on Jet Impingement Interactions 4

1.2.1 Jet-Wall Impingement 4

A. *Forced Convection Regime* 5

B. *Mixed Convection Regime* 9

1.2.2 Jet-Jet Impingement 11

A. *Forced Convection Regime* 12

B. *Mixed Convection Regime* 17

1.3 Conclusions 18

1.4 Problem description 18

1.5 Objectives 20

1.6 Summary 20

2 Problem Formulation and Solution Methodology 22

2.1 Mathematical Formulation and the Governing equations 22

2.1.1 Boundary and initial conditions 26

2.2 Parametric Space 27

2.3 Numerical Scheme 28

2.3.1 Time integration 28

A. *Predictor step* 29

B. *Corrector step* 30

2.3.2 Spatial discretisation 32

2.4 Validation 33

2.5 Summary 36

3 Flow Dynamics and Mixing Characteristics at VR = 1 39

3.1 Numerical Aspects 39

3.2 Forced Flow 42

3.3 Buoyancy Effects 44

3.3.1 Flow regimes 46

3.3.2 Steady flow dynamics 51

3.3.3 Unsteady flow dynamics 58

A. *Spatio-temporal data analysis* 58

B. *POD Analysis* 67

3.3.4 Mixing Characteristics 73

3.4 Summary 80

4 Effect of Velocity Ratio on Flow Dynamics and Mixing 84

4.1 Forced Flow 84

4.2 Buoyancy Effects 86

4.2.1 Flow regimes 87

4.2.2 Steady flow dynamics 89

4.2.3 Unsteady flow dynamics 96

A. *Spatio-temporal data analysis* 96

B. *POD Analysis* 103

4.2.4 Mixing Characteristics 108

4.3 Summary 113

5 Conclusions and recommendations 116

5.1 Spatio-temporal flow dynamics 117

5.2 Mixing characteristics 120

5.3 Recommendations for further study 122

References 124

Appendix A 132

List of figures

Figure	Figure caption	Page
1.1	Jet Interaction with Solid Surface	2
1.2	Jet Interaction with Fluid	2
1.3	Parallel Jets	2
1.4	Co-axial Jets	2
1.5	Jets in Cross-flow	3
1.6	Jet-Wall Impingement	4
1.7	Confined Jet-Jet impingement	4
1.8	Generic configuration of a counter-flowing jet interaction in a 2-D rectangular channel	19
2.1	A magnified view of 325 × 129 mesh employed for validation studies	34
2.2	Steady state streamline patterns for a) Re= 100, h = 2 b) Re = 250, h = 4	35
2.3	a) Velocity profiles at (Re= 100, h = 2) and b) Wall Nusselt number at (Re = 250, h = 4) along with the numerical data of Ref. [37]	36
3.1	Comparison of unsteady mean u-velocity profiles for different exit boundary locations at a) x = 3.0, b) x = 10 and c) x = 60 at (Ri_T = 1.5, Ri_C = 0.5)	40
3.2	Comparison of steady state u-velocity profiles for different choice of grids at a) x =3.0, b) x = 10 and c) x = 60 for (Ri_T = 0.5, Ri_C = 0.2)	41
3.3	The steady state streamline pattern for the forced flow for a) short times (unstable), b) large times (stable) and c) the time history of u(-15.56, 0) at (Re = 200, h = 2.0)	43
3.4	Variation of square of equilibrium amplitudes of the periodic data of u(-15.56, 0) with the control parameter Ri_T in the neighborhood of bifurcation at Ri_C = 0.5	49
3.5	Regime map showing the different flow regimes and the neutral curve	50

3.6	The a) steady state streamline patterns and b) axial velocity profiles at $Ri_T = 0.5$, $Ri_C = 1$ (left) and $Ri_T = 1$, $Ri_C = 0.5$ (right)	51
3.7	Steady state a) Isotherm patterns and b) Iso-concentration patterns for $Ri_T = 0.5$, $Ri_C = 1$ (left) and $Ri_T = 1$, $Ri_C = 0.5$ (right) respectively	53
3.8	Steady state a) temperature and b) concentration profiles for $Ri_T = 0.5$, $Ri_C = 1$	54
3.9	Steady state a) temperature and b) concentration profiles for $Ri_T = 1$, $Ri_C = 0.5$	55
3.10	Variation of upper-wall pressure for steady flow cases at different combinations of Ri_T and Ri_C	56
3.11	Time history of u (-15.56, 0) at ($Ri_T = 1$, $Ri_C = 1.5$) and ($Ri_T = 1.5$, $Ri_C = 1$)	59
3.12	Mean flow streamline patterns at a) $Ri_T = 1$, $Ri_C = 1.5$, b) $Ri_T = 1.5$, $Ri_C = 1$	59
3.13	Mean flow isotherm patterns at a) $Ri_T = 1$, $Ri_C = 1.5$, b) $Ri_T = 1.5$, $Ri_C = 1$	60
3.14	Mean flow iso-concentration patterns at a) $Ri_T = 1$, $Ri_C = 1.5$, b) $Ri_T = 1.5$, $Ri_C = 1$	60
3.15	Mean flow profiles of a) temperature and b) concentration c) u-velocity at $Ri_T = 1$, $Ri_C = 1.5$	61
3.16	Mean flow profiles of a) temperature and b) concentration and c) u-velocity at $Ri_T = 1.5$, $Ri_C = 1$	62
3.17	Mean flow a) streamline, b) isotherms and c) iso-concentration patterns at $Ri_T = 1.5$, $Ri_C = 1.5$	63
3.18	Instantaneous streamline patterns over one temporal cycle of oscillations at $Ri_T = 1$, $Ri_C = 1.5$	64
3.19	a) Time history of u (+0.90, 0) and b) the instantaneous v-velocity along channel centerline at different instants of time	65
3.20	Variation of mean upper-wall pressure for different combinations of Ri_T and Ri_C in unsteady flow regime	66
3.21	The POD eigenspectrum obtained from the unsteady fluctuating field data for ($Ri_T = 1.0$, $Ri_C = 1.5$)	71
3.22	The (a) temporal and (b) spatial structure of the leading three POD modes at ($Ri_T = 1$, $Ri_C = 1.5$)	72

3.23	Comparison between bulk based and simple average based normalized mixing index for a) temperature and b) concentration for the forced flow	74
3.24	The impact of buoyancy on a) thermal and b) physical mixing characteristics for both steady and unsteady cases	75
3.25	a) Temperature and b) concentration normalized mixing lengths at different combinations of Ri_T and Ri_C	78
4.1	The time history of u(-15.56, 0) at (Re = 200, h = 2.0) for VR =0.5, 1 and 2	85
4.2	Forced flow steady state streamline plots for a) VR = 0.5, b) VR = 2 and c) VR = 1	85
4.3	Steady state lower wall pressure plots for forced flow at VR = 0.5, 1 and 2	86
4.4	Regime map showing the different flow regimes and the neutral curve at VR = 1 and 2	88
4.5	The streamline patterns at $Ri_T = 0.5$, $Ri_C = 1.0$ for a) VR = 0.5, b) VR = 2 and c) VR = 1	89
4.6	The a) streamline patterns and b) u-velocity profiles at different axial locations at $Ri_T = 1$, $Ri_C = 0.5$ for VR = 0.5 (left) and VR = 2 (right)	90
4.7	Steady state a) Isotherm patterns and b) Iso-concentration patterns at $Ri_T = 0.5$, $Ri_C = 1$ for VR = 0.5, VR = 2 and VR = 1 respectively	92
4.8	Steady state temperature (left) and concentration (right) profiles respectively for a) VR = 0.5, b) VR = 2 and c) VR = 1 at $Ri_T = 0.5$, $Ri_C = 1$	93
4.9	Variation of steady state a) upper-wall and b) lower-wall pressures at $Ri_T = 1$ and $Ri_C = 0.5$ at different VRs	94
4.10	Time history of u (-15.56, 0) at ($Ri_T = 1$, $Ri_C = 1.5$) for VR = 0.5, 2 and 1	96
4.11	Mean flow patterns as represented by a) streamlines, b) isotherms and c) iso-concentration for VR = 2 (left) and VR = 1 (right) respectively at $Ri_T = 1$ and $Ri_C = 1.5$	97
4.12	Mean flow patterns for a) streamlines, b) isotherms and c) iso-concentration for VR = 2 at $Ri_T = 1.5$ and $Ri_C = 1$	98
4.13	Instantaneous streamline patterns over one temporal cycle for VR = 2 at $Ri_T = 1$, $Ri_C = 1.5$	99

4.14 a) Time history of u (+0.90, 0) and b) the instantaneous v-velocity along channel centerline at different instants of time at Ri_T = 1, Ri_C = 1.5 100

4.15 Mean a) temperature, b) concentration and c) u-velocity profiles for VR = 2 (left) and VR = 1 (right) at Ri_T = 1, Ri_C = 1.5 101

4.16 Variation of mean a) upper-wall and b) lower-wall pressures at Ri_T =1 and Ri_C = 1.5 at VR = 1 and 2 102

4.17 The POD eigenspectrum obtained from the unsteady fluctuating field data for VR = 2 at Ri_T = 1.0, Ri_C = 1.5 103

4.18 The (a) temporal and (b) spatial structure of the leading three POD modes for VR = 2 at (Ri_T = 1, Ri_C = 1.5) 104

4.19 The time evolution of temporal coefficients of degenerate pairs of modes for VR = 2 at Ri_T = 1, Ri_C = 1.5 105

4.20 The spatial structures of the contributions of pairs of POD modes having equal eigenvalues to the temperature field at τ = 3326.30 at Ri_T = 1 and Ri_C = 1.5 105

4.21 Spatial structure degenerate of the temperature eigenfunctions a) ($\psi_T^{(1)}$, $\psi_T^{(2)}$) and (b) ($\psi_T^{(3)}$, $\psi_T^{(4)}$) in the x-direction along the channel centreline 106

4.22 Thermal (left) and physical (right) normalized mixing indices for a) (Ri_T = 0, Ri_C = 0), b) (Ri_T = 1, Ri_C = 0) and c) (Ri_T = 1, Ri_C = 1.5) at VR = 0.5, 1 and 2 108

4.23 a) Temperature and b) concentration normalized mixing lengths at Ri_T = 0.5 for different VRs 111

4.24 a) Temperature and b) concentration normalized mixing lengths at Ri_T = 1.5 for different VRs 111

List of tables

Table	Table captions	page
3.1	Various grids along with minimum and maximum spacing used in grid independence study	41
3.2	Statistics for the linear fit $A_e^2 = a + b(\textbf{control parameter})$ and the determination of points on the neutral curve in (Ri_C - Ri_T) plane	50
3.3	Summary of the salient features of the observed flow patterns for the steady flow cases	57
3.4	Summary of the salient flow features for the unsteady flow regime	66
3.5	Convergence of leading POD eigenvalues with increasing number of snapshots in the data ensemble for Ri_T =1, Ri_C = 1.5	70
3.6a	Thermal and physical mixing lengths for different combinations of Ri_T and Ri_C in the steady flow regime	76
3.6b	Thermal and physical mixing lengths for different combinations of Ri_T and Ri_C in the unsteady flow regime	77
3.7a	Thermal and physical buoyancy mixing effectiveness for different combinations of Ri_T and Ri_C in the steady flow regime	79
3.7b	Thermal and physical buoyancy mixing effectiveness for different combinations of Ri_T and Ri_C in the unsteady flow regime	79
4.1	Separation lengths of recirculation zones for VR = 0.5, 1 and 2 within the steady flow regime	95
4.2	Comparison of the salient features of the flow patterns in the unsteady flow regime at VR = 1 and 2	103
4.3	Average phase speeds of the travelling waves (x-direction) at different y locations in the channel for different (Ri_T, Ri_C), combinations	107
4.4	Thermal and physical mixing lengths for different combinations of Ri_T and Ri_C for unsteady flow regime at VR = 0.5, 1 and 2	109
4.5	Thermal and physical mixing lengths for different combinations of Ri_T and Ri_C for steady flow regime at VR = 0.5, 1 and 2	110
4.6	Thermal and physical buoyancy mixing effectiveness for different combinations of Ri_T and Ri_C in the steady flow regime at VR = 0.5, 1 and 2	112

4.7 Thermal and physical buoyancy mixing effectiveness for different combinations of Ri_T and Ri_C in the unsteady flow regime at VR = 1 and 2 113

Nomenclature

A = amplitude of unstable perturbation associated with Landau equation

A_e = equilibrium amplitude associated with Landau equation

$\mathbf{B}$ = real symmetric square matrix associated with POD eigenvalue problem

B_{ij} = components of real square matrix $\mathbf{B}$

C = concentration or mass fraction of fluid 2 in the binary mixture

$\overline{C}$ = non-dimensional concentration, $\overline{C} = C - C_o$

$\bar{c}$ = average translational wave speed

D = jet / inlet stream width

D_{12} = binary diffusion coefficient of fluid 1 w.r.t 2

$E_{i,j}$ = aggregate of convective and diffusive terms in mass transport equation

e_m = buoyancy mixing effectiveness

$F_{i,j}$ = aggregate of convective and diffusive terms in energy transport equation

$G_{i,j}$ = aggregate of convective and diffusive terms in y-momentum equation

Gr = Grashof number

g = acceleration due to gravity

H = channel height

$H_{i,j}$ = aggregate of convective and diffusive terms in x-momentum equation

h = non-dimensional channel height, $h = \frac{H}{D}$

$\bar{h}_b$ = bulk based convective heat transfer coefficient

k = thermal conditivity

L = half channel length

L_m = non-dimensional mixing length

ℓ = non-dimensional half channel length, $\ell = \frac{L}{D}$

l_u = Landau constant

Le = Lewis number, $Le = \frac{Sc}{Pr}$

M = number of snapshots

MI(x) = bulk based mixing index at a axial location, x

$\langle MI \rangle$ = normalized mixing index, $\langle MI \rangle = \frac{MI(x)}{MI(0)}$

Nu_b = bulk based Nusselt number, $Nu = \frac{2H\overline{h_b}}{k}$

Nu_p = bulk based fully developed poiseuille flow Nusselt number for laminar flow

n = normal direction

P = non-dimensional pressure, $P = \frac{\overline{p} - \overline{p_o}}{\rho_o U^2}$

$\overline{p}$ = pressure

p' = pressure correction

p, q = POD modal quantum numbers

Pr = Prandtl number, $Pr = \frac{\nu_o}{\kappa_o}$

Re = bulk mean Reynolds number, $Re = \frac{UD}{\nu_o}$

Re_j = Hydraulic width based Reynolds number, $Re_j = 2\ Re$

Ri = Richardson number, = Gr/Re^2

Ri_T = thermal Richardson number, $Ri_T = \frac{g\beta_{mT}\Delta T D}{U^2}$

Ri_C = concentration Richardson number, $Ri_C = \frac{g\beta_{mC}D}{U^2}$

r = coordinate in radial direction

s_1, s_2 = Scaling factor associated with eigenvalues

Sc = Schmidt number, $Sc = \frac{\nu_o}{D_{12}}$

T = temperature

U = mean or bulk velocity of jet, $U = (U_1 + U_2)/2$

U = POD data ensemble

u, v = dimensionless Cartesian Velocity components along x and y directions respectively

$\bar{u}$ = guessed u-velocity

$\bar{\bar{u}}$ = average u-velocity

u' = u-velocity correction

$\bar{v}$ = guessed v velocity

v' = v-velocity correction

v_i = inlet jet velocity, $v_i = \frac{3U_i}{U_1(1+U_2/U_1)}(1-4x^2)$

VR = velocity ratio, $\frac{U_1}{U_2}$

x, y = non-dimensional Cartesian coordinates

Z = eigenvector of algebraic POD eigenvalue problem

Greek symbols

α = coefficient of thermal diffusivity

β = coefficient of volume expansion

γ = Jet inclination w. r. t. impingement surface normal

ξ = flow control parameter

λ = Eigenvalue

σ = growth rate of amplitude

ϕ = fluid property

$\bar{\phi}$ = average fluid property

ϕ_B = bulk based fluid property

ψ = POD basis function

ν = kinematic viscosity

θ = non-dimensional temperature, $\theta = \frac{T - T_o}{\Delta T}$

ρ = binary mixture density

τ = non-dimensional time, $\tau = \frac{D}{U}$

κ = thermal diffusivity

Subscripts / Superscripts

C = concentration

c = critical

i = number of snapshots

m = mean property associated with two fluid streams

n = time instant

o = reference state mean temperature and concentration

T = temperature

1 = property associated with pure fluid 1

2 = property associated with pure fluid 2

" = properties related to fluctuating flow field

Chapter 1

Introduction and Literature Review

In this chapter the generic problem of opposed jet impingement in enclosures is introduced. Section 1.1 discusses in brief the various jet interactions that have been the subject of research in the past years. In §1.2, previous studies related to various types of jet impingement interactions are reported. The conclusions drawn from the review of previous studies on jet impingement interactions are presented in §1.3. The problem chosen in the present investigation is described in §1.4. Finally, in §1.5, various objectives of the present study are enumerated.

1.1 Introduction

Study of jets is important in the field of fluid mechanics due to its wide application in daily life as well as in industries. Jets are a class of flows known as *free shear flows*, and can be defined as an efflux of high velocity fluid forced out of a small-diameter opening or nozzle. The surrounding is assumed to be made up of the same fluid as the jet itself, and sometimes, this ambient fluid is carried along with the jet by the viscous drag at the outer edge of the jet. The process of drawing in the surrounding fluid from the sides of the jet by frictional forces is called *entrainment.* A special class of problem involving one or more jets is: *Jet Interaction.* Jet interactions with its surroundings may be broadly classified as,

(i) Shear interactions,

(ii) Cross-flow interactions,

(iii)Impingement interactions.

Shear interactions originate in the form of tangential discontinuities (both kinematic and thermal) between the jet and its surroundings. The jet interacting with solid is known

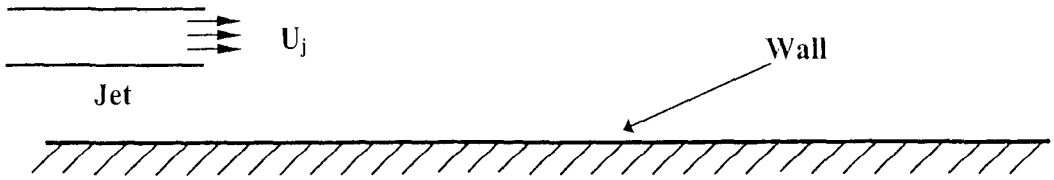

Fig. 1.1: Jet Interaction with Solid Surface

as a wall jet (Fig. 1.1). The examples of such class of problem are boundary layer control and lift enhancement on airfoils by making use of wall jet tendency to adhere to surfaces (Coanda effect), windshield defroster system in automobiles, cooling and protecting surfaces (turbine blades and combustion chamber walls) from hot and/or corrosive fluids, the cooling of the outer surfaces in high-speed vehicles or rockets.

Another type of interaction is jet fluid (stagnant or moving) interaction. The other fluid can be any stream (Fig. 1.2), another jet, both parallel (Fig. 1.3) and coaxial (Fig. 1.4).

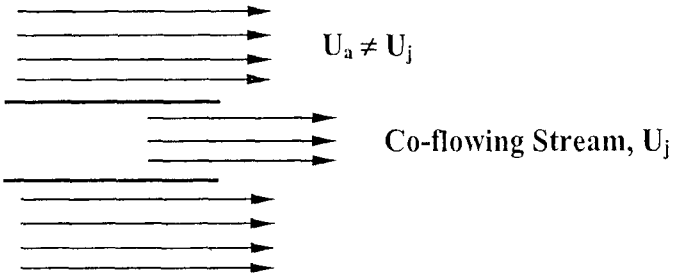

Fig. 1.2: Jet Interaction with Fluid

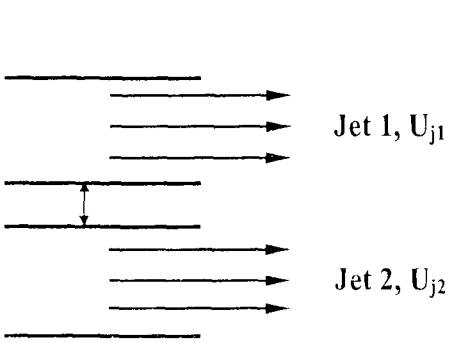

Fig. 1.3: Parallel Jets

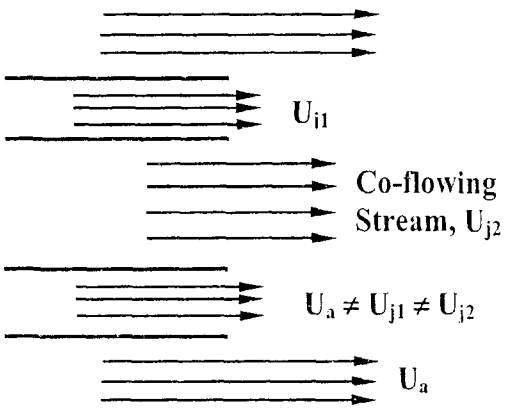

Fig. 1.4: Co-axial Jets

Examples of such type of jet interactions are seawater flowing from an adjacent tank in the form of a jet impinging on a thin residual layer of fuel in fuel tank of ships, mixing between fuel and air using a row of combustor jets in power boilers, use of multiple jets to give improved propulsion and noise level in vertical or short distance take off and landing of planes, use of multiple arrays of parallel jets for enhancement of cooling in electronic components, etc. Also coaxial jets are used in combustion chambers, jet pumps, mixing tanks, cooling systems, and premixed burners, etc.

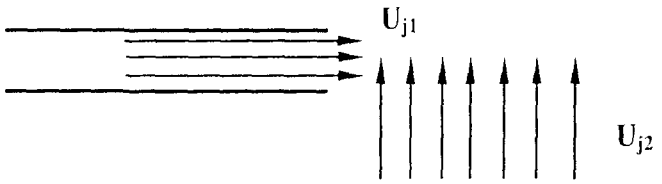

Fig. 1.5: Jets in Cross-flow

Cross-flow jet interactions are observed when a jet of fluid mixes with a stream of fluid moving in a direction normal to the direction of the jet (Fig. 1.5). These interactions can take place in unconfined, semi-confined and fully confined geometries. The diverse applications of impinging jets in a cross-flow are cooling of the metal sheets, tempering of glass, environmental flow problems, gas turbine combustors, film cooling of turbine blades, drying of paper and textiles, V-STOL planes with vertical takeoff, waste disposal into water bodies and atmosphere etc.

Jet Impingement is a special case of jet interaction in which a jet impinges on a solid boundary or another jet. For clear distinction the former is referred to as ***Jet-wall impingement (Fig. 1.6)*** while the latter is referred to as ***Jet-jet impingement (Fig.1.7)***. While jet-wall impingement can take place only in unconfined and semi-confined domains, jet-jet impingement can be found to take place in unconfined, semi-confined and completely confined geometries. Some applications of jet-wall impingement are in annealing of metal, tempering of glass, drying of textiles, cooling of turbine blades and

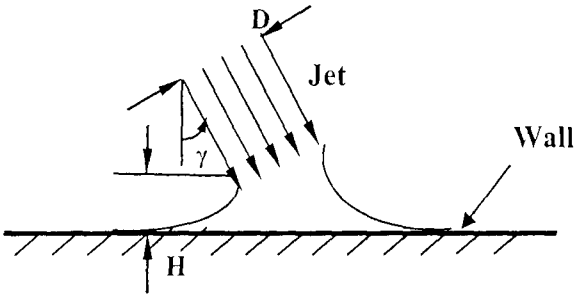

Fig. 1.6: Jet-Wall Impingement

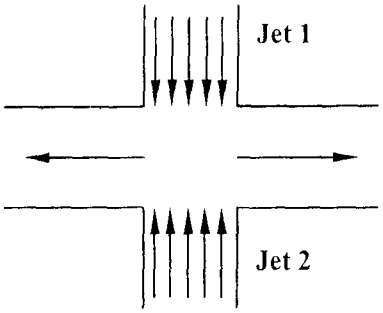

Fig. 1.7: Confined Jet-Jet impingement

cooling of electronic components etc. Similarly some applications in which jet-jet interaction taking place are fluid and thermal mixers in process industries, opposed jet reactors for chemical kinetic studies and nano-particle synthesis, side dump combustors, polymer processing etc.

1.2 Previous Studies on Jet Impingement Interactions

1.2.1 Jet-Wall Impingement

Impinging jets have, most commonly, been exploited to the enhancement of heat and mass transfer that occurs in the form of impingement surface heating and cooling in applications featuring fairly high heat fluxes. Apart from impingement heat transfer, the shear induced along the surface by jet impingement provides the impetus for several important technologies including surface cleaning [1] and jet stripping [2, 3] in which gas jets are used to control liquid coating thickness. The induced shear could also be utilized for characterization of adhesive strength in powder coatings [4] or trace particulate residues [5] for subsequent surface sampling and chemical analysis.

Of the studies related to jet impingement heat transfer, most of the reported work is on forced convection regime and very few studies are available where the effect of buoyancy on flow dynamics and heat transfer has been taken into account.

A. Forced Convection Regime

Local transfer rates under single unconfined turbulent slot jets were first reported by Gardon and Akfirat [6, 7]. The potential flow solution coupled with a numerical solution of the boundary-layer equations was used to evaluate the local friction factor and Nusselt number of an impinging laminar jet with a uniform velocity profile at exit by Miyazaki and Silberman [8]. The heat-mass transfer analogy was used to convert the mass-transfer results into the heat transfer counterparts by Sparrow and Wong [9]. It was found that the shape of the velocity profile at the jet exit had a significant effect on the heat transfer characteristics of the impingement surface.

The effects of suction and nozzle exit velocity profile on the flow and heat transfer characteristics of a semi-confined laminar impinging slot-jet was studied by Van Heiningen et al. [10]. Uniform suction at the impingement surface was shown to enhance the heat transfer rates by a constant amount. The stagnation heat-transfer rate for a parabolic inlet velocity profile was calculated to be 1.5-2.0 times the value produced by a flat velocity profile. On a flat surface covered with a swollen polymer coating, a holographic interferometry technique was utilized to measure the mass-transfer coefficients for an impinging slot laminar air jet in study taken up by Masliyah and Nguyen [11]. The local Sherwood number was correlated to jet Reynolds number and distance along the surface.

Using finite-difference procedure, the laminar boundary-layer flow for a slot-jet impinging on an inclined flat plate, was investigated by Garg and Jayaraj [12]. It was

found that the local Nusselt number and skin friction coefficient could attain large values close to the stagnation point at small angles of impingement.

An experimental study on heat transfer behaviours of a confined slot jet impingement was systematically performed by Lin et. al. [13]. The parametric effects of jet Reynolds numbers (Re = 190-1537) and jet separation distance (H / D = 1-8) (refer Fig. 1.6) on heat transfer characteristics of the heated target surface were explored. It was shown that the effect of jet separation distance was not significant on stagnation, local and average Nusselt numbers. While the heat transfer increased with increasing jet Reynolds number.

An experimental study was performed to determine the effect of inclination of an impinging two-dimensional air jet on the heat transfer from a uniformly heated stainless steel flat plate having same width as the jet nozzle by Beitelmal et. al. [14]. Local Nusselt numbers were determined as a function of three parameters: (a) inclination angle (90°- γ) of the air jet relative to the plate in the range of 90°-40°, (b) nozzle exit-to-plate spacing (H / D) in the range of 4-12 and (c) Reynolds number based on the hydraulic diameter of the slot nozzle in the range of Re (4000-12000). The location of the maximum heat transfer region appeared to fall between 0 and 3D uphill (of inclined plate) from the geometrical impingement point, and was found to be insensitive to the Reynolds number in the range used in that study. For low values of inclination angle, the local Nusselt number on the uphill side from the maximum heat transfer point was insensitive to jet exit-to-plate spacing. Correlations were proposed to predict the local Nusselt number as a function of geometric parameters and flow Reynolds number.

Chung and Luo [15] studied unsteady heat transfer caused by confined impinging jet using DNS. The simulations were carried out for three Reynolds numbers (Re=300, 500, 1000) and two nozzle-to-plate distances (4 and 10). The instantaneous flow fields and heat transfer distributions were found to be highly unsteady and oscillatory in nature,

even at relatively low Reynolds numbers. It was shown that the fluctuations in the stagnation heat transfer were mainly caused by impingement of the primary vortices originating from the jet nozzle exit. The quasi-periodic nature of the generation of the primary vortices due to the Kelvin-Helmholtz instability was behind the nearly periodic fluctuation in impingement heat transfer, although more chaotic and nonlinear fluctuations were observed with increasing Reynolds numbers. The Nusselt number distribution away from the impingement point, on the other hand, was influenced by the secondary vortices which are generated due to the interaction between the primary vortices and the wall jets. The unsteady vortex separation from the wall in the higher Reynolds number cases led to a local minimum and a secondary maximum in the Nusselt number distribution. These were due to the changes in the thermal layer thickness accompanying the unsteady flow structures.

A numerical investigation of the effect of thermo-physical properties of fluid on heat transfer and the effect of the fluid Prandtl number on heat transfer under a semi-confined laminar slot jet was taken up by Shi et. al [16]. The fluid Prandtl number ranged from 0.71 to 71. Local, stagnation and average values of the impingement Nusselt number as well as the heat transfer coefficient distributions were reported. Empirical correlations were derived for the stagnation and average Nusselt number as a function of the fluid Prandtl number. The effects of nozzle-to-target spacing, H / D and jet Reynolds number on heat transfer were also reported.

A numerical investigation to examine the effects of geometric parameters on the confined impinging jet heat transfer was performed by Lou et. al. [17]. The effect of various parameters such as Nusselt number, Reynolds number, D / H was studied. Nozzle width D was varied from 0.6 mm to 2 mm, and nozzle-to-plate spacing H ranged from 0.5 mm to 10 mm. The jet flow was laminar with Reynolds number varying from 26.8 to

1000. The distribution of target surface temperature, local and average Nusselt number on the target plate was reported. Pressure drop for different D / H was also obtained.

The effects of jet plate size and plate spacing (jet height) on the heat transfer characteristics for a confined circular air jet vertically impinging on a flat plate were investigated by San and Shiao [18]. A heated plate was at constant heat flux of 1000 W/m^2. Jet Reynolds number (Re) was kept in the range 10,000–30,000 and plate spacing-to-jet diameter ratio (H / D) was in the range 1–6. Eleven jet plate width-to-jet diameter ratios in the range of 4.17–41.7 and seven jet plate length-to-jet diameter ratios in range of 5.5–166.7 were considered. The measured data were correlated into a simple equation.

A confined axisymmetric turbulent air jet laden with fluorescent solid particles of 5.0 μm diameter was impinged on a flat surface at Re = 10^4, and the total particle deposition efficiency and spatial distribution were measured experimentally using fluorometry and imaging techniques and also simulated numerically for different nozzle-to-surface distances by Burwash et. al. [19]. Three dimensionless distances from the nozzle's exit to the impaction surface, H / D = 2, 4, and 6, were investigated. It was observed that although having similar total deposition efficiencies (16.5–17.8%), shorter nozzle to surface distances (H / D = 2 and 4) showed a more pronounced ring-like radial deposition pattern around the stagnation point. These shorter distances also exhibit significantly lower particle deposition near the stagnation point when compared to the longer distance (H / D = 6). Numerical simulation performed showed that the particle deposition was dominated by a turbulent dispersion mechanism for H / D = 2, with inertial impaction became more important for the H / D = 4 and 6 cases.

Numerical study of impinging jets was performed with 13 widely spread Reynolds-averaged Navier-Stokes (RANS) turbulence models using commercial CFD software by Hofmann et. al. [20]. The only model able to predict correctly the laminar–turbulent

transition occurring at small nozzle-to-plate distance was the SST k-ω model (''transitional flow option''). Most of the other models can only satisfactorily predict heat transfer in the turbulent wall jet region. When the SST k-ω model with transitional flow option was applied for calculation of pulsating jets, the tendencies were predicted correctly.

B. Mixed Convection Regime

By using finite-difference numerical calculations, Yuan et al. [21] presented the effect of buoyancy on a laminar slot-jet impinging on a flat surface. For high Richardson numbers, both, buoyancy assisted and retarded flows were shown to have significant effects on the enhancement and mitigation, respectively, of the local Nusselt number.

The heat transfer and flow characteristics, of a single circular laminar impinging jet, including buoyancy force in a comparatively narrow space with a confined wall was studied by Ichimiya and Yamada [22]. Temperature distribution and velocity vectors in the space were obtained numerically by solving three-dimensional governing equations for the Reynolds number *Re* (= 400–2000) and the dimensionless space, h (= 0.25–1.0). After impingement, heat transfer behaviour on the impingement surface was divided into a forced convection region, a mixed convection region, and a natural convection region in the radial direction. The local heat flux corresponding to these three regions was visualized using a thermosensitive liquid crystal. Moreover, with the increase in Reynolds number, *Re,* and dimensionless space, *h*, the recirculation flow on the impingement surface moved downstream and its volume increased correspondingly. The Nusselt number averaged from $r = 0$ to the minimum point of peripherally averaged Nusselt number was computed as a function of Re and h.

The flow and heat transfer characteristics in the cooling of a heated surface by impinging slot jets in mixed convective regime was investigated numerically by Sahoo and Sharif [23]. Computations were done for vertically downward-directed two-dimensional slot jets impinging on a hot isothermal surface at the bottom and confined by a parallel adiabatic surface on top. Some computations were also performed where the jet was vertically upward, with an impingement plate at the top. The computed flow patterns and isotherms for various domain aspect ratios (4–10) and for a range of jet exit Reynolds numbers (100–500) and Richardson numbers (0–10) were analysed to understand the mixed-convection heat transfer phenomena. The local and average Nusselt numbers and skin friction coefficients at the hot surface for various conditions were presented. It was observed that for a given domain aspect ratio and Richardson number, the average Nusselt number at the hot surface increased with increasing jet exit Reynolds number. On the other hand, for a given aspect ratio and Reynolds number, the average Nusselt number did not change significantly with Richardson number, indicating that the buoyancy effects were not very significant in the overall heat transfer process for the range of jet Reynolds number considered in that study. Also, for the same problem configuration, the average Nusselt number did not change significantly when the jet was moving upward or downward.

Results of numerical simulation of the flow and heat transfer characteristics for a semi-confined cluster of laminar air jets impinging normally on a plane wall were reported by Zhao et. al. [24]. A central jet was surrounded by four equally spaced jets of the same configuration. Both circular and noncircular nozzles were considered. The effect of nozzle cross-section was displayed in the static pressure, temperature, and local Nusselt number contours on the impingement surface only for relatively short nozzle-to-surface distances. The heat transfer characteristics and performance of circular and

noncircular nozzles were compared. It was observed that the Nusselt number based on property values at the jet temperature was relatively insensitive to the temperature difference between the jet and the impingement surface. Also, the local Nusselt numbers were independent of the thermal boundary condition; i.e., the values were nearly the same for both isothermal and uniform heat flux conditions at the target surface.

1.2.2 Jet-Jet Impingement

When two counter-flowing jets / streams of different fluids (same phase) strike each other, a three-fold interaction, involving mixing of mass, momentum and energy, takes place. This generic phenomenon possesses diverse applications which were mentioned in detail by Tamir [25]. From the design point of view, the main objective is to develop an understanding and correlation of the mixing process with the operating variables like, flow rates, geometry parameters and fluid properties. This would in turn assist in optimization of the designs with respect to the operating variables. From the fundamental point of view, owing to the complex three-fold interactions, the flow physics is complicated and the sensitivity of flow patterns with the various operating parameters needs to be explored in order to establish a rational basis for designing flow systems involving such scenarios.

Turbulence is a favourable phenomenon for mixing. Many works related to turbulent opposed jet impingement have been reported in literature. But, although jet mixing is favored by turbulence, mixing of laminar jets also find numerous applications. In *Reaction Injection Moulding (RIM)* two opposed jets interact with each other in a cylindrical chamber. Jet Reynolds number in *RIM* is based on injector diameter and injector fluid properties usually lies in the range 100-500. At this low Reynolds number

no turbulence occurs as reported by Erkoç et. al. [26]. So the mixing of jets in *RIM* is in the laminar flow regime.

Miniaturization is the recent trend in analytical chemistry and life sciences. In the past two decades, miniaturization of fluid handling and fluid analysis has been emerging in the interdisciplinary research field of *microfluidics. Microfluidic* applications cover micro arrays, DNA sequencing, sample preparation and analysis, cell separation and detection, as well as environmental monitoring. The concept of *lab-on-chip* which is based on *microfluidics* is gaining popularity both in industry and academia, because of its potentials and advantages: small amounts of sample and reagent, less time consumption, lower cost and high throughput. Micro-pump and micro-mixer are two important components in a *microfluidic system.* Because of the small size of micro-mixers, the interacting jet Reynolds number is usually in laminar regime, although a few studies of turbulent jet mixing have also been reported for reacting jets as given by Kakuta et. al. [27].

An altogether new dimension is added to the interaction of opposed jets / streams in the form of heat transfer if the streams are of unequal temperatures. Further, depending on the operating conditions in such systems, the associated heat transfer may be of forced or mixed type. The published literature is mostly in the forced convection regime with few studies in the mixed convection regime.

A. Forced Convection Regime

Studies in the past involving counter-flowing impinging jets / streams in laminar regime have revealed that the stagnation flows resulting from their interactions are susceptible to instabilities leading to oscillatory and even chaotic flows. For the class of problem under consideration, most of the earlier studies have focused on isothermal

interaction of jets / streams. One of the earliest attempts to understand the isothermal interaction of opposed jets of similar fluids was made by Denshchikov et al. [28, 29]. They carried out an experimental investigation with opposed streams of water submerged in water. It was shown that the jets oscillate in a periodic fashion with the time period of oscillation depending on the operating parameters like the spacing between the nozzles, the characteristic jet flow-velocities and the width of the nozzles in addition to the fluid density and viscosity. Their experiments yielded dimensionless relations between the oscillating time periods, the Reynolds numbers associated with the unequal jets and the nozzle width to spacing ratios. For the case of equal jets, they also provided a neutral curve separating the oscillatory from the stationary flow regimes in the dimensionless parametric space.

Nossier and Shabtay [30, 31] investigated the behaviour of two round turbulent jets impinging on each other in a *side-dump ramjet combustor*. Their visualization results showed the generation of counter-rotating vortex pairs in the impingement region with strength changing periodically due to their stretching in the downstream direction of the combustor.

In another experimental investigation involving isothermal counter-flowing streams, Rolon et al. [32] found that multiple steady states existed for a given set of operating conditions. For the case of equal inlet mass flow rates, they found that two stable flow states existed with the stagnation point shifted along the line of symmetry on either side of the mid-plane between the nozzles / slots. Wood et al. [33] carried out an experimental as well as a numerical study of three-dimensional flows induced by horizontal laminar isothermal opposed jets in a vertical cylinder closed at the bottom. The jet Reynolds number was varied from 50-300. They also found that beyond a certain threshoid value of Re, the jets undergo oscillations.

A numerical investigation was carried out to predict and compare the fluid flow and heat transfer characteristics of five low-Reynolds-number k-ε models and the standard high-Reynolds-number model for two-dimensional turbulent confined impinging and opposing jet flows in an isothermal channel by Hosseinalipour and Mujumdar [34]. The aspect ratio (H / D) was taken as 1.5 and Reynolds number as 8000. The stagnation region was difficult to predict accurately with any one of the tested models. Outside this region, the Jones and Launder model [35] yielded adequate representation of the experimental data.

A numerical study of confined two-dimensional opposing turbulent jets of superheated steam over a range of nozzle-to-nozzle separations and jet Reynolds numbers in an isothermal channel, was performed by Hosseinalipour and Mujumdar [36]. The standard k-ε model was used to solve the governing conservation equations for fluid flow. Predictions were performed in two distinct parts. In the first part, hybrid, finite volume method based on the "SIMPLEC" algorithm was used to solve the momentum and energy equations and in the second part the trajectories and drying of single particles with different Stokes numbers were computed by solving the differential equations of particle trajectories analytically assuming a constant fluid velocity over the short integration time Δt. Results were presented in terms of the residence time of injected particles in the flow domain.

Hosseinalipour and Mujumdar [37, 38] carried out a numerical investigation of flow and thermal characteristics of steady two-dimensional confined laminar opposing jets in a planar channel. The studies were carried out for the *forced* convection regime for equal and unequal jets. For investigating the heat transfer characteristics, the temperatures of the opposed jets were taken to be equal but different from that of the channel walls. For the thermal mixing characteristics, the opposed jets were taken at different temperatures

while the channel walls were taken to be adiabatic. The effects of jet Reynolds number and channel height to jet-width ratio on local heat transfer and mixing characteristics were reported.

An opposed jet burner which features impingement of two opposed jet flames, for the study of high-intensity combustion in the distributed reaction regime, was described by Yoshida [39]. This burner could be applied to both premixed and diffusion flame studies. A stable annular turbulent premixed or diffusion flame could be stabilized between two ceramic plates, which ensure an adiabatic environment for the flame. A characteristic feature of this burner was its easy optical access and probe measurements. It was shown that NO_x emission was low in high-intensity turbulent flames due to the short residence time.

Experimental as well as numerical studies of the interaction of horizontal laminar opposed *unequal* jets in a vertical cylinder closed at the bottom were also conducted by Johnson [40, 41]. The investigations were aimed at; a) highlighting the flow characteristics induced particularly by the momentum imbalance of the opposed jets and b) suggesting strategies for controlling some of the negative aspects of the flow characteristics.

Numerical studies of confined turbulent opposing jets of different fluids were taken up by Wang and Mujumdar [42] using low Reynolds number k– ε turbulence models to examine the effects of intrinsic density difference on the flow pattern and mixing characteristics in a three-dimensional in-line static mixer. Unequal jets were achieved by varying the mass flow rate ratio and / or inlet channel jet width ratio of opposing jets. It was found that, as compared with equal jets, two asymmetric recirculation bubbles were formed after jet impingement and a higher level of turbulent kinetic energy was produced

in the impingement region as well as its vicinity. Result showed that better mixing was obtained for unequal jets than equal jets for the same total mass flow rate.

Wang et al. [43] also carried out a numerical investigation of two-dimensional laminar flow caused by non-isothermal impinging streams in an adiabatic channel. The buoyancy effects were neglected and temperature was treated as a passive scalar. The study primarily focused on effects of momentum ratio and width ratio of the two impinging fluid streams with a constant total mass flow in the channel. It was reported that the unequal inlet momenta of the streams could improve mixing under certain operating and geometrical configurations. They also demonstrated that placement of multiple staggered baffles in the channel resulted in better mixing owing to vortex formations and shear.

More recently, motivated by the above findings that point to a rich dynamic behavior exhibited by such flow systems, Pawlowski et al. [44] carried out a numerical study of the stability and the bifurcations of flows generated by laminar isothermal counter-flowing *equal* jets in planar and cylindrical geometries. In a parametric space of Jet Reynolds number (Re) and the ratio of nozzle / slot width to the spacing between the nozzles / slots (ζ), the steady states of the flow along with their stability was examined by employing a global stability analysis of the perturbation equations. For the planar configuration, four distinct flow regimes were identified in the range $1 \leq Re \leq 1500$ and $0.05 \leq \zeta \leq 1.0$: (i) Single Steady State (symmetric) regime (ii) Multiple Steady State (asymmetric) regime, (iii) Oscillating or Deflecting jet and (iii) Vortex shedding regime. For the cylindrical configuration, however, for axisymmetric (2D) as well as non-axisymmetric (3D) flows, no oscillatory or Hopf bifurcations were reported. Only the Pitchfork bifurcation leading to multiple steady states was found.

B. Mixed Convection Regime

Devahastin and Mujumdar [45] conducted a numerical study of two-dimensional laminar steady flow and mixing in an impinging stream in-line mixer. The novelty of the work was in the choice of the system configuration that involved two, in-line, inlet jets / streams on either side of the two-dimensional adiabatic mixing channel. The nozzles / slots were slightly offset so that the opposing streams do not impinge head-on. The streams of upper and lower nozzles / slots were of unequal temperature so that mixing could be monitored using temperature as a passive scalar. Effects of jet Reynolds number, ratio of height of channel to jet width and ratio of spacing between the two inlet jets to the jet width on the flow and mixing characteristics were reported.

In another study, Devahastin and Mujumdar [46] performed numerical simulations of two-dimensional laminar flow caused by non-isothermal impinging streams in an adiabatic channel. The temperature was treated as a passive scalar. Simulations were carried out for; (i) inlet Re varying from 10 to 10000 and, (ii) the ratio of channel height to jet width (H / D) varying from 1.0 to 4.0. In order to capture the possible bifurcations, an unsteady model was employed. For different combinations of Re and H / D, three different flow regimes were reported. These were: (i) the Steady Flow regime, (ii) the Periodic Flow regime and, (iii) the Random Oscillatory regime. For the steady flow regime, the thermal mixing characteristics were reported. It was concluded that an increase in the jet Re slows down the thermal mixing owing to the reduction in the residence time.

In another investigation involving the same geometry, Wang et al. [47] studied the effects of variations in thermo-physical properties caused by temperature variations. It was shown that even for equal jets, an asymmetric flow developed after the jet

impingement, leading to a strong vortex formation and shear that affects the mixing process.

1.3 Conclusions

From the literature surveyed, the following gaps can be readily identified for the generic problem of interaction of opposed / counter-flowing impinging streams in confined geometries.

1. Problems related to interactions of jets in an isothermal environment have received the maximum attention [Refs 28, 29, 33, 40, 41, and 44].
2. For non-isothermal jets a number of numerical investigations have been reported [Refs 37, 38, 43, 45, 46 and 47]. However, most of the studies, except Devahastin and Mujumdar [46], utilized a steady flow model thereby eliminating the possibility of capturing the possible instabilities and bifurcations.
3. The studies carried out for non-isothermal impinging streams, are in the forced convection regime. Therefore the effects of thermal buoyancy on the flow and mixing characteristics have not been investigated in detail.
4. If the impinging streams are of different fluids (same phase), buoyancy forces owing to inherent differences in the densities may affect the flow dynamics significantly. These aspects have not been investigated in the earlier works.

1.4 Problem description

The present work involves numerical investigation of two-dimensional interaction of two opposing jets / streams of *different* miscible fluids (same phase) in a channel in the mixed convection laminar flow regime. The buoyancy forces due to temperature difference (thermal buoyancy) as well as inherent differences in the densities of the two fluid streams (intrinsic buoyancy) are considered through the Boussinesq approximation.

In addition to the geometric and boundary condition related parameters, the Prandtl number, the Schmidt number and the Reynolds number; the buoyancy forces (thermal and intrinsic) give rise to thermal and intrinsic Richardson numbers, Ri_T and Ri_C, respectively as the dimensionless numbers in the governing equations. Figure 1.8 depicts the geometry of the problem considered. The upper stream comprises of heavier fluid at lower temperature and the lower stream is of lighter fluid at higher temperature. The properties of two jets with regards to body forces are chosen in such a way that two buoyancy forces aid in the mixing of jets.

The inspiration for choosing the particular problem comes from the fact that the effect of thermal and intrinsic buoyancy forces on mixing of counter-flowing jets have not been taken up in any research work earlier. Also an unsteady model is used in order to capture instabilities and bifurcations in the flow.

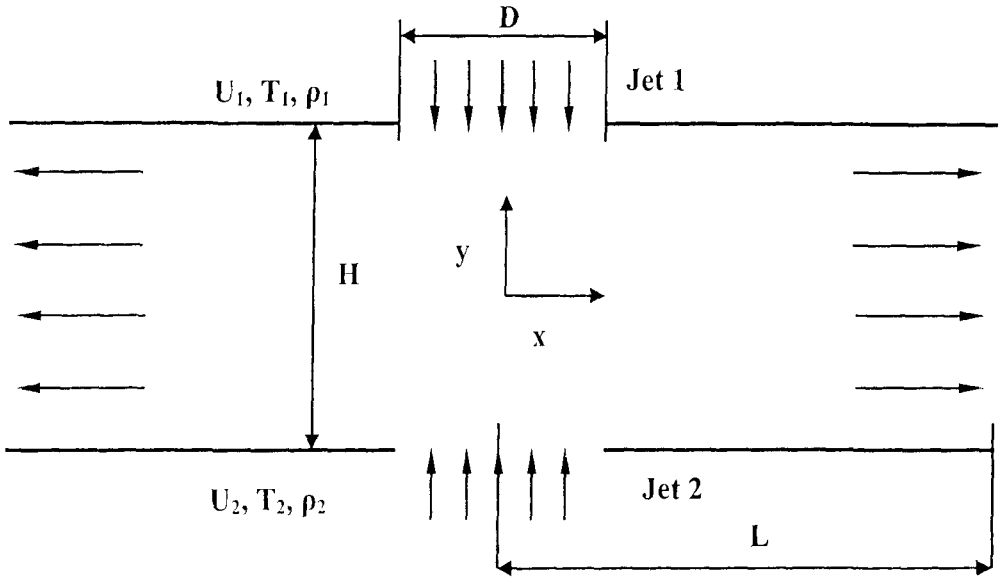

Fig. 1.8: Generic configuration of a counter-flowing jet interaction in a 2-D rectangular channel

From the fundamental point of view, the study the spatio-temporal changes in the flow structure with the variation of non-dimensional parameters is important and not well known for the class of problem under consideration. The parametric space of the generic

problem consists of seven important dimensionless numbers namely; *velocity ratio (VR), H / D, L / D, Ri_T, Ri_C, Re, Sc and Pr*. The effect of these parameters on flow dynamics needs to be investigated thoroughly in order to design efficient flow systems for different operating conditions.

1.5 Objectives

The main objectives of the present study are:

1. Investigation of the effects of buoyancy (thermal and intrinsic) on changes in the flow structure in both space and time at a fixed *H / D, L / D, VR, Re, Sc* and *Pr*, by varying Ri_T *and* Ri_C in the mixed convection regime.
2. Identification of the different possible flow regimes (steady and unsteady) in the domain of the parametric space of the problem chosen for study.
3. Identification of the dominant structures in the flowfield in the unsteady regime, if it exists within the range of parameters considered, by utilizing a POD (Proper Orthogonal Decomposition) analysis of the computational data.
4. Study of momentum imbalance effects on the dynamics of flow by varying *velocity ratio (VR)* of the two impinging jets.
5. To quantitatively describe the mixing process via suitable scalar measures and correlate it to the relevant dimensionless operating parameters. Specifically, the operating conditions that lead to high rates of thermal and physical mixing, within the ranges of the parameters considered, would be identified.

1.6 Summary

The present problem belongs to the generic class of double diffusive counter-flowing jet interactions in enclosures. The class of problem under investigation has many potential

applications [Ref. 25]. The work involves a numerical investigation of two-dimensional interaction of two non-isothermal opposing jets / streams of *different* miscible fluids (same phase) in an adiabatic channel in the mixed convection laminar flow regime. The two buoyancy forces are considered in such a way that they aid in mixing of jets. It is concluded from the literature reviewed that the chosen problem has not been investigated earlier.

The present study focuses on both fundamental aspects of fluid flow as well as the practical applications of jet mixing. From the fundamental point of view, a detailed investigation involving the effect of variation of different parameters on the spatio-temporal structure of the flow is proposed. From the practical point of view, different parameters which quantify mixing of two jets would be reported and correlated to the relevant dimensionless parameters. A POD analysis of the computational data would be carried out to identify the dominant spatial structures in the unsteady flow regime if it exists. This would also help in identifying the character of the possible bifurcations and instabilities.

The next chapter focuses on the mathematical formulation of the problem and the description of the numerical methodology employed to obtain the solutions of the mathematical model of the problem.

Chapter 2

Problem Formulation and Solution Methodology

This chapter comprises of five sections. The mathematical model involving the basic governing equations within the framework of Boussinesq approximation is presented along with the boundary and initial conditions in §2.1. Section 2.2 presents the ranges of the various dimensionless parameters chosen for the present investigation. The details of the numerical scheme together with the various types of discretization procedures adopted are provided in §2.3. Section 2.4 deals with the validation studies. Finally a brief summary of the entire chapter is given in §2.5.

2.1 Mathematical Formulation and the Governing equations

The present study is a numerical investigation of laminar flow induced in a 2-D rectangular channel by counter-flowing impinging jets / streams of *different* miscible fluids (non-reacting, same phase) in the mixed convection regime. To model the interactions and flow, the fluid in the flow domain (Fig. 1.8) is modeled as a binary non-reacting mixture. Therefore, the local flow state can be described by the binary-mixture properties like, density, velocity, pressure, temperature and mixture concentration. The equations of;

(i) the conservation of overall mass,

(ii) the transport of momentum,

(iii) transport of energy (thermal) and

(iv) the transport of mixture concentration,

are utilized to model the flow physics. To account for buoyancy effects (thermal and intrinsic), the fluid (binary-mixture) density 'ρ' at a given temperature is related to densities of pure components, ρ_1 and ρ_2, (assuming $\rho_2 > \rho_1$) at the same temperature by the relation,

$$\frac{1}{\rho} = \frac{1}{\rho_1(T)} + C\left(\frac{1}{\rho_2(T)} - \frac{1}{\rho_1(T)}\right), \tag{2.1}$$

where C is mixture concentration (mass fraction of heavier component 2) for the mixture.

The buoyancy forces are introduced in the momentum equations via the Boussinesq approximation. In this approximation, the density variations are only accounted in an external force field like gravity and neglected elsewhere in the governing equations. The binary-mixture density variations 'Δρ' over a reference state ρ_o, are expressed as a function of temperature and concentration variations by the linearized relation:

$$\frac{\Delta\rho}{\rho_o} = \frac{1}{\rho_o}\left(\frac{\partial\rho}{\partial T}\right)_o (T - T_o) + \frac{1}{\rho_o}\left(\frac{\partial\rho}{\partial C}\right)_o (C - C_o) \tag{2.2}$$

The partial derivatives of mixture density with respect to temperature and concentration can be found from Eq. (2.1) as,

$$\left(\frac{\partial\rho}{\partial T}\right)_o = \frac{\rho_o^2}{\rho_{o1}^2}\left(\frac{d\rho_1}{dT}\right)_o + C_o\left[\frac{\rho_o^2}{\rho_{o2}^2}\left(\frac{d\rho_2}{dT}\right)_o - \frac{\rho_o^2}{\rho_{o1}^2}\left(\frac{d\rho_1}{dT}\right)_o\right]$$
$$\left(\frac{\partial\rho}{\partial C}\right)_o = -\rho_o^2\left(\frac{1}{\rho_{o2}} - \frac{1}{\rho_{o1}}\right) \tag{2.3a, b}$$

where ρ_{o1} and ρ_{o2} are densities of the pure components at the reference temperature.

If the coefficients of thermal expansion of pure components at the reference temperature are defined as $\beta_{o1} = -\frac{1}{\rho_{o1}}\left(\frac{d\rho_1}{dT}\right)_o$ and $\beta_{o2} = -\frac{1}{\rho_{o1}}\left(\frac{d\rho_2}{dT}\right)_o$, then the partial derivative in Eq. (2.3a) can be expressed as,

$$\left(\frac{\partial\rho}{\partial T}\right)_o = -\frac{\rho_o^2}{\rho_{o1}}\beta_{o1} + C_o\left[\frac{\rho_o^2}{\rho_{o1}}\beta_{o1} - \frac{\rho_o^2}{\rho_{o2}}\beta_{o2}\right] \tag{2.4}$$

Assuming small density variations (in the spirit of the Boussinesq approximation),

$\frac{\rho_o}{\rho_{o1}} \approx \frac{\rho_o}{\rho_{o2}} \approx 1.0$ we get,

$$\left(\frac{\partial \rho}{\partial T}\right)_o = -\rho_o[\beta_{o1} + C_o(\beta_{o2} - \beta_{o1})]. \tag{2.5}$$

Therefore, the coefficients of thermal and concentration expansion of the binary mixture at reference state can be defined as,

$$\begin{aligned} \beta_{mT} &= -\frac{1}{\rho_o}\left(\frac{\partial \rho}{\partial T}\right)_o = \beta_{o1} + C_o(\beta_{o2} - \beta_{o1}) \\ \beta_{mC} &= +\frac{1}{\rho_o}\left(\frac{\partial \rho}{\partial C}\right)_o = \rho_o\left(\frac{\rho_{o2} - \rho_{o1}}{\rho_{o2}\rho_{o1}}\right) \end{aligned} \tag{2.6a, b}$$

The reference state density of the mixture, 'ρ_o', is taken to be the density at a reference temperature 'T_o' and a reference concentration 'C_o'. The reference temperature is taken to be the mean temperature of the two fluid streams, $T_o = (T_1+T_2)/2$ while the reference value of C_o is taken to be 0.5. Therefore, from Eq. (2.1), the reference density of the mixture can be expressed in terms of the reference densities of the pure components as,

$$\rho_o = \frac{2\rho_{o1}\rho_{o2}}{\rho_{o1} + \rho_{o2}}. \tag{2.7}$$

The expansion coefficients of the binary mixture can be further simplified and expressed as,

$$\begin{aligned} \beta_{mT} &= -\frac{1}{\rho_o}\left(\frac{\partial \rho}{\partial T}\right)_o = 0.5(\beta_{o2} + \beta_{o1}) \\ \beta_{mC} &= +\frac{1}{\rho_o}\left(\frac{\partial \rho}{\partial C}\right)_o = 2\left(\frac{\rho_{o2} - \rho_{o1}}{\rho_{o2} + \rho_{o1}}\right) \end{aligned} \tag{2.8a, b}$$

Finally, the density variations of the binary mixture as given in Eq. (2.2) can be expressed, customarily as,

$$\Delta\rho = -\rho_o\beta_{mT}(T - T_o) + \rho_o\beta_{mC}(C - C_o). \tag{2.9}$$

The above model for small variations in mixture density is utilized, within the framework of Boussinesq approximation, to obtain the governing equations for the flow of the binary mixture. The dimensionless governing equations of overall mass, momentum, energy and the mass transport are,

Overall mass conservation: $$\frac{\partial u}{\partial x} + \frac{\partial v}{\partial y} = 0 \tag{2.10}$$

x-momentum: $$\frac{\partial u}{\partial \tau} + u\frac{\partial u}{\partial x} + v\frac{\partial u}{\partial y} = -\frac{\partial P}{\partial x} + \frac{1}{Re}\left(\frac{\partial^2 u}{\partial x^2} + \frac{\partial^2 u}{\partial y^2}\right) \tag{2.11}$$

y-momentum: $$\frac{\partial v}{\partial \tau} + u\frac{\partial v}{\partial x} + v\frac{\partial v}{\partial y} = -\frac{\partial P}{\partial y} + \frac{1}{Re}\left(\frac{\partial^2 v}{\partial x^2} + \frac{\partial^2 v}{\partial y^2}\right) + Ri_T\theta - Ri_C\overline{C} \tag{2.12}$$

Energy transport: $$\frac{\partial \theta}{\partial \tau} + u\frac{\partial \theta}{\partial x} + v\frac{\partial \theta}{\partial y} = \frac{1}{Re\cdot Pr}\left(\frac{\partial^2 \theta}{\partial x^2} + \frac{\partial^2 \theta}{\partial y^2}\right) \tag{2.13}$$

Mass transport: $$\frac{\partial \overline{C}}{\partial \tau} + u\frac{\partial \overline{C}}{\partial x} + v\frac{\partial \overline{C}}{\partial y} = \frac{1}{Re\cdot Sc}\left(\frac{\partial^2 \overline{C}}{\partial x^2} + \frac{\partial^2 \overline{C}}{\partial y^2}\right) \tag{2.14}$$

The governing equations have been converted into dimensionless form by employing the width of the two identical jets 'D' (Fig. 1.8) as the length scale, the mean bulk or flow velocity of the two streams '$U = (U_1 + U_2) / 2$' as the velocity scale and '$\tau = D / U$' as the time scale. The dimensionless pressure, temperature and scaled concentration are defined as,

$$P = \frac{\overline{p} - \overline{p_o}}{\rho_o U^2}, \qquad \theta = \frac{T - T_o}{\Delta T}, \qquad \overline{C} = C - C_o \tag{2.15}$$

The various dimensionless parameters in the governing equations are,

(i) Reynolds Number, $Re = \dfrac{UD}{\nu_o}$

(ii) Thermal Richardson number, $Ri_T = \dfrac{g\beta_{mT}\Delta T D}{U^2}$

(iii) Concentration Richardson number, $Ri_C = \frac{g\beta_{mC}D}{U^2}$

(iv) Prandtl number, $Pr = \frac{\nu_o}{\kappa_o}$

(v) Schmidt number, $Sc = \frac{\nu_o}{D_{12}}$

All fluid (binary mixture) properties (ν, κ, ρ, D_{12} etc) are taken at reference temperature and concentrations T_o and C_o, respectively. In addition to the above dimensionless parameters in the governing equations, the geometric dimensionless parameters (Fig. 1.8) are,

(i) dimensionless height, $h = \frac{H}{D}$,

(ii) dimensionless half-channel length, $\ell = \frac{L}{D}$.

In addition to the above mentioned parameters, one parameter related to boundary condition, termed as velocity ratio also exists. It is symbolically represented as VR and defined as the ratio of the bulk velocity of jet 1 to the bulk velocity of jet 2 (refer Fig 1.8). Mathematically, $VR = \frac{U_1}{U_2}$.

2.1.1 Boundary and initial conditions

The inlet jet / stream velocity profiles are taken to be parabolic (laminar fully developed state) and can be expressed as,

$$V_i = \frac{3U_i}{U_1(1+U_2/U_1)}(1-4x^2),\ i = 1, 2 \qquad -0.5 \le x \le 0.5 \qquad (2.16)$$

The dimensionless temperatures (uniform) for the hot and cold inlet streams are fixed at +0.5 and -0.5 respectively, while the concentration of the intrinsically heavier and lighter

fluid stream is kept fixed at +0.5 and -0.5 respectively. The thermal and concentration boundary conditions at inlets are,

$$\begin{aligned} \theta = +0.5,\ \overline{C} = -0.5, \quad & -0.5 \le x \le +0.5,\ y = -h/2 \\ \theta = -0.5,\ \overline{C} = +0.5, \quad & -0.5 \le x \le +0.5,\ y = +h/2 \end{aligned} \tag{2.17}$$

The no-slip and non-penetrative condition is employed for the velocity components at the solid walls. The channel walls are adiabatic and mass flux across them is taken as zero i.e. $\left(\frac{\partial \overline{C}}{\partial y} = 0\right)$. At the outlet, the following conditions are employed,

$$\frac{\partial^2 u}{\partial x^2} = \frac{\partial v}{\partial x} = \frac{\partial^2 \theta}{\partial x^2} = \frac{\partial^2 \overline{C}}{\partial x^2} = 0 \tag{2.18}$$

It is worth mentioning that in the present work, the condition of fully developed flow is not employed at the channel exit. Instead, the channel length is taken long enough for the flow to develop and attain a *nearly* fully developed state. For laminar flow, generally a long length of the passage is needed for the flow to become fully developed. This increases the domain size and consequently the time of computations. Therefore, slightly shorter lengths are employed along with conditions given in Eq. 2.18. An exercise is carried out to determine an appropriate length that yields a flow dynamics that is not significantly affected by the choice of the above exit boundary conditions.

2.2 Parametric Space

The numerical study is carried out for fixed values of the dimensionless numbers; Re, Pr, Sc. The value of Reynolds number is chosen to be 200 which is well within the laminar flow regime [Ref. 43]. The values of Prandtl number and Schmidt number is fixed at 0.7 and 0.8, respectively. The values of Prandtl and Schmidt numbers are chosen from the point of view of physical realizability and can be achieved in physical experiments if one of the streams is of air and the other stream is a mixture of air and a

heavier gas like carbon dioxide, ethane, propane, butane etc. The range of the two Richardson numbers namely, Ri_T and Ri_C, is chosen between 0 and 1.5 which lies in mixed convection regime. Typically,

$$Ri_T = \{0, 0.5, 1, 1.5\} \text{ and } Ri_C = \{0, 0.5, 1, 1.5\}.$$

The aspect ratio, h, is kept fixed at 2. To examine the effect of difference of flow rate and momentum of the two jets, three different cases of velocity ratios, VR, are considered, typically, 0.5, 1 and 2.

2.3 Numerical Scheme

For the purpose of capturing the possible instabilities and bifurcations, an unsteady model is used for simulation. A semi-implicit, pressure correction type scheme, on a non-staggered structured Cartesian mesh employing a finite difference type of spatial discretisation is utilized. The concept of momentum interpolation of Rhie and Chow [48] as described by Ferziger and Peric [49], is utilized in order to avoid grid scale pressure oscillations that can otherwise result owing to the decoupling between the velocity and pressure at a grid point. The scheme is described by Hirsch [50] and is conceptually similar to the SMAC algorithm given by Amsden and Harlow [51]. The scheme is described in detail in the work of Hasan and Sanghi [52]. The details of the scheme are spread over the next two sub-sections. In §2.3.1, the details of time integration are presented while the details of the spatial discretisation are given in §2.3.2.

2.3.1 Time integration

The flowfield at a given time instant is marched forward in time using a two step predictor-corrector approach. In the predictor step, the time integration of momentum and energy equations is performed using an explicit two-step Adam-Bashforth scheme

yielding second order accurate estimates of provisional velocities, temperature and concentration of the binary fluid mixture. In the corrector step, the provisional estimates of the velocity field is then corrected in a vorticity preserving manner via pressure correction field to bring the divergence of the velocity field close to zero. Formally the scheme is given as follows:

A. Predictor step

At each grid point (i, j), the second order Adam-Bashforth integration in time of the momentum and energy equations yields

$$\bar{u}_{i,j}^{n+1}=u_{i,j}^{n}+\frac{3}{2}\delta\tau\left\{H_{i,j}^{n}-\left(\frac{\partial P}{\partial x}\right)_{i,j}^{n}\right\}-\frac{1}{2}\delta\tau\left\{H_{i,j}^{n-1}-\left(\frac{\partial P}{\partial x}\right)_{i,j}^{n-1}\right\} \tag{2.19a}$$

$$\bar{v}_{i,j}^{n+1}=v_{i,j}^{n}+\frac{3}{2}\delta\tau\left\{G_{i,j}^{n}-\left(\frac{\partial P}{\partial y}\right)_{i,j}^{n}\right\}-\frac{1}{2}\delta\tau\left\{G_{i,j}^{n-1}-\left(\frac{\partial P}{\partial y}\right)_{i,j}^{n-1}\right\} \tag{2.19b}$$

$$\theta_{i,j}^{n+1}=\theta_{i,j}^{n}+\delta\tau\left\{F_{i,j}^{n}\right\} \tag{2.19c}$$

$$\bar{C}_{i,j}^{n+1}=\bar{C}_{i,j}^{n}+\delta\tau\left\{E_{i,j}^{n}\right\} \tag{2.19d}$$

where superscript n and n-1 indicates the flowfield at time level n and n-1 respectively. The superscript n+1 represents the flow field at the new time level n+1.

The overbar is used to represent the guessed velocity components at time level n+1 which do not satisfy continuity. The terms $H_{i,j}$, $G_{i,j}$, $F_{i,j}$ and $E_{i,j}$ are the aggregates of convective and diffusive terms in the momentum, energy and the mass transport equations evaluated at a grid point on the basis of the flow field at time level n and n-1. It is worth mentioning that a second order accurate estimate of the temperature and concentration field is obtained in the predictor step itself.

B. Corrector step

As mentioned earlier, in this step the guessed velocity field obtained in the predictor step is corrected in a vorticity preserving manner through a pressure correction field. The velocity and pressure corrections are defined as,

$$\begin{aligned} u'_{i,j} &= u^{n+1}_{i,j} - \bar{u}^{n+1}_{i,j} \\ v'_{i,j} &= v^{n+1}_{i,j} - \bar{v}^{n+1}_{i,j} \\ p'_{i,j} &= P^{n+1}_{i,j} - P^{n}_{i,j} \end{aligned} \tag{2.20}$$

The velocity field at time level n+1 that satisfies continuity is related to the pressure field at time level n+1 through a semi-implicit discretisation in time of the momentum equations. This is given as,

$$u^{n+1}_{i,j} = u^{n}_{i,j} + \frac{3}{2}\delta\tau\left\{H^{n}_{i,j} - \left(\frac{\partial P}{\partial x}\right)^{n+1}_{i,j}\right\} - \frac{\delta\tau}{2}\left\{H^{n-1}_{i,j} - \left(\frac{\partial P}{\partial x}\right)^{n-1}_{i,j}\right\} \tag{2.21a}$$

$$v^{n+1}_{i,j} = v^{n}_{i,j} + \frac{3}{2}\delta\tau\left\{G^{n}_{i,j} - \left(\frac{\partial P}{\partial x}\right)^{n+1}_{i,j}\right\} - \frac{\delta\tau}{2}\left\{G^{n-1}_{i,j} - \left(\frac{\partial P}{\partial x}\right)^{n-1}_{i,j}\right\} \tag{2.21b}$$

Relationships between velocity corrections and pressure correction can be obtained by subtracting Eq. (2.19a) from Eq. (2.21a) and Eq. (2.19b) from Eq. (2.21b) respectively. This yields the following relations:

$$\begin{aligned} u'_{i,j} &= -\frac{3}{2}\delta\tau\left(\frac{\partial p'}{\partial x}\right)_{i,j} \\ v'_{i,j} &= -\frac{3}{2}\delta\tau\left(\frac{\partial p'}{\partial y}\right)_{i,j} \end{aligned} \tag{2.22}$$

The pressure correction field must be such that it enforces continuity at the new time level. This is achieved as follows:

$$\left(\frac{\delta u}{\delta x}\right)_{i,j}^{n+1}+\left(\frac{\delta v}{\delta y}\right)_{i,j}^{n+1}=0 \tag{2.23}$$

$$\left(\frac{\delta \bar{u}}{\delta x}\right)_{i,j}^{n+1}+\left(\frac{\delta \bar{v}}{\delta y}\right)_{i,j}^{n+1}+\left(\frac{\delta u'}{\delta x}\right)_{i,j}+\left(\frac{\delta v'}{\delta y}\right)_{i,j}=0 \tag{2.24}$$

Substituting for velocity corrections from Eq. (2.22) in Eq. (2.24) yields,

$$\frac{\delta}{\delta x}\left(\frac{\partial p'}{\partial x}\right)_{i,j}+\frac{\delta}{\delta y}\left(\frac{\partial p'}{\partial y}\right)_{i,j}=\frac{2}{3}\left(\frac{1.0}{\delta \tau}\right)\left[\left(\frac{\delta \bar{u}}{\delta x}\right)_{i,j}^{n+1}+\left(\frac{\delta \bar{v}}{\delta y}\right)_{i,j}^{n+1}\right] \tag{2.25}$$

The pressure correction is thus obtained by solving the above Poisson equation.

The pressure correction is obtained in the interior from Eq. (2.25) subject to the following boundary conditions, as suggested by Cheng and Armfield [53] and reported in Hasan et. al. [54],

Inflow and Walls (velocity specified): $$\frac{\partial p'}{\partial n}=0 \tag{2.26a}$$

Outflow: $$p'=0 \tag{2.26b}$$

where n is the local normal direction to the boundary of the domain.

Once the pressure correction field is obtained, Eq. (2.22) can be readily employed in the interior of the flow domain to correct the guessed velocity field so that a near solenoidal velocity field is obtained.

It is observed that the velocity correction field as defined via Eq. (2.22) is irrotational in character. Thus the vorticity associated with the guessed velocity field is preserved in the corrector step. The current method is thus similar to the SMAC method where the guessed velocity field obtained from the momentum equations is corrected by adding irrotational velocity corrections to enforce continuity at the new time level. Equations (2.22) and (2.25) are used only in the interior to obtain the corrections and hence the flow

field at the new time step. At the solid walls, the no-slip and no penetration condition is explicitly specified for the velocities. The pressure at the inlet boundary and solid walls is updated through the normal momentum equation and at outflow boundary through Grashof boundary condition. These conditions are the same as employed by Cheng and Armfield [53] and Hasan et. al. [54].

2.3.2 Spatial discretisation

The spatial discretisation of the Eqs. (2.19a)–(2.19d), (2.22) and (2.25) is carried out using a finite difference methodology on a Cartesian colocated mesh. For the interior nodes, the convection terms are discretised using a hybrid scheme of a fourth order, central differencing and a third order Taylor series based upwinding scheme. The upwinding scheme employs two points on the upstream side and one point on the downstream side of the grid point under consideration. The choice between upwinding and central differencing is made on the basis of the local cell Peclet number. If $|Pe| < 2$ then central differencing is preferred, otherwise upwinding is utilised. For near boundary points, the convective terms are discretised using a second order central differencing. The viscous terms are discretized using a fourth order, symmetric, central differencing in the interior while a second order central differencing scheme is utilized for the near boundary mesh points. Since a non-uniform grid spacing will be employed, the expressions for third order upwind and fourth order central discretizations for first order spatial derivatives and five point central discretization have been derived and are presented in *Appendix A*.

The discretization of Eq. (2.25) needs to be handled carefully on a colocated grid. It is well known [Ref. 49] that a central discretization of terms on both sides of Eq. (2.25) leads to an effective discrete equation on a mesh twice as coarse as the actual grid.

Further, central discretization of the divergence term on the right hand side of Eq. (2.25) results in pressure-velocity decoupling. These effects permit spurious grid scale pressure oscillations [Refs. 49, 53]. In order that the scheme does not permit such non physical solutions specifically due to the above mentioned reasons, a compact discretization along with the momentum interpolation procedure is employed which is described in detail in Ref. [54]. The discrete poisson equation is solved numerically using Stone's SIP procedure as given in Ref. [49].

2.4 Validation

The FORTRAN code used in the present study has been validated with the data from the numerical simulations of 2-D, laminar, steady flow in a channel caused by opposing isothermal jets / streams impingement carried out by Hosseinalipour and Mujumdar [37]. The geometric configuration was the same as shown in Fig. 1.8. Further, the flow was taken to be symmetric about the vertical centerline ($x = 0$) and therefore symmetry conditions were imposed on it. Results were reported in a parametric space defined by the following ranges of parameters: $50 \leq Re_j \leq 500$ and $0.5 \leq h \leq 5.0$. The Prandtl number was fixed at 0.71. The top and bottom walls were kept at uniform equal wall temperatures and the jet temperatures were also kept equal but higher than the wall temperatures. In Ref. [37], the buoyancy forces were not considered and the temperature was treated as a passive scalar. Also, the jets / streams were of identical fluids and therefore the mass transport was not considered. Therefore for validation purposes both Ri_T and Ri_C are set equal to zero.

It is worth pointing out that in Ref. [37], the jet Reynolds number, Re_j, has been defined using hydraulic width of the nozzle feeding the two streams into the channel. Since the hydraulic width was twice the nozzle / slot width, the values of Reynolds

numbers (Re) employed in the present study would correspond to values of Re_j via the relation: $Re_j = 2\ Re$.

In order to validate the code, numerical simulations are carried out for; i) (Re = 100, h = 2) and ii) (Re = 250, h = 4), respectively. A 325×129 grid employed for validation studies is shown in Fig. 2.1. To depict the details clearly, only the grid in the central portion close to the jet interaction zone is shown. The mesh along the x-direction is fine

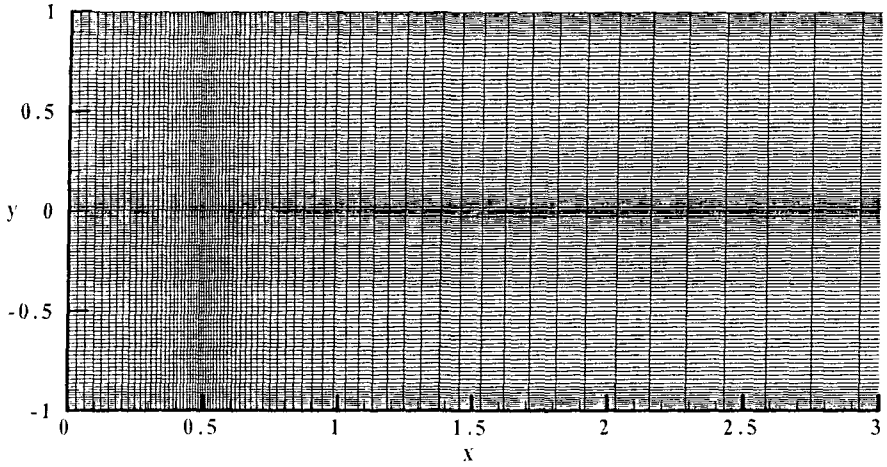

Fig. 2.1: A magnified view of 325 × 129 mesh employed for validation studies

near the edges of the jets in order to capture the flowfield in the vicinity of the jet / wall junction. The minimum and maximum spacing in the x-direction is 0.033 and 0.542 dimensionless units respectively. Along the y-direction the mesh is fine near the walls as well as near the channel centerline (min. spacing 0.00625) and relatively coarse (max. spacing 0.02) in the remaining portion. The computations were carried out for $\ell = 80$ and a dimensionless time step of 0.5×10^{-3}. The choice of the half-channel length, at this validation stage, is made in an adhoc manner and it will be shown that the results obtained are quite accurate with this choice. However, later, for carrying out the numerical experiments for the present work, an exercise is carried out for determining the appropriate range of the half-channel length.

Since the unsteady flow equations are employed in the present study, the time integrations were performed for a sufficiently long interval of time to permit the flow to attain a long term stable solution. In both the cases mentioned above, steady states were attained. For (Re = 100, h = 2), a flow pattern with two equal recirculating zones and symmetry about the channel centerline is observed. Figure 2.2(a), (b) shows the steady state streamline patterns for (Re = 100, h = 2) and (Re = 250, h = 4) respectively. The steady symmetric flow pattern at (Re = 100, h = 2) is in agreement with the linear stability analysis of Pawlowski et al [44]. At (Re = 250, h = 4), a non-symmetric steady state flow pattern is observed with a lower detached vortex or separation bubble (Fig. 2.2(b)). According to the linear stability calculations of Pawlowski et al. [44] at (Re = 250, h = 4), the symmetric state is unstable and the system exhibits multiple stable steady states (non- symmetric) as a result of a pitchfork bifurcation. Therefore the flow pattern in Fig. 2.2(b) agrees with the linear stability predictions.

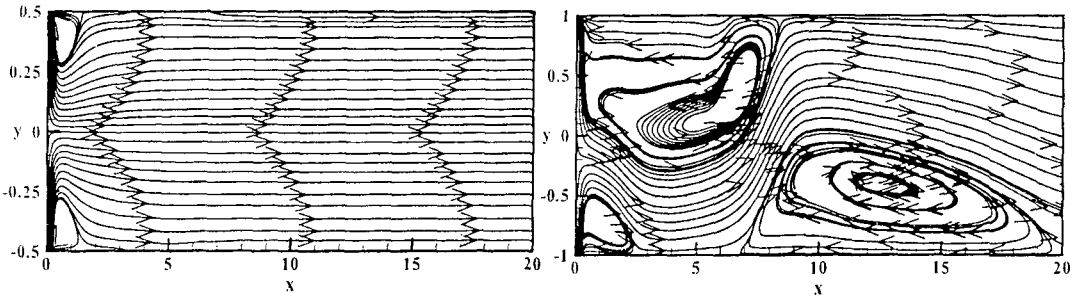

Fig. 2.2: Steady state streamline patterns for a) Re= 100, h = 2 b) Re = 250, h = 4

Figure 2.3(a), (b) depicts the axial velocity profile at a specific section (x = 4) for (Re = 100, h = 2) and the variation of Nusselt number along the bottom wall for (Re = 250, h = 4), respectively. The axial velocity is scaled by the bulk or flow velocity at the same section. The Nusselt number is based on the bulk temperature and has been normalized by the corresponding value for the fully developed laminar flow between parallel plates

(Plane Poisuelle Flow). The Nusselt number variation along the bottom wall undergoes non-monotonic variations due to the presence of a couple of separation zones. The velocity profile and the Nusselt number variation is in agreement with the numerical data obtained from Ref. [37]. The deviations in the wall Nusselt number data can be attributed to the differences in the numerical aspects of the two computations.

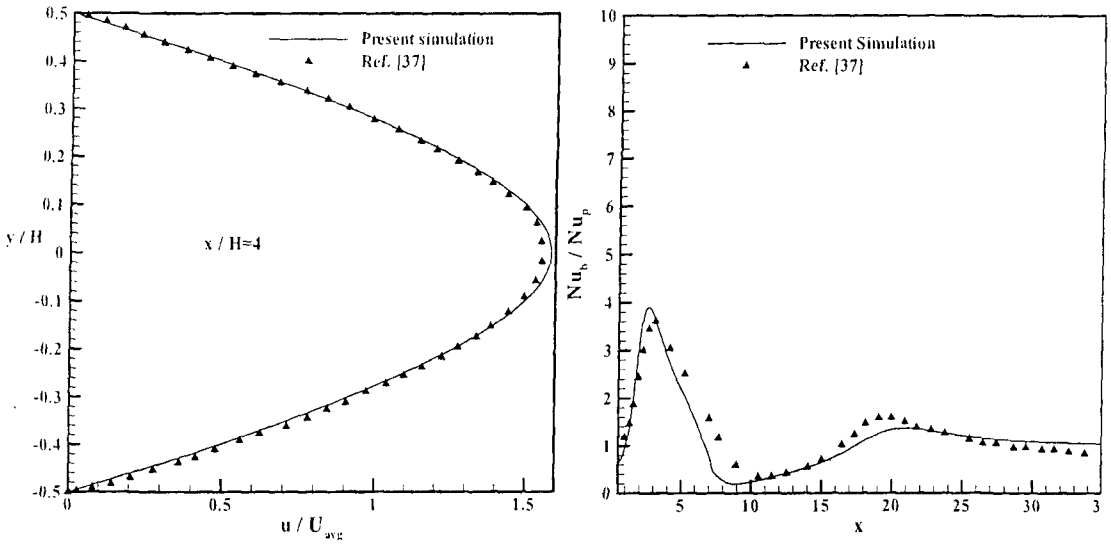

Fig. 2.3: a) Velocity profiles at (Re= 100, h = 2) and b) Wall Nusselt number at (Re = 250, h = 4) along with the numerical data of Ref. [37]

2.5 Summary

The problem of interaction of opposed jets / streams in a channel has been formulated by considering the fluid as a binary mixture. Both thermal and intrinsic buoyancy has been considered through Boussinesq approximation. The geometry of the flow domain along with the dimensionless form of the governing equations and chosen boundary conditions, shows that the flow is dependent on eight dimensionless numbers / groups, namely,

(a) Reynolds number, Re,

(b) Thermal Richardson number, Ri_T,

(c) Concentration Richardson number, Ri_C,

(d) Prandtl number, Pr,

(e) Schmidt number, Sc,

(f) Dimensionless channel height, h,

(g) Dimensionless half-channel length, ℓ,

(i) Velocity ratio, VR.

In the present study both the thermal and concentration Richardson numbers (Ri_T, Ri_C) are varied over the set of discrete values {0, 0.5, 1, 1.5}. Reynolds number is fixed at 200. Prandtl and Schmidt numbers are taken as 0.7 and 0.8 respectively such that one of the interacting streams could be considered as air and other a slightly heavier gas mixed with air. All the numerical experiments would be performed at h = 2 and a sufficiently long channel length would be taken so that the exit boundary conditions do not affect the flow in the interaction zone.

A finite difference, semi-explicit pressure correction scheme on a Cartesian, structured colocated mesh has been employed for the purpose of the numerical study. The scheme involves a two step predictor-corrector procedure. Using a second order, explicit two-step Adam-Bashforth integration, the velocity, the temperature and concentration fields are marched forward in time in the predictor step. While a second order accurate temperature and concentration fields are obtained after the predictor step itself, the velocity field obtained in the explicit predictor step does not satisfy continuity. The continuity is enforced by adding irrotational velocity corrections obtained via gradients of the pressure correction field. The pressure correction field is obtained by solving the pressure correction Poisson equation (PCPE) subject to appropriate boundary conditions at the inflow and outflow. The discretisation of PCPE is done by taking into consideration the pressure-velocity coupling issues on a colocated grid so that non-

physical grid scale pressure oscillations may not be permitted by the scheme. Standard techniques available in the literature, like compact discretisation of the divergence and gradient operators and momentum interpolation, have been utilized for this purpose. The discretized PCPE has a five-point molecule and is solved using a five-point SIP solver.

In order to validate the code, the numerical computations of 2-D, laminar, steady flow induced in a channel by interaction of opposing isothermal jets / streams carried out by Hosseinalipour and Mujumdar [37] are utilized. The geometric configuration was the same as shown in Fig. 1.8. Two cases were considered for validation, namely, a) (Re = 100, h = 2) and b) (Re = 250, h = 4). The Prandtl number was fixed at 0.71. The temperature of the two jets was equal and higher than the temperature of the two channel walls which were at same temperatures. The results from present simulation agree well with the numerical data from Ref. [37].

In next chapter, effect of thermal and physical buoyancy forces on flow dynamics and mixing characteristics at equal velocity ratio are reported and analysed.

Chapter 3

Flow Dynamics and Mixing Characteristics at VR = 1

In this chapter, the effect of buoyancy on the flow dynamics and mixing are presented. The bulk velocity ratio of the two streams is kept fixed at unity. The chapter is divided into four sections. In §3.1 numerical aspects such as grid independence and choice of suitable exit length of channel are discussed. The forced flow ($Ri_T = Ri_C = 0$) case is reported in §3.2. The effect of buoyancy on the flow structure (temporal and spatial) and its subsequent effect on the thermal and physical mixing is presented in §3.3. Finally a brief summary of the chapter is given in §3.4.

3.1 Numerical Aspects

Before carrying out the actual computations, exercises are carried out to assess the effect of (i) grid size on the solutions, and (ii) to determine the appropriate range of the channel length so that the flow dynamics is not significantly affected by the chosen numerical boundary conditions at the exit (Eq. 2.18) within that range.

For determining the appropriate half-channel length, a 423 × 129 grid is generated in a flow domain having $\ell = 120$. This grid is truncated at lower values of x = 100 and x = 80 to yield three flow domains with progressively shorter channel lengths but *same grid spacings*. This procedure is adopted so that the sensitivity of the results on the channel length could be isolated as the grid spacings are kept identical in all the three chosen flow configurations. The computations are carried out in all the three configurations ($\ell = 120, \ell = 100$ and $\ell = 80$) for equal jet velocities with Ri_T = 1.5, Ri_C = 0.5. The flow

is unsteady and periodic in nature. The axial velocity profiles of the mean flowfield, averaged over a periodic cycle, at x = 3, x = 10 and x = 60 are compared for the three

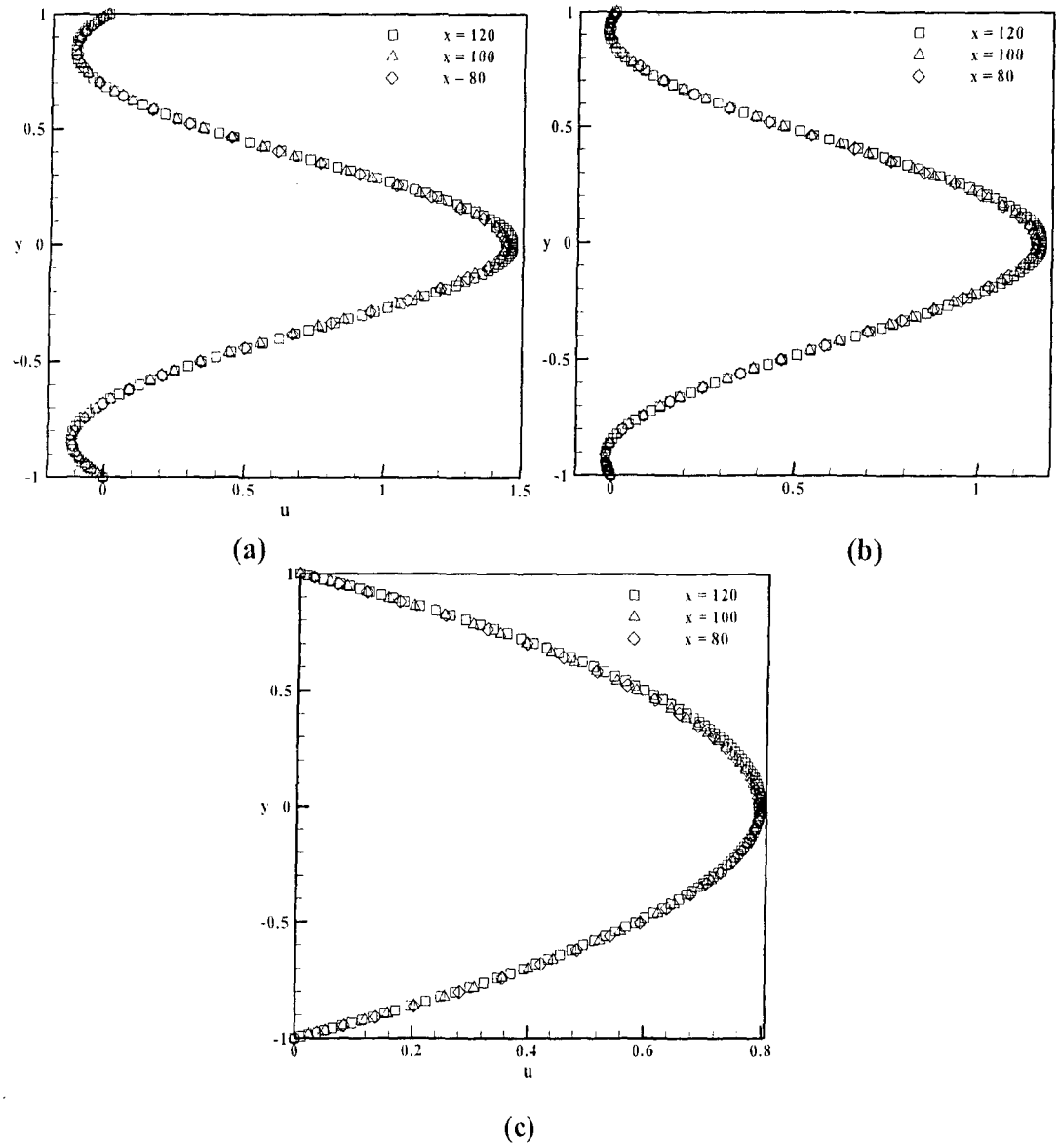

Fig. 3.1: Comparison of unsteady mean u-velocity profiles for different exit boundary locations at a) x = 3.0, b) x = 10 and c) x = 60 at (Ri_Γ = 1.5, Ri_C = 0.5)

different channel exit locations in Figs. 3.1(a)-3.1(c) respectively. It can be observed that the flowfield is not affected significantly in going from $\ell = 80$ configuration to $\ell = 120$. Therefore, $\ell = 100$ is considered suitable and all numerical computations are carried out for this half-channel length.

A grid independence study, employing three grids having 335×79, 379×129 and

Grid	Size	$(\Delta x)_{min}$	$(\Delta y)_{min}$	$(\Delta x)_{max}$	$(\Delta y)_{max}$
A	335 × 79	0.012	0.0088	0.9	0.047
B	379 × 129	0.0085	0.0065	0.9	0.0382
C	435 × 173	0.0043	0.0026	0.9	0.0314

Table 3.1: Various grids along with minimum and maximum spacing used in grid independence study

435×173 grid points, has been carried out to ensure that the results of the computations are relatively insensitive to the grid size. The various grid parameters are summarized in Table 3.1.

The computations are carried out for $Ri_T = 0.5$, $Ri_C = 0.2$ and $\ell = 100$. At these

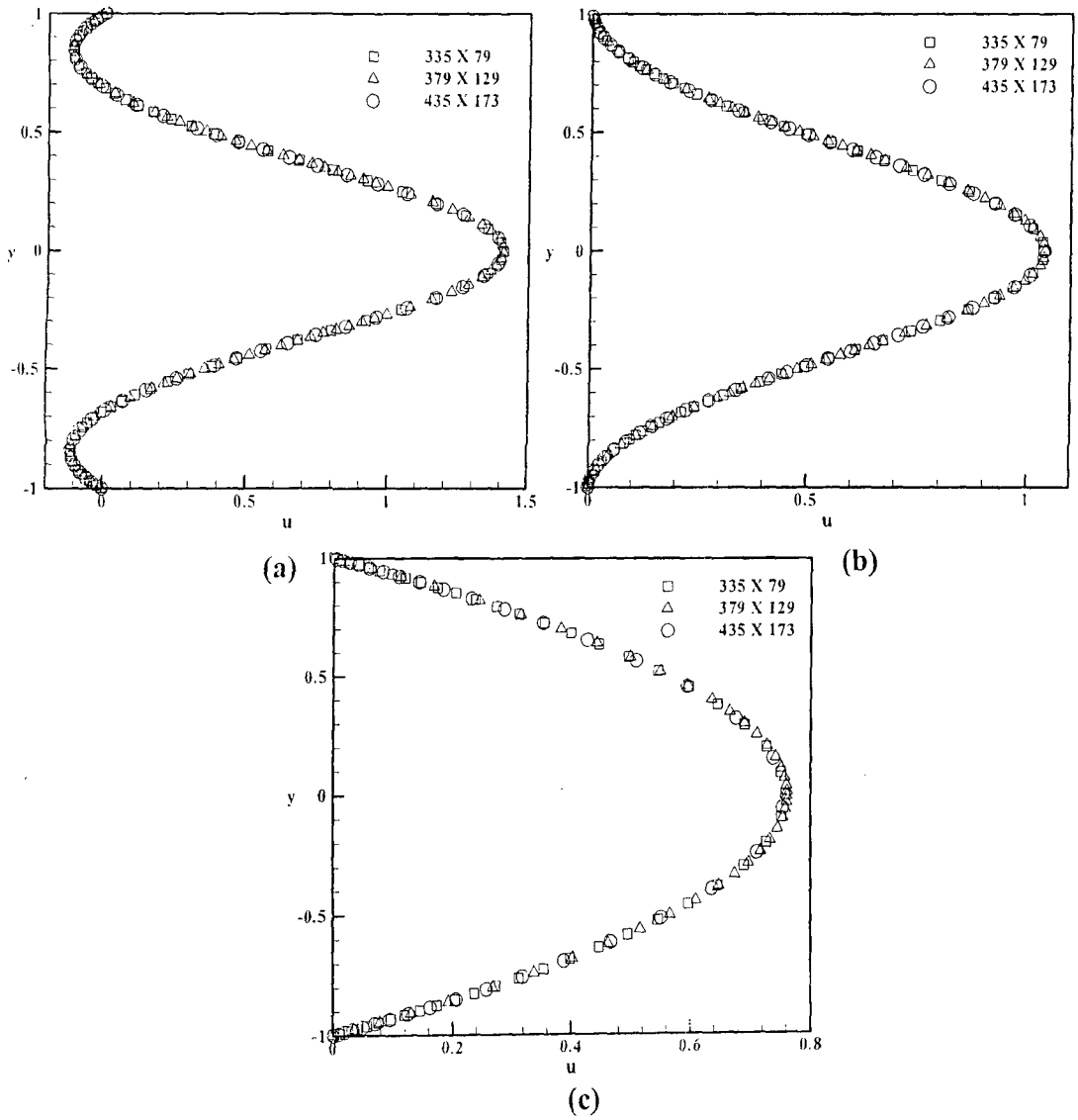

Fig. 3.2: Comparison of steady state u-velocity profiles for different choice of grids at a) x =3.0, b) x = 10 and c) x = 60 for ($Ri_T = 0.5$, $Ri_C = 0.2$)

values, the flow settled into long time steady state. The time step utilized in these computations is 10^{-3}. The level of satisfaction of the divergence-free constraint is monitored by comparing the volume flow rate at different sections of the flow passage with the inlet value. In the above computations, at any instant, less than 1% deviation in the volume flow rate along the channel length is observed. The steady state axial velocity profiles are compared for these three grids at x = 3, x = 10 and x = 60 in Fig. 3.2(a)-(c) respectively. A maximum deviation of about 2% is observed in going from 335×79 to a 379×129 grid, while the maximum deviation reduced to about 1% in going from 379×129 to a 435×173 grid. Therefore in order to save computational time, the 379×129 is adopted for the entire computations.

3.2 Forced Flow

The case of forced flow i.e. ($Ri_T = 0$, $Ri_C = 0$) has been included in order to assess, both qualitatively and quantitatively, the effects of thermal and intrinsic buoyancy forces on the flow dynamics. As mentioned earlier, the problem of forced flow has been investigated in detail by many workers. In particular Pawlowski et. al [44] have investigated the two-dimensional planar configuration in detail and examined the stability of the steady solutions obtained from the Navier-Stokes simulations via linear stability analysis. A complete bifurcation diagram was developed indicating the possible states in the parametric space of (Re, h). For (Re = 200, h = 2), they found that the flow system exhibited multiple steady states with the steady symmetric solution about y = 0 being unstable. Instead, a non-symmetric steady solution with a flow pattern having larger recirculation zones in the upper half than the lower half of the channel and vice versa was found to be stable. In the present context, the simulation carried out for the forced flow at (Re = 200, h = 2) is in agreement to the findings of Pawlowski et al [44].

For relatively short times ($\tau < 700$), the steady symmetric flow pattern is observed as shown in Fig 3.3(a). However, this pattern is unstable and owing to the growth of the unstable perturbation, in the limit of long time integrations ($\tau > 1000$), the flow attained a *steady stable non-symmetric state* as depicted by the streamline pattern in Fig. 3.3(b). As

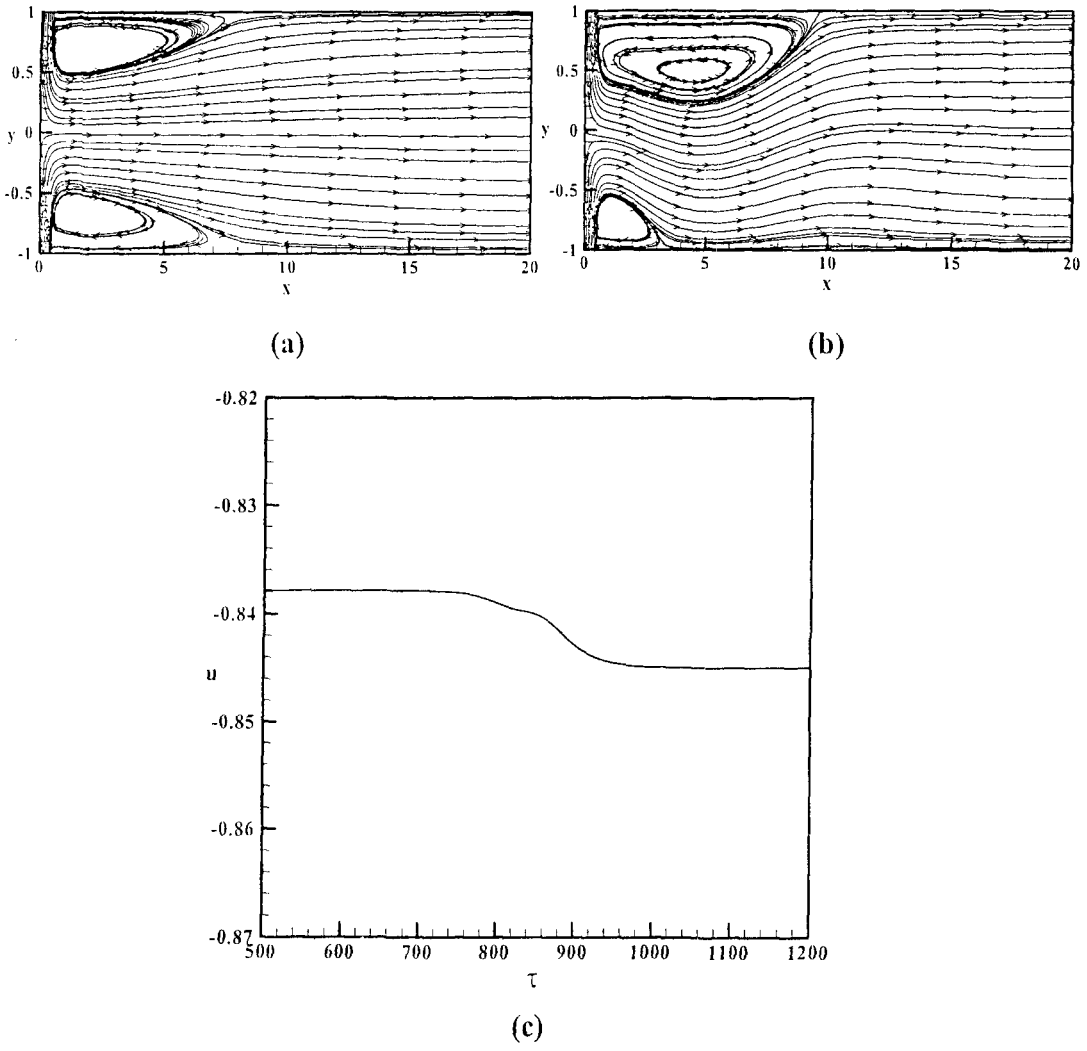

Fig. 3.3: The steady state streamline pattern for the forced flow for a) short times (unstable), b) large times (stable) and c) the time history of u(-15.56, 0) at (Re = 200, h = 2.0)

the symmetry about $x = 0$ is maintained, the pattern is shown only for the right half of the channel. In the upper half, a much larger separated zone is observed in comparison to the lower half. The growth of the instability and the transition from the steady symmetric unstable mode to a steady non-symmetric stable mode is captured in the time history of u-

velocity at (-15.56, 0) as depicted in Fig. 3.3(c). The time history has been sampled in the left half of the channel ($x < 0$). However, since the flow pattern is symmetric about $x = 0$, the character of the time history would be same at the point (+15.56, 0) in the right half of the channel.

3.3 Buoyancy Effects

The effect of variation of thermal and concentration Richardson numbers, in mixed convection regime, on structure and dynamics of the resulting flow due to impingement of two equal velocity jets is reported in this section. A complete regime map with neutral curve is obtained, within the parametric space of this study, by using Landau theory of linear stability given in detail by Drazin and Reid [55]. The spatial flow structure is represented by plots of instantaneous streamlines, isotherms and iso-concentration contours. In addition to these field plots, the axial velocity (u-velocity) profiles, temperature and concentration profiles are also generated at different streamwise or axial locations. Upper-wall pressure plots have been presented to illustrate the effect of buoyancy on pumping pressure. These spatial plots have been generated from data recorded after the initial transients have died out and the flow has settled into a long term stable state (steady or unsteady). The time history of flow variables is also recorded at 3 axial locations along the channel centerline ($y = 0$).

From the applications point of view, the chosen flow system is essentially a mixing device that attempts to mix the entering streams both thermally and physically. In order to quantify the state of mixing at any given axial position along the channel, a scalar measure termed as Mixing Index (MI) is defined. In the earlier studies [45, 46], a standard deviation from the local mean (at a particular axial location) is employed to estimate the mixing index. Defined in this manner, the Mixing Index is mathematically a

measure of flatness of the profile (uniformity of flow state) across the channel section. However, a better measure of mixing would be one that measures the instantaneous deviation of the state of fluid at any axial section from the thermodynamically attainable bulk values (of temperature and concentration). These values for the present flow system can be readily estimated using overall energy and mass conservation principles. Mathematically, the bulk average and the statistical average of a property (temperature / concentration) at any axial location can be expressed as,

$$\phi_B = \frac{\int_{-h/2}^{+h/2} \rho u \phi \, dy}{\int_{-h/2}^{+h/2} \rho u \, dy}, \quad \bar{\phi} = \frac{1}{h} \int_{-h/2}^{+h/2} \phi \, dy \tag{3.1}$$

As the present work is being carried out within the framework of Boussinesq approximation, the bulk average can be further simplified as,

$$\phi_B = \frac{\int_{-h/2}^{+h/2} u \phi \, dy}{\int_{-h/2}^{+h/2} u \, dy} \tag{3.2}$$

It is worth pointing out that for the adiabatic flow system without any mass transport from the solid walls, the bulk average temperature and concentration are independent of the axial location and are constant for the entire channel. The statistical averages, however, in general would vary along the channel length.

Using the bulk or the statistical averages, the local mixing index can be defined as,

$$MI(x) = \sqrt{\frac{1}{h} \int_{-h/2}^{+h/2} \left(\phi(x,y) - \phi_{avg}(x)\right)^2 dy}, \tag{3.3}$$

where, $\phi_{avg}(x) \equiv \phi_B$ or $\bar{\phi}$

Defined in this manner, the mixing index is a measure that represents the average deviation of any fluid property (temperature or concentration) from its bulk / statistical

average at any axial location along the channel. Further a normalized mixing index is employed which is defined as, $\langle MI \rangle = \frac{MI(x)}{MI(0)}$.

In order to quantitatively correlate the mixing characteristics to the various operating parameters like the two Richardson numbers, a mixing length, 'L_m', defined as the length from the centre of the channel (x = 0), where a particular level of mixing is achieved. This is analogous to defining boundary layer thickness, jet widths or width of mixing layers in free shear flows. In particular, we choose a normalized mixing index of *0.1* to define a mixing length that yields essentially a *90%* mixing level. Since the mixing lengths for thermal and physical mixing would be different in general, therefore they would be denoted as L_{mT} and L_{mC} respectively. The values of these lengths can be readily estimated from the mixing index characteristics by computing the length where the characteristic crosses the value of 0.1.

A quantitative measure which can represent the effectiveness of buoyancy forces, known as Buoyancy Mixing Effectiveness (e_m), is defined as,

$$e_m = \frac{1}{L/D}\int_0^{L/D}\left(\frac{\langle MI_f(x)\rangle - \langle MI(x)\rangle}{\langle MI_f(x)\rangle}\right)dx. \qquad (3.4)$$

The Buoyancy Mixing Effectiveness (e_m) gives an idea about how effective buoyancy forces are altering the mixing characteristics over and above the forced flow under similar conditions. A positive value of e_m implies that the buoyancy effects enhance the rate of mixing and vice versa. The buoyancy mixing effectiveness of thermal and concentration fields are symbolically represented as e_{mT} and e_{mC} respectively.

3.3.1 Flow regimes

In the range of Ri_T and Ri_C considered in the present study, two different flow regimes are obtained. For combined value of Ri_T and Ri_C less than 1.5, the flow is always

found to be steady in the limit of large times. For $(Ri_T + Ri_C) \geq 2$, the flow showed an unsteady, periodic behavior with vortex-shedding. These two regimes along with other flow regimes were also reported by Pawlowski et. al. [44], for isothermal interacting jets in a 2-D channel. Using linear stability analysis, they established that this vortex-shedding periodic regime was due to a Hopf bifurcation.

Vortex-shedding, due to supercritical Hopf bifurcation, is the outcome of growth of a linearly unstable mode or perturbation which evolves in time in an oscillatory manner. After the initial exponential growth in time, the infinitesimal unstable perturbation becomes finite and the non-linear self-interactions alter the exponential growth rate. This scenario was first proposed by Landau and given in detail by Drazin and Reid [55]. The growth of the amplitude of the oscillatory unstable mode in time, for small amplitudes, is governed by the famous Landau equation given as,

$$\frac{d}{d\tau}(A^2) = 2\sigma A^2 - l_u A^4 \tag{3.5}$$

The constant 'σ' represents the initial exponential growth rate of the amplitude and 'l_u' is the landau constant. The steady state amplitude of the unstable mode is readily obtained from Eq. (3.5) by setting $\frac{d}{d\tau}(A^2) = 0$ as,

$$A_e^2 = \frac{2\sigma}{l_u} \tag{3.6}$$

Clearly, equilibrium solutions to Eq. (3.6) are possible only if both σ, l_u are of same sign. For $\sigma > 0$, $l_u > 0$, a linearly unstable disturbance with amplitude $A < A_e$ will grow resulting in a *supercritical* instability. In contrast, for $\sigma < 0$ and $l_u < 0$, a disturbance of amplitude $A < A_e$ would decay, making the flow linearly stable to any infinitesimal

disturbance. However, for the latter case, a disturbance with amplitude $A > A_e$ would grow. This is referred to as a *subcritical* instability [55].

For the supercritical instabilities governed by the Landau scenario, the equilibrium amplitude A_e can be expressed in terms of the flow control parameter, say 'ξ'. Recognizing that the constants 'σ' and 'l_u' in general are functions of the control parameter, the Taylor's series can be used to expand these about the critical point as,

$$\sigma(\xi) = \sigma_c + \left(\frac{d\sigma}{d\xi}\right)_c (\xi - \xi_c) + O\left[(\xi - \xi_c)^2\right], \tag{3.7a}$$

$$l_u = l_{uc} + \left(\frac{dl}{d\xi}\right)_c (\xi - \xi_c) + O\left[(\xi - \xi_c)^2\right]. \tag{3.7b}$$

Since σ changes sign on either side of ξ_c, σ must vanish at the critical point ($\sigma_c = 0$) i.e the unstable mode or infinitesimal perturbation becomes neutrally stable (neither grows nor decays) at the critical point. Therefore, the equilibrium amplitude can be expressed as a function of the control parameter ξ as,

$$\begin{aligned} A_e^2 &= \frac{2}{l_{uc}}\left(\frac{d\sigma}{d\xi}\right)_c (\xi - \xi_c) + O\left[(\xi - \xi_c)^2\right] \quad \text{or,} \\ A_e^2 &\cong \frac{2}{l_{uc}}\left(\frac{d\sigma}{d\xi}\right)_c (\xi - \xi_c) \end{aligned} \tag{3.8}$$

Thus, within first order accuracy, sufficiently close to the critical point, the square of the equilibrium amplitude varies linearly with the control parameter 'ξ'. This law can be utilized to determine the critical value of the control parameter (Richardson number in the present context) corresponding to the supercritical bifurcation.

Using the above considerations, it can be inferred that the phenomenon of vortex-shedding at high Richardson numbers is a case of *supercritical Hopf bifurcation* as the unstable perturbation grows from *infinitesimal* proportions (sources being round-off errors) in an *oscillatory* manner. As a quantitative confirmation of the above statement,

the square of the equilibrium oscillatory flow amplitudes obtained from the time history of u(-15.56, 0) are plotted as a function of the control parameter Ri_T for $Ri_C = 0.5$ in Fig. 3.4. The data agrees well with a straight line fit, $A_e = a + b\ (Ri_T)$. This confirms that the onset of unsteady periodic behavior accompanied by vortex-shedding is a supercritical Hopf bifurcation. The implication of this line having positive slope and crossing the x-axis is that the exponential growth rate of the linearly unstable mode, σ, changes sign from negative to positive with increase in Ri_T across the critical point leading to the onset of the vortex-shedding (Eq. 3.8). Extrapolating the straight line fit, the critical thermal Richardson number Ri_T at $Ri_C = 0.5$, is obtained as 1.28.

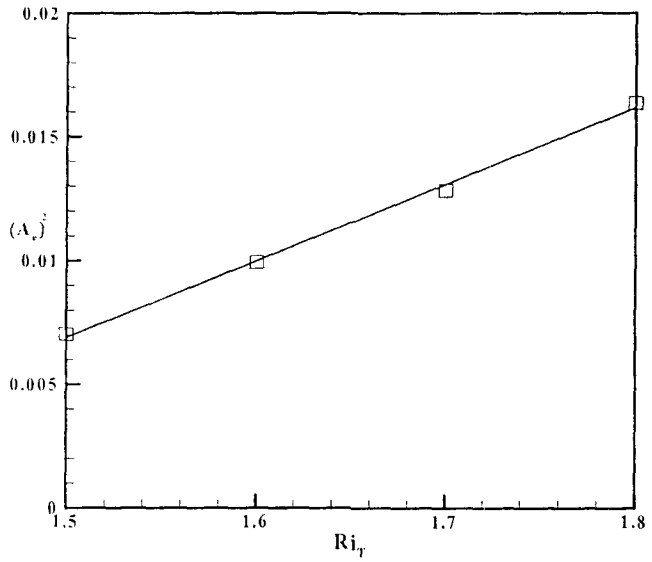

Fig. 3.4: Variation of square of equilibrium amplitudes of the periodic data of u(-15.56, 0) with the control parameter Ri_T in the neighborhood of bifurcation at $Ri_C = 0.5$

This approach of obtaining the critical Richardson number: (Ri_T or Ri_C) is employed to obtain approximately the neutral curve separating the steady and unsteady flow regimes in the parametric space spanned by $0 \leq Ri_T \leq 3$ and $0 \leq Ri_C \leq 3$. By fixing one of the two Richardson numbers, the other Richardson number is varied as a control parameter and the straight line fit constants (a, b) in the relation $A_e = a + b$ (control

parameter) yields a point on the neutral curve in the (Ri_C – Ri_T) plane. The straight line fits for the A_e^2- Ri_T (or Ri_C) data have been obtained and the critical Ri_T (or Ri_C) determined from the plot. The fit statistics along with the critical values of Ri_T and Ri_C are summarized in Table 3.2. Excellent correlations of the data with the straight line fits are obtained for the entire vortex-shedding range of Ri_T and Ri_C.

Fixed parameter	Control parameter	(a, b)×10^3	Critical value of control parameter	Correlation coefficient (%)
$Ri_T = 0.0$	Ri_C	(-9.5, 5.0)	1.90	100
$Ri_T = 0.5$	Ri_C	(-37.6, 32.2)	1.166	99.92
$Ri_C = 0.0$	Ri_T	(-39.4, 30.9)	2.0	99.73
$Ri_C = 0.5$	Ri_T	(-5.5, 2.8)	1.28	99.75

Table 3.2: Statistics for the linear fit $A_e^2 = a + b(\text{control parameter})$ and the determination of points on the neutral curve in (Ri_C - Ri_T) plane

The regime map, within the parametric space of the present study, is obtained by plotting the 3rd order polynomial fit neutral curve based on the points determined by the above exercise, and depicting the steady and the unsteady flow regimes as shown in Fig. 3.5. The dashed line represents the limits of the parametric space spanned in the present study.

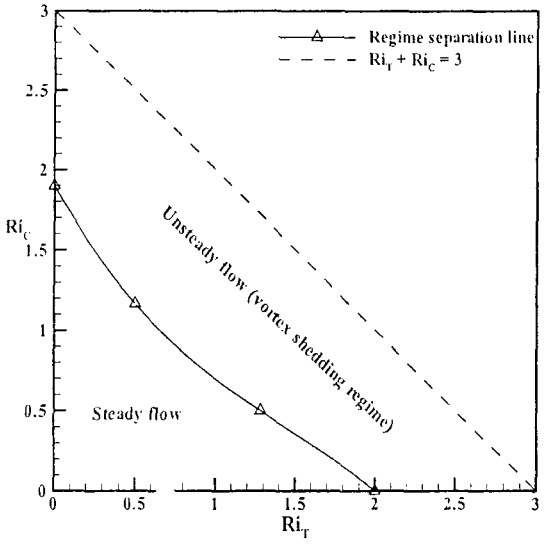

Fig. 3.5: Regime map showing the different flow regimes and the neutral curve

The functional relation representing the neutral curve of the regime map is obtained by fitting a polynomial of order 3 given as,

$$Ri_C = A + B \times Ri_T + C \times Ri_T^2 + D \times Ri_T^3 \qquad (3.9)$$

where; A = 1.900, B = -1.827, C = 0.8123, D = -0.1868.

It is interesting to note from Fig. 3.5 that the critical value of Ri_T at $Ri_C = 0$ is 2.0 where as critical Ri_C at $Ri_T = 0$ is only 1.9. So the plot presented in Fig. 3.5 and / or Eq. 3.9 can be used to predict whether a flow will be steady or unsteady for any combination of values of Ri_T and Ri_C within the range $0 \leq Ri_T \leq 3$, $0 \leq Ri_C \leq 3$.

3.3.2 Steady flow dynamics

Figures 3.6(a), (b) depict the steady state streamline patterns and axial u-velocity profile

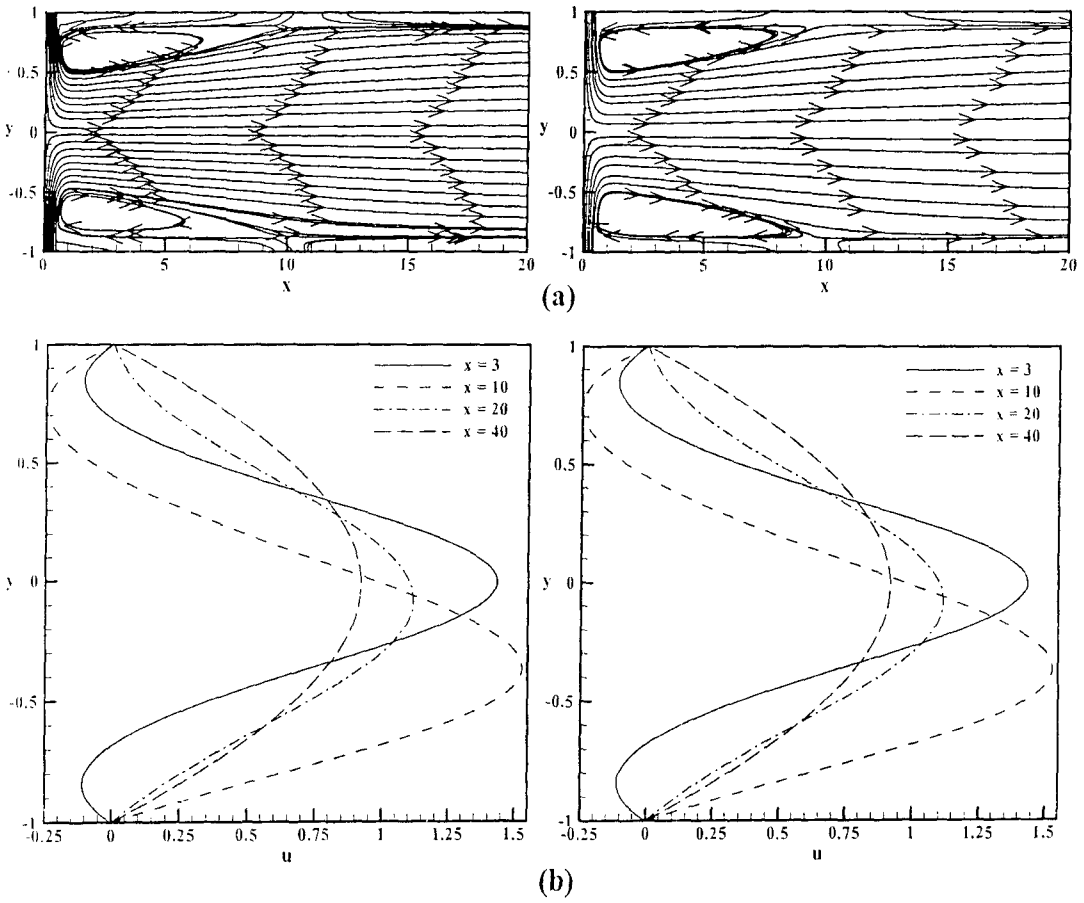

Fig. 3.6: The a) steady state streamline patterns and b) axial velocity profiles at $Ri_T = 0.5$, $Ri_C = 1$ (left) and $Ri_T = 1$, $Ri_C = 0.5$ (right)

observed for (Ri_T, Ri_C) (0.5, 1) (subsequently referred to as case S-I) (left) and (1, 0.5) (subsequently referred to as case S-II) (right) respectively. Owing to the symmetry of the flow pattern about x = 0, the flow patterns in only the right half of the channel are shown. For both cases, the flow patterns are observed to be symmetric about the channel centerline (y = 0). Therefore, the buoyancy forces suppress the symmetry breaking instability found in the case of forced flow (refer Fig. 3.3(b)). Although the size of recirculating zone for case S-II is slightly higher than that for case S-I, interchanging the values of Richardson numbers does not change the flow patterns in the qualitative sense. For case S-I, the flow reattaches at a dimensionless distance of 10.61 from the edge of the inlet port, while for case S-II the reattachment length is observed to be 10.99. The reattachment length has been computed by locating the zero crossing of the wall shear stress. The thermal buoyancy is directed upwards on hot fluid particles ($\theta > 0$) and vice versa, while the intrinsic buoyancy is directed downwards on heavier fluid particles ($\overline{C} > 0$) and vice versa. Therefore the two buoyancy forces add-up to accelerate the fluid in the lower as well as the upper jet / streams.

The u-velocity profiles are four different axial locations are also presented in Fig. 3.6(b) for cases S-I (left) and S-II (right). The development of the flow in the channel is clearly visible with these u-velocity profiles.

It is expected that the flow dynamics would not be affected significantly by exchanging the values of the two Richardson numbers as the net buoyancy aids the fluid inertia of the two streams. This is confirmed from the fact that the reattachment lengths observed for case S-I is very close to that observed for case S-II and the qualitative as well as quantitative nature of the u-velocity profiles at different axial locations is same for the two steady cases under consideration. The slight difference is expected as the

temperature and concentration distributions are not exactly similar leading to slightly different net buoyancy force distributions for the two cases.

Figures 3.7(a), (b) depict the spatial structure of temperature and concentration fields, respectively, represented by isotherm and iso-concentration contour plots for case S-I (Ri_T = 0.5, Ri_C = 1) and S-II (Ri_T = 1, Ri_C = 0.5) respectively. Figure 3.7(a) shows the isotherm patterns for cases S-I and S-II respectively. For both cases, intense thermal mixing and heat transfer is observed near the stagnation point (central portion) as evident from the clustering of the isotherms.

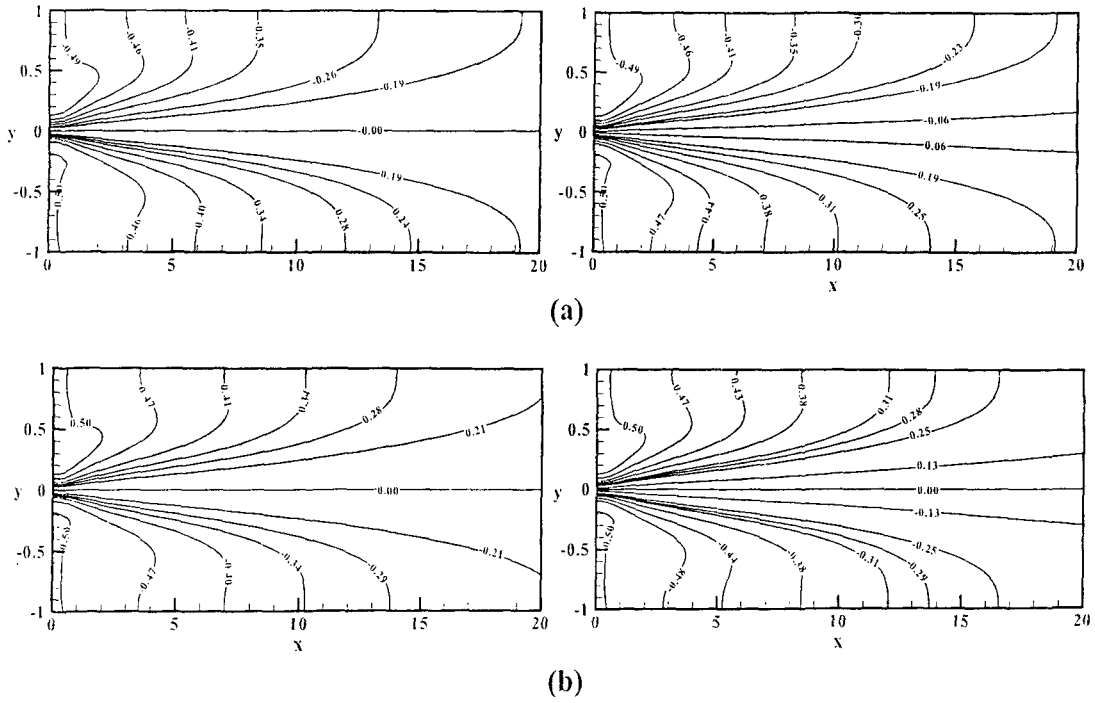

Fig. 3.7: Steady state a) Isotherm patterns and b) Iso-concentration patterns for Ri_T = 0.5, Ri_C = 1 (left) and Ri_T = 1, Ri_C = 0.5 (right) respectively

The spatial structure is very nearly anti-symmetric about y = 0 with colder fluid in the upper half portion and hotter fluid in the lower half. Similarly, the iso-concentration patterns, for the two cases are shown in Fig. 3.7(b), respectively. The anti-symmetry in the flow structure about y = 0 is again observed with high rate of mass transfer near the stagnation point. It is worth observing that from a qualitative view point, the spatial

structure of temperature and concentration fields is almost the same. This is because the relative rates of transport of heat and mass by diffusion as compared to convection, as represented by Prandtl and Schmidt numbers, are nearly equal. For significantly different values of Pr and Sc, the structure of temperature and concentration fields is expected to be dissimilar. Further, there is not much difference between the isotherm and iso-concentration plots for S-I and S-II. This can be attributed to the fact that the two buoyancy forces are not acting independently but as combined buoyancy in both cases S-I and S-II. Since the combined value $Ri_T + Ri_C$ is same for the two cases, the flow structure is also similar.

In order to demonstrate the mixing process, the steady state temperature and concentration profiles at several axial locations are recorded and shown in Figs. 3.8(a), (b) and Fig. 3.9(a), (b) respectively for cases S-I and S-II. Near the channel center, at x = 3.0, large thermal and concentration gradients are observed in a narrow region on either side of the channel centerline. This indicates that mixing is essentially confined in a narrow region around the channel center. As the flow develops along the channel, the

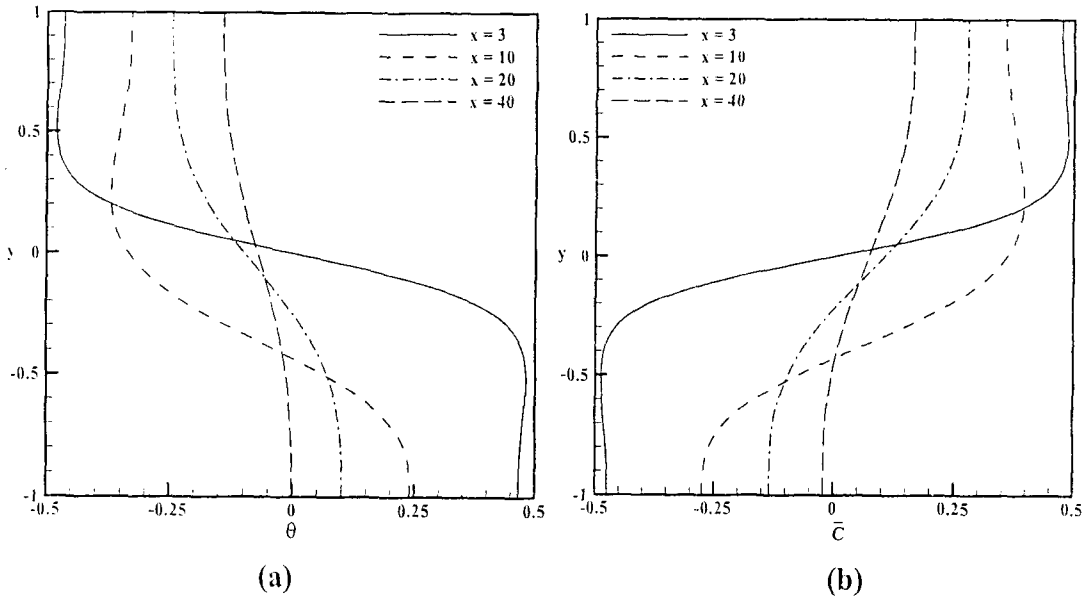

Fig. 3.8: Steady state a) temperature and b) concentration profiles for Ri_T = 0.5, Ri_C = 1

profiles tend to flatten out indicating progressive mixing along the channel length. At x = 40, the profiles become nearly flat with temperature and concentration values very close to their mean (= 0) values.

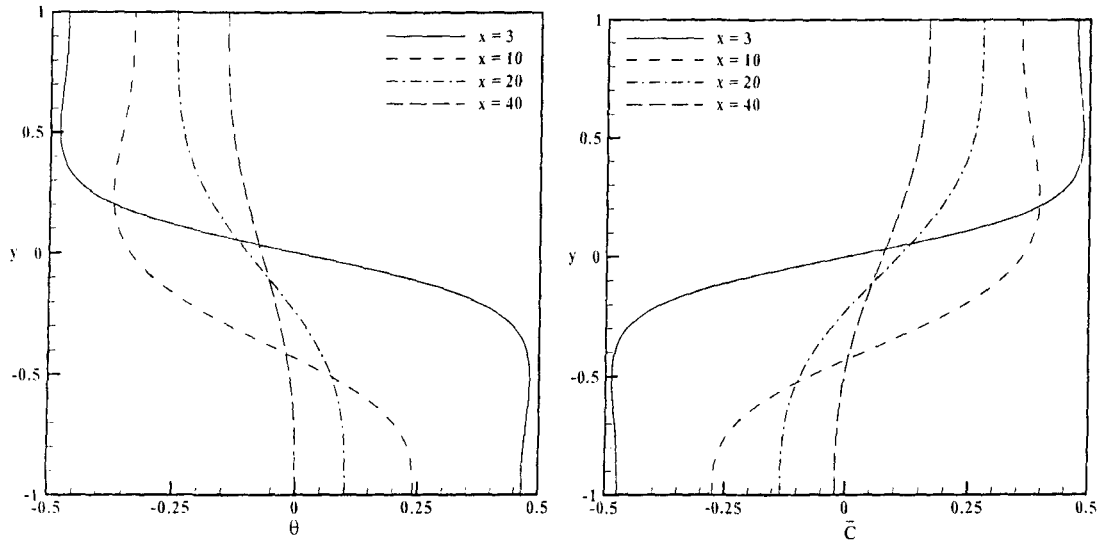

Fig. 3.9: Steady state a) temperature and b) concentration profiles for Ri_T = 1, Ri_C = 0.5

A couple of interesting features are associated with these profiles. Firstly, as hinted earlier, they are anti-symmetric about y = 0. This is because of the symmetry in the velocity field about y = 0 and the choice of thermal and concentration boundary conditions associated with the inlet streams. Secondly, the temperature and concentration profiles at a given axial location are nearly mirror images of each other or *reflectionally symmetric with respect to each other*. Mathematically, this symmetry can be expressed as,

$$\theta(x,y) \cong -\bar{C}(x,y) \tag{3.10}$$

If the y-momentum equation (Eq. 2.12) is examined closely, the above property of the flow field implies that the two buoyancy parameters Ri_T and Ri_C would not behave as two independent parameters, and the net buoyancy (Ri_T + Ri_C) would control the flow dynamics of such a flowfield. The reflectional symmetry of the thermal and

concentration profiles at any axial location is possible for the present configuration owing to (i) the choice of boundary conditions (Eq. 2.17) and (ii) the fact that the thermal mixing and physical mixing processes proceed quantitatively at a similar rate along the channel length. In all the steady flow cases ($Ri_T + Ri_C \leq 1.5$) within the range of parameters considered, it is observed that the buoyancy does not qualitatively affect the flow dynamics. Quantitatively, the flow dynamics is not very sensitive to individual Ri_T / Ri_C values for a fixed value of $Ri_T + Ri_C$. Instead the dynamics is controlled more effectively by the combined value ($Ri_T + Ri_C$).

The change in wall pressure gives a good representation of the power required to pump a fluid in the channel. As already established that the buoyancy forces aid the fluid inertia. Thus it is expected that the pressure drop should decrease with increase in buoyancy. Figure 3.10 shows the variation of upper wall pressure along channel length for certain combinations of Ri_T and Ri_C in the steady flow regime. As expected the pumping pressure decreases with increase in the value of $Ri_T + Ri_C$. The effect of buoyancy is only in the region where two streams are not fully mixed ($x < 60$) and once

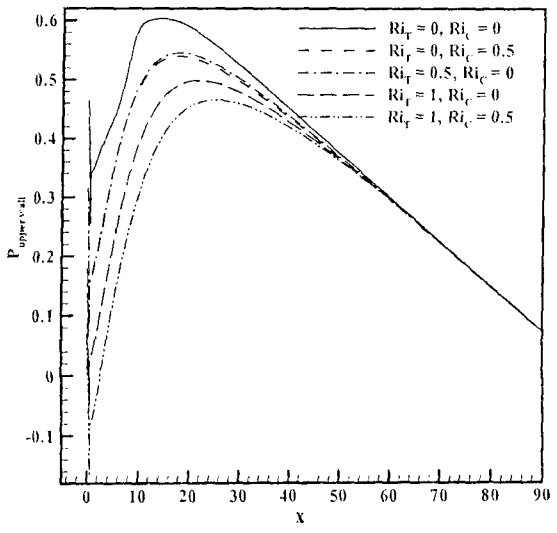

Fig. 3.10: Variation of upper-wall pressure for steady flow cases at different combinations of Ri_T and Ri_C

significant mixing is achieved (beyond x > 60) the buoyancy forces do not cause any significant effect on the wall pressure drop characteristics. Also the effect of interchanging of thermal and concentration Richardson numbers on pumping pressure is insignificant for a fixed value of $(Ri_T + Ri_C)$.

The various features associated with the flow patterns like; the temporal character, symmetries (about channel centerline y = 0), reattachment lengths, L_{ru} and L_{rl}, associated with the upper and lower recirculating zones in the right half of the channel, respectively, are summarized in Table 3.3. An increase in the combined buoyancy level increases the lengths of the recirculation zones. The length of the recirculation zone is directly influenced by fluid velocities and it would increase if fluid velocities increase with increasing level of the combined buoyancy. This is very much evident from the reattachment length data. The quantitative sensitivity of the flowfield to the individual

(Ri_T, Ri_C)	Flow Pattern	L_{ru}	L_{rl}
(0, 0)	Steady, non-symmetric	9.07	2.80
(0, 0.5)	symmetric	8.36	8.36
(0.5, 0)	symmetric	8.49	8.49
(0, 1)	symmetric	9.54	9.54
(1, 0)	symmetric	9.80	9.80
(0, 1.5)	symmetric	10.89	10.89
(1.5, 0)	symmetric	11.25	11.25
(0.5, 1)	symmetric	10.61	10.61
(1. 0.5)	symmetric	10.99	10.99
(0.5, 0.5)	symmetric	9.68	9.68

Table 3.3: Summary of the salient features of the observed flow patterns for the steady flow cases

values of the two Richardson numbers for a given combined buoyancy level is also made evident by the data in Table 3.3. Interchanging the values of the two Richardson numbers alters the reattachment lengths by about 3% only whereas increasing the combined buoyancy brings about a much stronger response in the flowfield data. On comparison with the forced flow case (refer Fig. 3.3) it is quite evident that the buoyancy suppresses the instability which shifts the forced flow from one stable symmetric state to another stable un-symmetric state and for all finite buoyancy cases (steady regime) exact upper-lower half symmetry is maintained.

3.3.3 Unsteady flow dynamics

The flow structure in the unsteady regime is investigated by carrying out

(i) a spatio-temporal data analysis and

(ii) analysis using Proper Orthogonal Decomposition (POD).

The two approaches are presented in the following two sub-sections.

A. *Spatio-temporal data analysis*

In this section, the unsteady flow structure is presented and analysed by generating and examining mean spatial structures via plots of streamlines, isotherms and iso-concentration contour plots, mean flow profiles of temperature and concentration, wall pressures of mean flow and time history of flow variables sampled at specific locations. Along with these mean plots, also presented are instantaneous streamline patterns over a temporal cycle at a particular combination of Ri_T and Ri_C.

Numerical simulations carried out at (Ri_T = 1, Ri_C = 1.5) (case U-I) and at (Ri_T = 1.5, Ri_C = 1) (case U-II) are presented. In both these cases, in the limit of large times, the flow evolves into an oscillatory periodic state. The periodic nature of the flow is clearly depicted in Fig. 3.11 which show the time history of u-velocity at (-15.56, 0) for the two

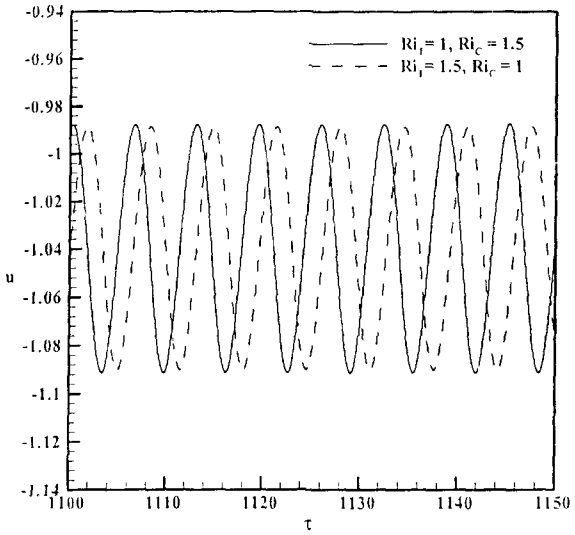

Fig. 3.11: Time history of u (-15.56, 0) at (Ri_T = 1, Ri_C = 1.5) and (Ri_T = 1.5, Ri_C = 1)

cases under consideration. Comparing the time histories for the two cases in Fig. 3.11, it can be readily observed that qualitatively they are same with nearly the same frequencies (0.152) with some phase shift.

Streamline, isotherm and iso-concentration patterns for the mean flow obtained by averaging over a temporal cycle for both the cases U-I (left) and U-II (right) are shown in Figs. 3.12-3.14, respectively. It is quite evident that there is not much difference between

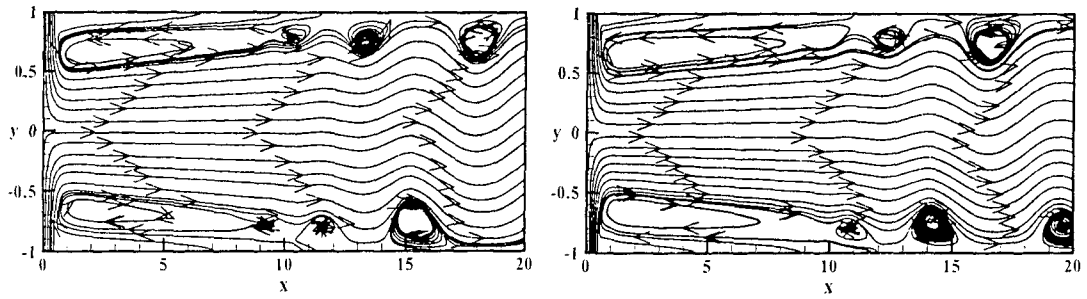

(a) (b)

Fig. 3.12: Mean flow streamline patterns at a) Ri_T = 1, Ri_C = 1.5, b) Ri_T = 1.5, Ri_C = 1

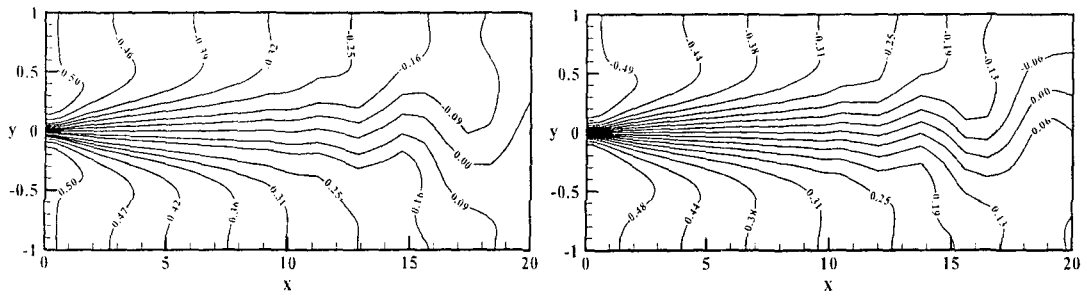

Fig. 3.13: Mean flow isotherm patterns at a) $Ri_T = 1$, $Ri_C = 1.5$, b) $Ri_T = 1.5$, $Ri_C = 1$

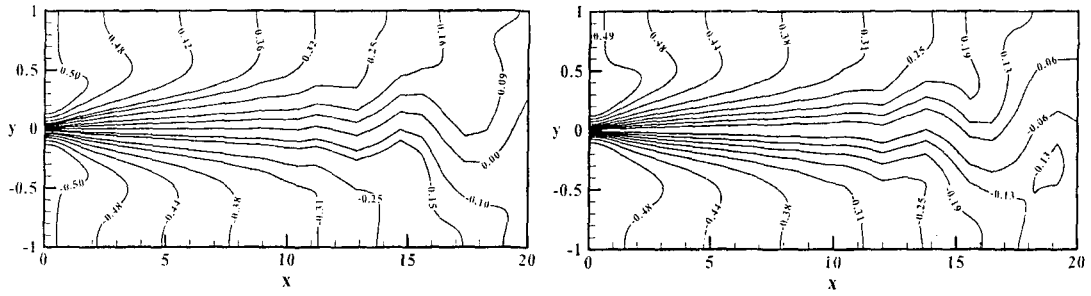

Fig. 3.14: Mean flow iso-concentration patterns at a) $Ri_T = 1$, $Ri_C = 1.5$, b) $Ri_T = 1.5$, $Ri_C = 1$

the spatial structure of the mean flow for the two cases considered. It is interesting to observe that the mean flow structure, in contrast to the steady flow regime, does not possess symmetry about the channel centreline (y = 0). Later, when the structure of the unsteady flowfield is examined in detail, this would be related to the character of the instability leading to the bifurcation from the steady to the unsteady flow regime.

Figures 3.15(a)-(c) and 3.16(a)-(c) depict temperature, concentration and u-velocity profiles for the mean flow, respectively, at four different axial locations for both cases U-I and U-II. As the flow moves along the channel, mixing of two streams takes place which

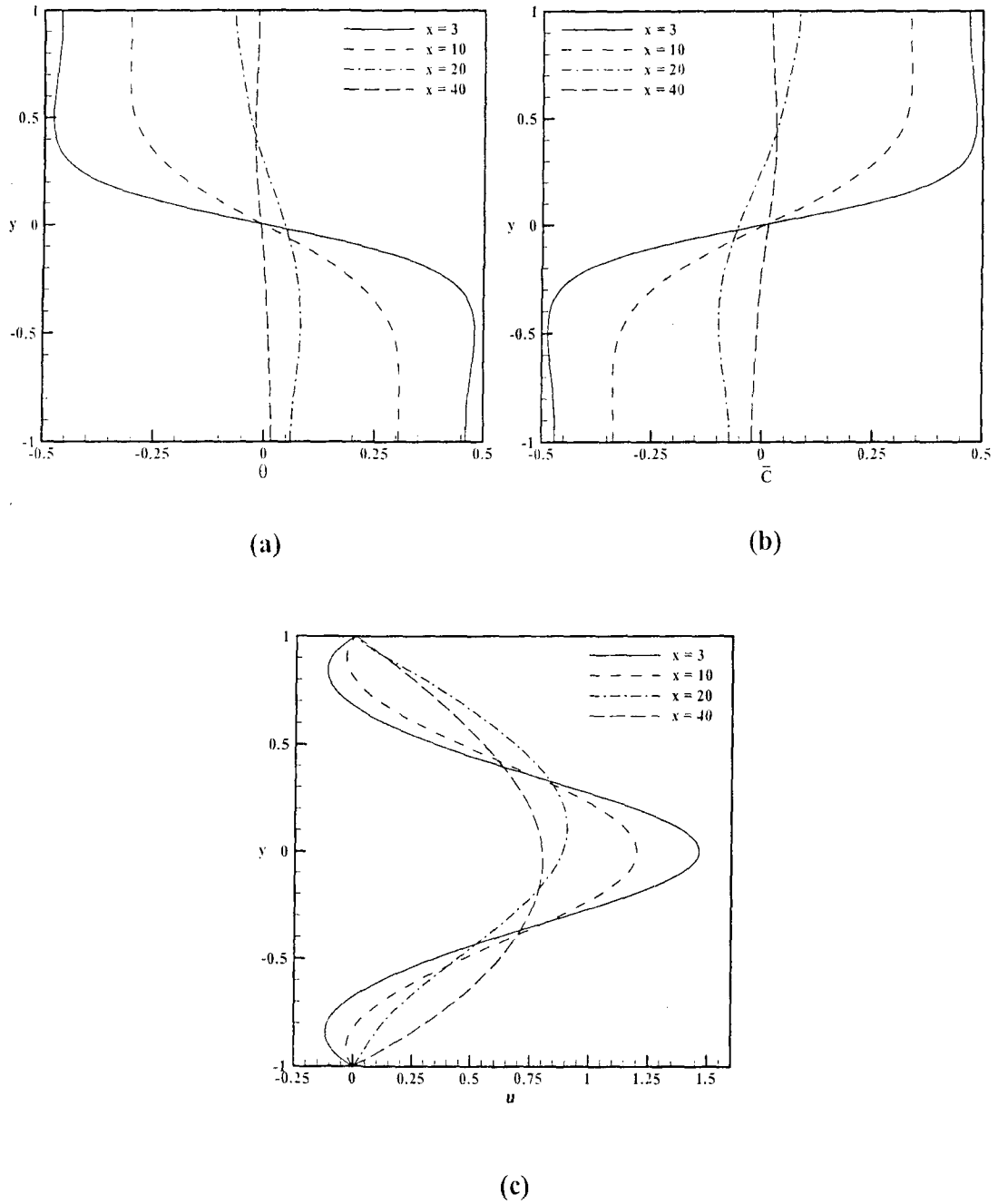

Fig. 3.15: Mean flow profiles of a) temperature and b) concentration c) u-velocity at $Ri_T = 1$, $Ri_C = 1.5$

is indicated by flat profiles of both temperature and concentration at x = 40. No significant difference is visible in the profiles of temperature, concentration and velocity for the two cases U-I and U-II.

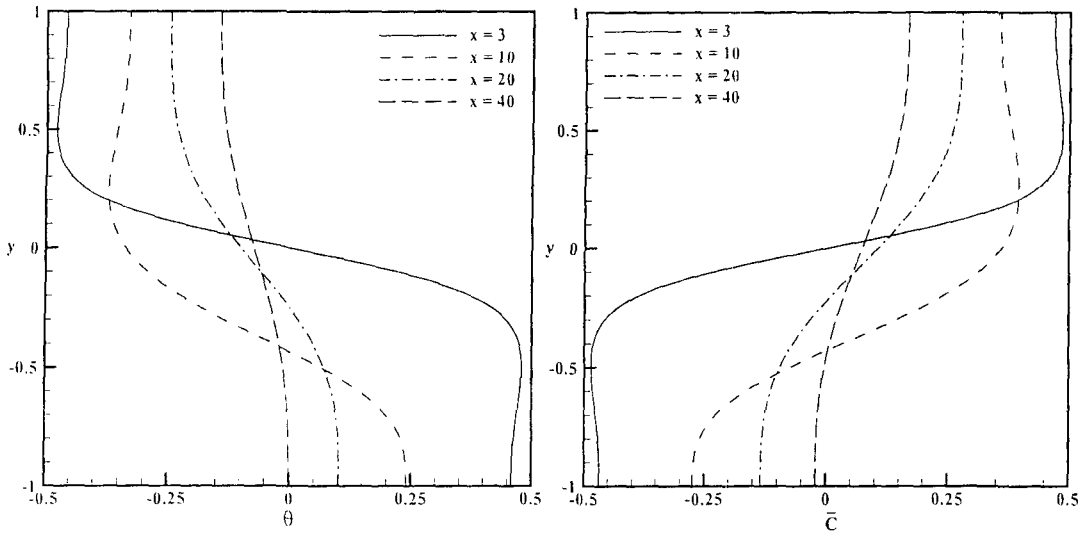

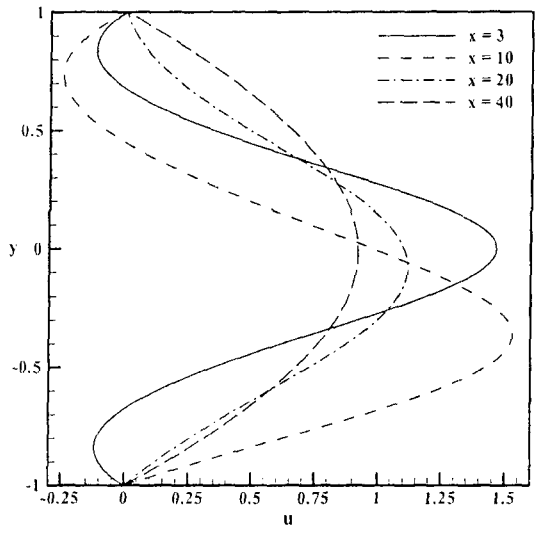

Fig. 3.16: Mean flow profiles of a) temperature and b) concentration and c) u-velocity at $Ri_T = 1.5$, $Ri_C = 1$

In order to observe the effect of increase in buoyancy forces on the flow dynamics in the unsteady regime, simulation is carried out at ($Ri_T = 1.5$, $Ri_C = 1.5$). Figure 3.17 shows

the streamline, isotherms and iso-concentration patterns for the mean flow field at (Ri_T = 1.5, Ri_C = 1.5).

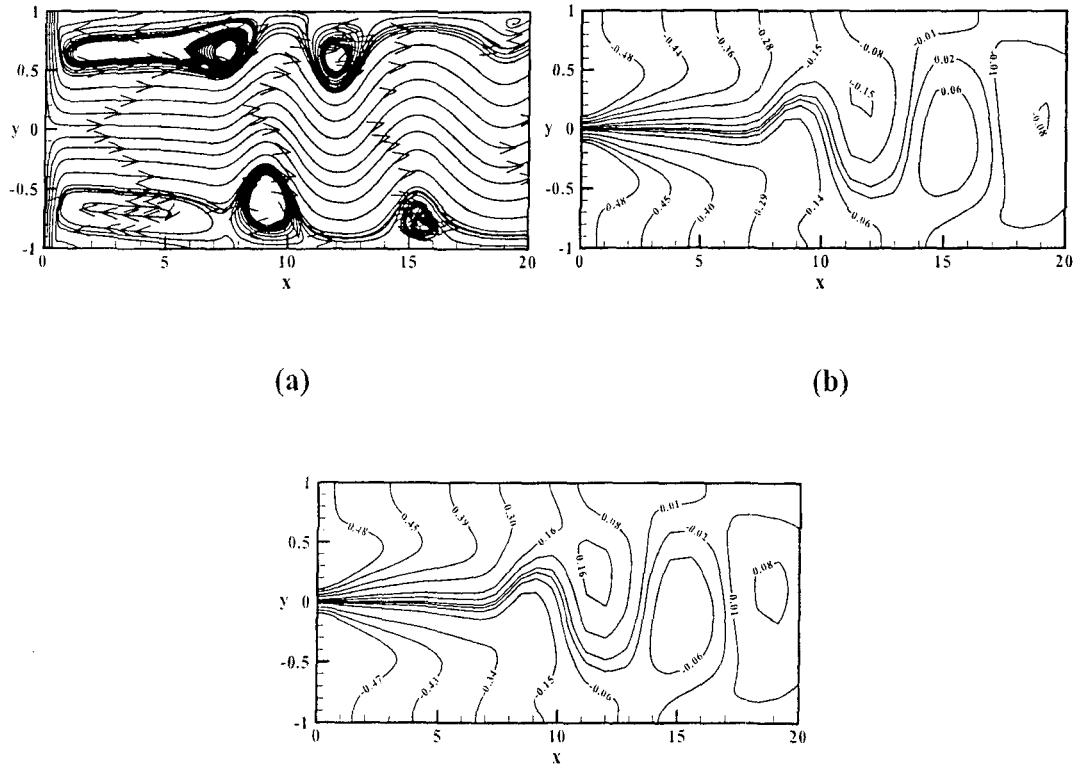

Fig. 3.17: Mean flow a) streamline, b) isotherms and c) iso-concentration patterns at Ri_T = 1.5, Ri_C = 1.5

The spatial structure of the periodic flow is captured through instantaneous streamline patterns over one cycle of oscillations as shown in Figs. 3.18(a)-(h), respectively at (Ri_T = 1, Ri_C = 1.5). The instantaneous snapshots reveal sinuous streamlines beyond the edge of the separation zones (x > 10) with formation of vortices near the channel walls and their subsequent propagation downstream with the flow. Since the streamlines appear to be steady in the flow between the separation zones for x < 10, the unstable perturbation or mode appears as a spatially growing mode along the flow direction. This suggests that the periodic flow is the outcome of a *convective instability*. The time history of u-velocity

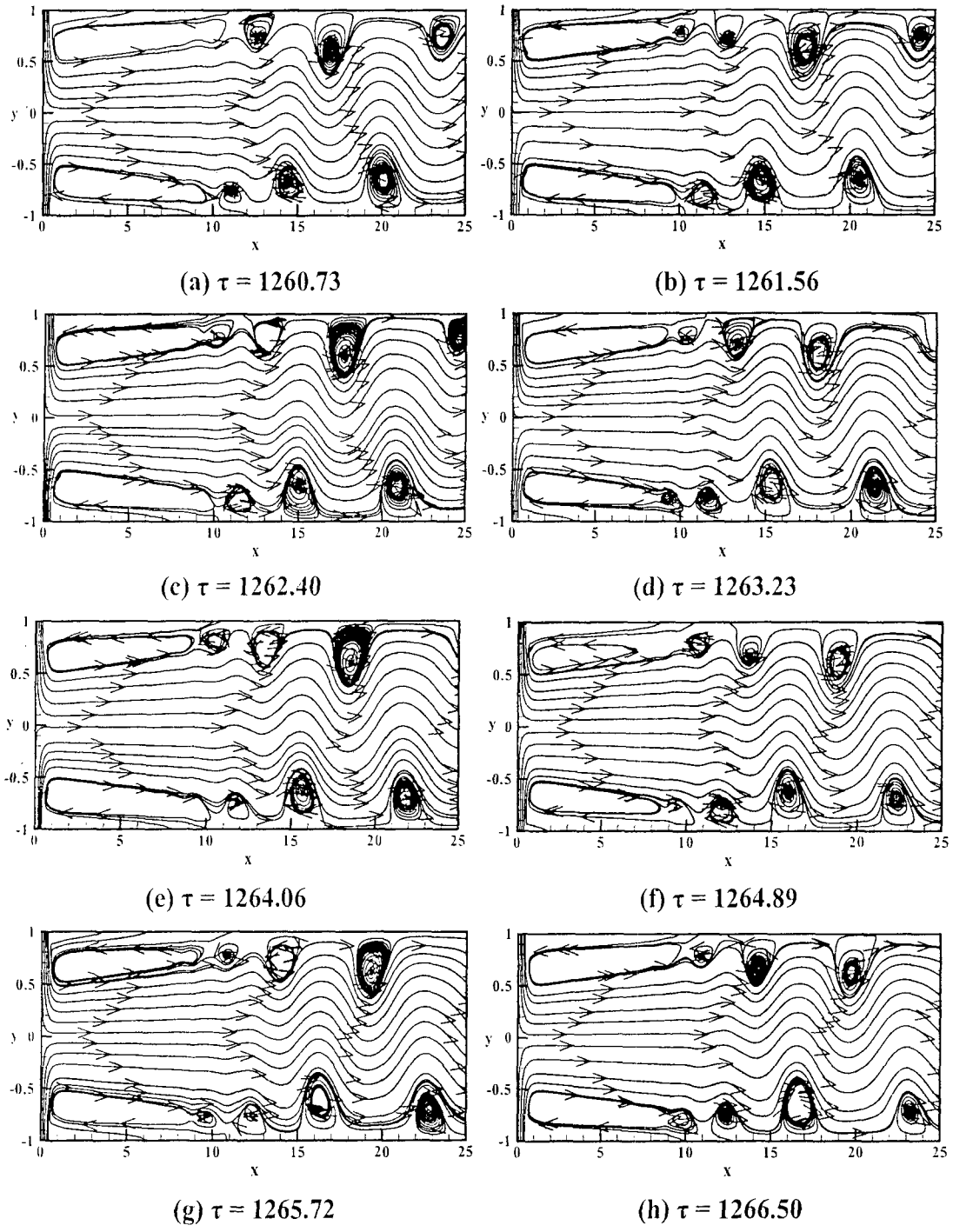

Fig. 3.18: Instantaneous streamline patterns over one temporal cycle of oscillations at $Ri_T = 1$, $Ri_C = 1.5$

at (-0.90, 0) shown in Fig. 3.19(a) clearly shows that the flow is locally steady. The oscillatory spatial growth of the unstable mode is captured in the instantaneous v-velocity profile along the channel centreline at different time instants over one temporal cycle as

shown in Fig. 3.19(b). The profiles show that the perturbation grows rapidly beyond x = 10, reaches a maximum amplitude at around x = 20 and then decreases to very small values for x > 60. Although a slight shift in the perturbation profile is observed over the entire temporal cycle, it is found that the perturbation profile for all times essentially remained confined in the region $10 \leq x \leq 60$. This type of non-propagating structure of the unstable mode clearly suggests the formation of standing waves in the flow domain for x > 10.

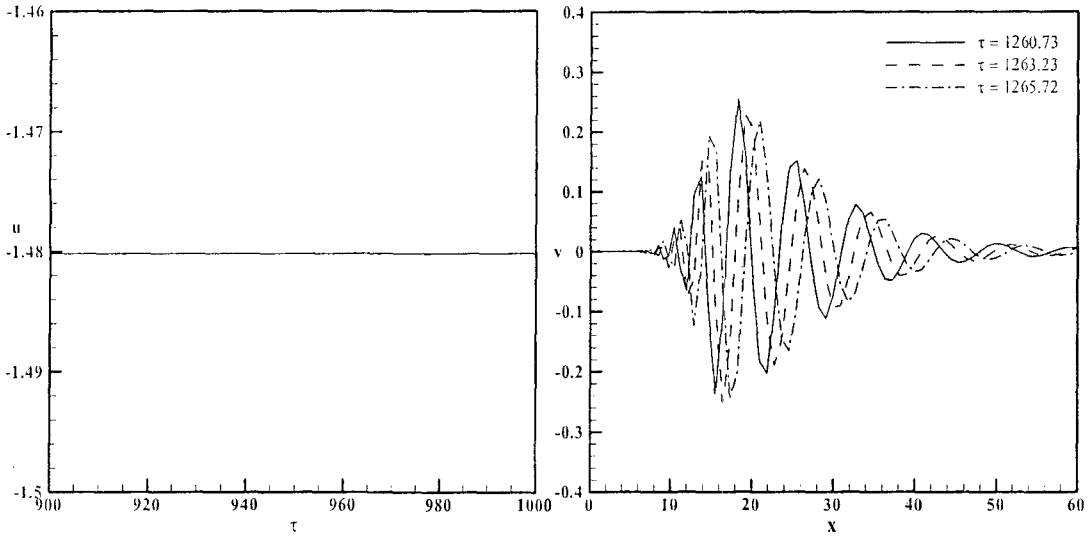

(a) (b)

Fig. 3.19: a) Time history of u (+0.90, 0) and b) the instantaneous v-velocity along channel centerline at different instants of time

Figure 3.20 depicts the mean wall pressure variation at the upper wall along the channel length for unsteady cases for certain combinations of Ri_T and Ri_C and compared with the forced flow case ($Ri_T = 0$, $Ri_C = 0$). The role of buoyancy is to add to the fluid inertia, so increase in the two buoyancy forces show a decrease in the wall pressure. This effect is significant only in the region where mixing of two streams is taking place (x < 60). Once the two streams are mixed, the effect of buoyancy on the wall pressure is not

evident. The spatial oscillations in the mean wall pressure profiles are correlated to the sinuous nature of the mean flow streamline pattern shown earlier (Fig. 3.12).

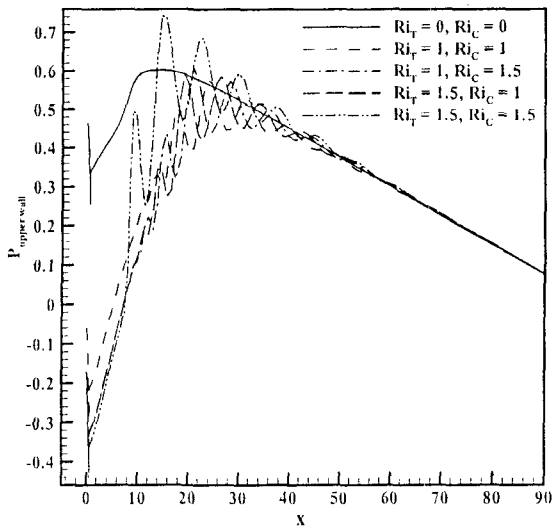

Fig. 3.20: Variation of mean upper-wall pressure for different combinations of Ri_T and Ri_C in unsteady flow regime

The various features of the flow field like; the temporal character, symmetries, reattachment lengths of the top and bottom recirculating zones, and the frequencies of the periodic flow are summarized in Table 3.4 for the various combinations of Ri_T and Ri_C in

(Ri_T, Ri_C)	Flow Pattern	L_{ru}	L_{rl}	Frequency
(0, 0)	Steady, non-symmetric	9.07	2.80	-
(0.5, 1.5)	Mean flow non-symmetric	9.93	10.01	0.154
(1.5, 0.5)	Mean flow non-symmetric	10.58	10.91	0.152
(1, 1.5)	Mean flow non-symmetric	11.33	11.91	0.152
(1.5, 1)	Mean flow non-symmetric	10.82	10.23	0.153
(1, 1)	Mean flow non-symmetric	10.68	11.29	0.151
(1.5, 1.5)	Mean flow non-symmetric	10.90	11.02	0.183

Table 3.4: Summary of the salient flow features for the unsteady flow regime

unsteady flow regime. As the flow is unsteady, the mean values of the reattachment lengths are reported. An increase in the combined buoyancy level increases the lengths of the recirculation zones, which is expected as the role of the buoyancy force is to accelerate the fluid flow in this configuration. In contrast to the steady flow regime, as reported in Table 3.3, the mean flow symmetry in the upper and lower half of the channel does not exist.

Further, in contrast to the steady regime, the unsteady regime exhibits a higher sensitivity of the flow dynamics to the individual values of the thermal and concentration Richardson numbers for a fixed combined buoyancy level. The frequencies of the fluctuating velocity field do not vary with small changes (25%) in combined value of the two Richardson number (Ri_T + Ri_C). But for large change in net buoyancy (50%) the oscillating frequency increases by almost 20%.

B. *POD Analysis*

In order to further examine the structure of the unsteady flow field and to confirm the presence of standing waves in the flow domain, a POD analysis is carried out. The proper orthogonal decomposition (POD) provides a basis for the modal decomposition of an ensemble of complex spatio-temporal data with the objective of extracting the dominant structures [56]. In the context of fluid mechanics, the data ensemble comprises of the flow field information obtained from a number of experiments (physical or numerical) or the information of an unsteady flow field at different time instants from a single experiment. Once the spatial structure of the ensemble is captured in the spatial basis functions or modes, the members of the ensemble can be represented as linear superposition of these modes given as Eq. 3.11.

$$\mathbf{U}(\mathbf{x}, \tau) = \sum_{1}^{\infty} a^{(p)}(\tau)\, \psi^{(p)}(\mathbf{x}) \tag{3.11}$$

The proper orthogonal basis provides the advantage such that finite truncations of the modal expansion of the ensemble members yields the smallest error in the mean-square sense compared to the any other orthogonal bases having the same dimension. In the context of fluid mechanics, this means that the structure of a complex spatio-temporal field like the velocity field could be captured in an average sense by a relatively small number of POD modes. POD is a fairly well established statistical tool which is being used in other disciplines like random variables [57], image processing [58], signal analysis [59], data compression [60], process identification control in chemical engineering [61] and oceanography [62]. It is also known as: Karhunen-Loève Decomposition, Principal Components Analysis, and Singular Value Decomposition. It was used in the context of fluid mechanics for the first time by Lumley [63]. Most of the studies regarding application of POD in fluid flow problems have been limited to the understanding of the dynamics of turbulent flows. However, some studies have also been reported in literature for unsteady laminar flows such as Hasan et. al. [64], Hasan and Sanghi [65], and Mishra et. al. [66].

In the present context a spatio-temporal data ensemble $\mathbf{U}^i = \mathbf{U}(\mathbf{x}, \tau_i)$, i = 1,....,M, representing the snapshots of the fluctuating flow field over one temporal cycle is considered. At each point, the vector **U** is constructed by four values corresponding to the two components of velocity, temperature and concentration fields of the fluctuating field. Symbolically this is expressed as, $(U_1, U_2, U_3, U_4) \equiv \left(u'', v'', \theta'', \overline{C''}\right)$. A composite data ensemble is considered in order to incorporate the inherent coupling between the velocity and the temperature as well as concentration fields for the present problem. This approach is similar to the one adopted by Podvin and Quéré [67].

The K-L basis functions $\{\psi\}$ are thus vector functions with four components at each point (ψ_1, ψ_2, ψ_3, ψ_4) corresponding to the two components of fluctuating velocity, the thermal and concentration fields.

Method of snapshots as proposed by Sirovich [68] is employed to determine the POD basis function $\{\psi\}$. The procedure is given in detail by Hasan and Sanghi [65] and described here in brief.

Let $\{\mathbf{U}^i, i = 1,....M\}$ represent M snapshots of the fluctuating flow field. Then, the following algebraic eigenvalue problem can be utilized to obtain the POD basis functions or modes,

$$\mathbf{BZ} = \lambda \mathbf{Z} \tag{3.12}$$

In Eq. (3.12), **B** is a real symmetric square matrix of size M X M and λ is the associated eigenvalue. The matrix **B** is built utilizing the snapshots $\mathbf{U}^{(i)}$ as,

$$B_{ij} = \frac{1}{M} (\mathbf{U}^{(i)}, \mathbf{U}^{(j)}). \tag{3.13}$$

In the present context, since the vector U is composed of four scalars at a point, the projection or the inner product employed in Eq. 3.13 is defined as,

$$(\mathbf{U}^i, \mathbf{U}^j) = \int_{\tilde{A}} (U_1^{(i)}U_1^{(j)} + U_2^{(i)}U_2^{(j)} + s_1 U_3^{(i)}U_3^{(j)} + s_2 U_4^{(i)}U_4^{(j)}) d\tilde{A} \tag{3.14}$$

The scaling factors s_1 and s_2 must be introduced to account for the inherent differences in the scaling of the different flow variables U_1, U_2, U_3 and U_4 as suggested by Lumley and Poje [69]. In the present study, the values of s_1 and s_2 are chosen as unity since the various components U_1, U_2, U_3 and U_4 are scaled so as to yield values which are of comparable order of magnitude and not vastly different.

The POD eigenvalues are always non-negative [56] and once these eigenvalues and the corresponding eigenvectors are determined from Eq. 3.12, the POD spatial basis functions or POD spatial modes $\{\psi\}$ can be determined as,

$$\psi^{(p)} = Z^{(p)}_{(i)} U^{(i)}, \qquad (p, i) = 1,2,.....M \tag{3.15}$$

The basis functions are further normalized such that,

$$(\psi^{(p)}, \psi^{(p)}) = 1.0, \tag{3.16}$$

and the temporal coefficients $a^{(p)}(\tau)$ can then be determined as,

$$a^{(p)}(\tau_i) = (\mathbf{U}^{(i)}, \psi^{(p)}). \tag{3.17}$$

Further, arranging the eigenvalues in the descending order as $\lambda^1 > \lambda^2,.....$, the corresponding eigenfunctions $\psi^1, \psi^2, ...$, represent a hierarchical set of dominant spatial structures of the spatio-temporal data.

In order to ascertain the proper size of the data ensemble to be employed in the method of snapshots, sets of 16, 32, 64 and 128 snapshots of the unsteady, periodic flow field are recorded over one temporal cycle of the periodic flow. The mean field of each set is extracted and the corresponding sets of fluctuating flow snaps **U** are constructed. For each set of $\mathbf{U}^1$, the method of snapshots is employed to determine the eigenvalues. Table 3.5 presents leading five eigenvalues for the different sets of data at $Ri_T = 1$, $Ri_C = 1.5$. Essentially, the idea is to assess the effect of increasing the size of the data ensemble

	M = 16	**M = 32**	**M = 64**	**M = 128**
λ_1	1.852	1.851	1.851	1.851
$\lambda_2 \times 10$	4.042	4.079	4.088	4.090
$\lambda_3 \times 10^2$	1.146	1.160	1.164	1.165
$\lambda_4 \times 10^3$	2.709	2.853	2.885	2.892
$\lambda_5 \times 10^4$	1.206	1.304	1.326	1.335

Table 3.5: Convergence of leading POD eigenvalues with increasing number of snapshots in the data ensemble for Ri_T =1, Ri_C = 1.5

on the few leading eigenvalues. It can be readily observed that the leading three eigenvalues converge within 1% for $M \geq 32$. For the fourth and fifth eigenvalues, it takes more than 32 snapshots to converge within less than 1%. However, these eigenvalues are quite small and their contribution to the total energy is quite negligible. Therefore an ensemble size of 32 snapshots is considered to be appropriate.

Figure 3.21 shows the eigenspectrum obtained with a data ensemble of 32 snapshots over one temporal cycle of the flow at $Ri_T = 1$, $Ri_C = 1.5$. The spectrum clearly confirms

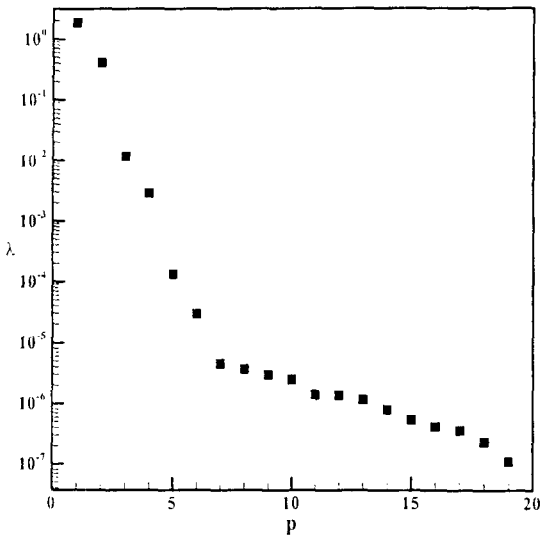

Fig. 3.21: The POD eigenspectrum obtained from the unsteady fluctuating field data for ($Ri_T = 1.0$, $Ri_C = 1.5$)

the presence of standing waves in the flow domain as no degeneracy is observed and all the eigenvalues are distinct (Podvin and Le Quéré [67], Rempfer and Fasel [70], , Aubry et. al. [71]).

The temporal and spatial structure of the first three leading POD modes is shown in Fig. 3.22(a), (b) respectively. The temporal structure of the POD modes is captured by the temporal coefficients $a^{(1)}(\tau)$, $a^{(2)}(\tau)$ and $a^{(3)}(\tau)$ while the spatial structure is captured by the associated eigenfunctions or the basis functions. As the POD modes represent the

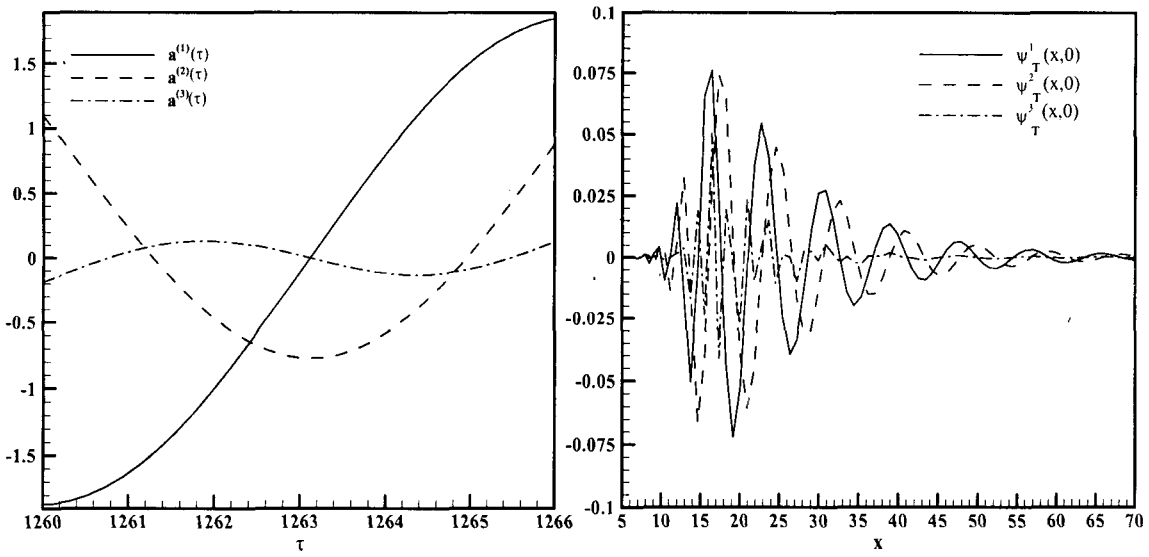

(a) (b)

Fig. 3.22: The (a) temporal and (b) spatial structure of the leading three POD modes at (Ri_T = 1, Ri_C = 1.5)

fluctuating flow field only, it follows from Eq. 3.11 that the temporal mean of each POD mode must vanish. This implies that $< a^{(p)}(\tau) >= 0$ for each POD mode. This can be observed in Fig. 3.22(a). Further, the eigenvalues 'λ' associated with each mode represent the amount of energy in the mean square sense contributed by each mode to the total energy, in the mean square sense, of the fluctuating flowfield. Mathematically, this implies that $< \left(a^{(p)}(\tau)\right)^2 > (\psi^{(p)}, \psi^{(p)}) = < \left(a^{(p)}(\tau)\right)^2 > = \lambda^{(p)}$. The structure of the temporal coefficients in Fig. 3.22(a) clearly reflects these properties. Figure 3.22(b) shows the spatial structure of the temperature eigenfunctions along the channel centreline for the leading three modes. The spatial structure of the standing waves is clearly captured by these leading eigenfunctions.

This type of an unsteady flow structure is interesting and has not been reported in the earlier studies on such geometries involving fluid flow and heat transfer. This "vortex-shedding" phenomenon can be corroborated from the earlier work of Pawlowski et al. [44] who also reported a vortex-shedding bifurcation in a similar configuration involving

isothermal opposed stream interaction. Such a bifurcation was reported at sufficiently high jet / stream Re. This suggests that if sufficiently high velocities are generated in the jet-like flow formed between the two separation zones, then it develops instabilities which show up in the form of sinuous streamlines beyond a certain distance from the center. In the present context, this also explains the existence of such instability only at large net buoyancy levels which accelerate the streams and consequently the jet-like flow to large enough speeds. These instabilities in turn generate localized vortices near the walls which gradually propagate downstream with the flow. This flow structure is interesting and as shown later, it would affect the mixing process significantly.

3.3.4 Mixing Characteristics

In this section the effect of buoyancy on the thermal and physical mixing characteristics are presented and analyzed. As mentioned in §3.3, the state of mixing at any location along the channel length is expressed quantitatively by the scalar measure termed as Mixing Index defined via Eq. (3.3). In the discussion to follow, the normalized mixing index for temperature and concentration, would be symbolically denoted as $<MI_T>$ and $<MI_C>$, respectively.

As pointed out earlier, the mixing index can be defined either using simple averages or the mass weighted / bulk averages. The simple average based index at a particular axial location essentially gives a measure of uniformity or flatness in the profile of temperature / concentration at that location. However, from thermodynamic considerations, the bulk averages represent the thermal / concentration states that are achievable via an adiabatic, mixing flow process of two steady streams like the one under consideration. Therefore, an index based on bulk averages is a *direct* measure of the degree or the extent to which these bulk values have been attained, on an average, by the fluid particles at a particular

axial location. The index based on the simple averages is more of an *indirect* measure of mixing as the simple averages would *approach* the bulk averages as the mixing proceeds and the flow approaches a fully developed state. Thus in order to monitor the progress of mixing for the entire length of the passage, the bulk-based normalized mixing index is preferred.

A comparison of bulk-based and simple average based normalized mixing indices for temperature and concentration for the forced flow is depicted in Fig. 3.23(a) and Fig. 3.23(b) respectively. The simple average based characteristics deviate from the bulk based characteristics only for the initial phase of the mixing process ($x < 10$) with bulk based characteristic showing a slower rate of mixing than the simple average based one. However, as expected, the two characteristics tend to overlap as the thermal and concentration gradients across the channel reduce. This clearly indicates that the characteristics of mixing based on bulk and simple averages would tend to differ significantly when the fluid is in a strong state of in-homogeneity or large gradients of

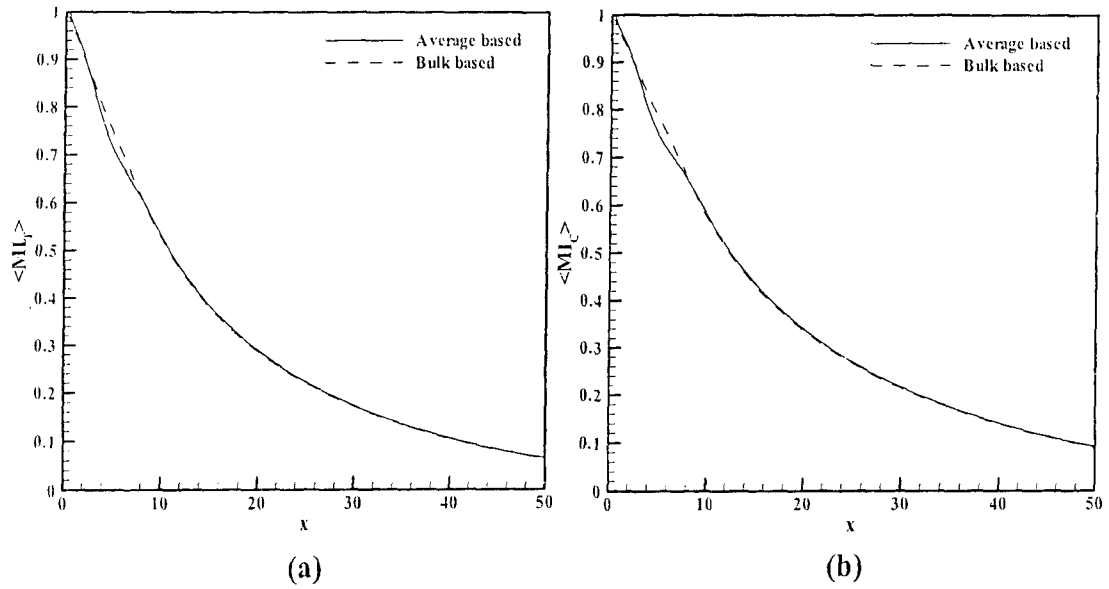

Fig. 3.23: Comparison between bulk based and simple average based normalized mixing index for a) temperature and b) concentration for the forced flow

temperature / concentration. This could be significant if not only the temperature / concentration but also the bulk velocities of the two streams are unequal in the context of the present problem. Therefore, in general, the bulk basis is considered a more natural choice to represent the mixing characteristics quantitatively.

The impact of buoyancy on the thermal and physical mixing characteristics for different Ri_T and Ri_C is shown in Fig. 3.24(a) and 3.24(b) respectively. For the unsteady cases, the mixing index has been estimated from the time mean flow field data averaged over one periodic cycle of the flow. The impact of formation of standing waves in the channel for x > 10 is quite *profound*. The standing waves *enhance* the rate of mixing (both thermal as well as physical) quite significantly. For the steady cases, where standing waves are absent, the mixing characteristics are not much sensitive to the buoyancy effects. In section 3.3.2, it was established that the effect of switching of Ri_T and Ri_C, for a fixed level of combined buoyancy, has only a weak effect on the flow dynamics. From Fig. 3.24 it is evident that switching of Ri_T and Ri_C, also, does not have any prominent effect on mixing characteristics as well. Therefore, the combined buoyancy ($Ri_T + Ri_C$),

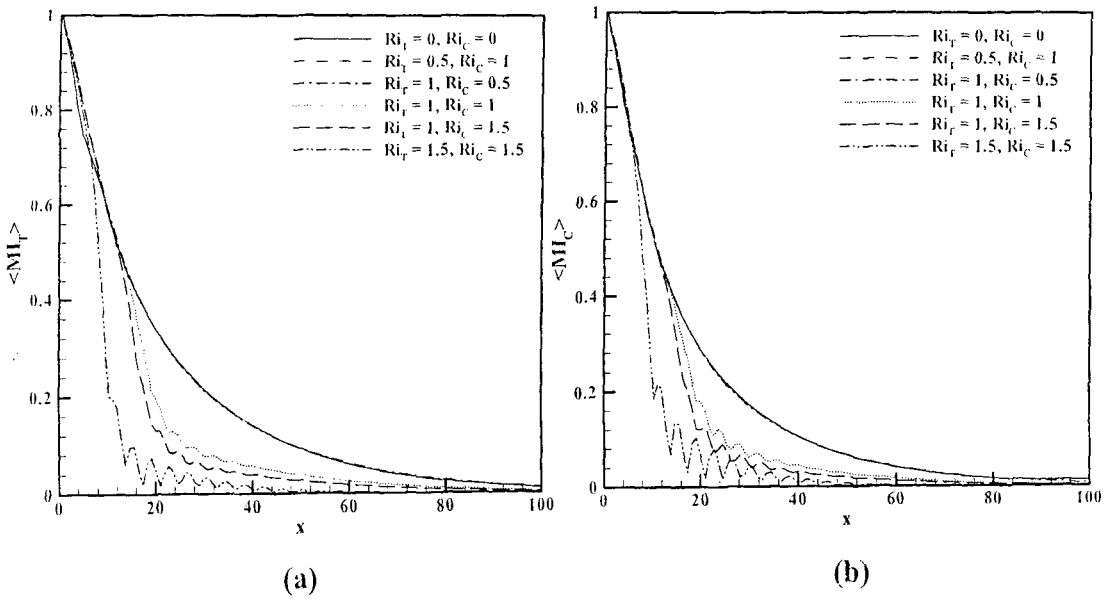

(a) (b)

Fig. 3.24: The impact of buoyancy on a) thermal and b) physical mixing characteristics for both steady and unsteady cases

rather than individual thermal and concentration buoyancies, is controlling the thermal and physical mixing. Increase in net buoyancy further enhances the mixing phenomena in the unsteady flow regime characterized by the formation of standing waves.

In order to quantitatively correlate the mixing characteristics to the various operating parameters like the two Richardson numbers in the context of the present study, mixing lengths can be defined as the length from the center of the channel (x = 0) where a particular level of mixing is achieved. This is analogous to defining boundary layer thickness, jet widths or width of mixing layers in free shear flows. In particular, we choose a mixing index of 0.1 to define the mixing length that yields 90% mixing level. Symbolically this mixing length is denoted as L_m. Since the mixing lengths for thermal and physical mixing would be different in general, therefore they would be symbolically denoted as L_{mT} and L_{mC} respectively. The values of these lengths can be readily estimated from the mixing index characteristics by computing the length where the characteristic crosses the value of 0.1.

Tables 3.6(a) and 3.6(b) summarize the values of mixing lengths estimated for

	(Ri_T, Ri_C)	L_{mT}	L_{mC}
Forced Flow	(0, 0)	41.26	48.10
Finite Buoyancy Configuration in steady flow regime	(0, 0.5)	41.34	48.27
	(0.5, 0)	41.24	48.14
	(0, 1)	41.04	48.04
	(1, 0)	40.81	47.80
	(0, 1.5)	40.71	47.80
	(1.5, 0)	40.37	47.41
	(0.5, 1)	41.21	48.42
	(1, 0.5)	41.26	48.10
	(0.5, 0.5)	40.92	47.92

Table 3.6a: Thermal and physical mixing lengths for different combinations of Ri_T and Ri_C in the steady flow regime

	(Ri_T, Ri_C)	L_{mT}	L_{mP}
Forced Flow	(0, 0)	41.26	48.04
Finite Buoyancy Configuration in unsteady flow regime	(0.5, 1.5)	23.18	26.30
	(1.5, 0.5)	25.92	29.67
	(1, 1.5)	21.89	22.42
	(1.5, 1)	20.81	23.92
	(1, 1)	25.03	26.11
	(1.5, 1.5)	13.20	13.39

Table 3.6b: Thermal and physical mixing lengths for different combinations of Ri_T and Ri_C in the unsteady flow regime

the various combinations of Ri_T and Ri_C in both the steady and unsteady flow regimes respectively. The forced flow case has been included for comparison purposes. The buoyancy does not affect the mixing rates significantly in the steady flow regime. This is a direct consequence of the fact that in the steady flow regime, for the cases investigated, the flow features do not exhibit a strong sensitivity to the buoyancy effects (see Table 3.3). The unsteady flow that results due to the convective instability, leading to the formation of standing waves, is accompanied by a sharp drop in the values of the mixing lengths. The values drop by more than 40% indicating that the mixing process is significantly accelerated or enhanced by the unsteady standing wave formation. This is a significant finding of the present work.

The physical reason for the enhancement of the mixing rate can be attributed to the sinuous type of the flow pattern associated with the standing waves. As the fluid particles move forward, their transverse excursions or motions across the channel cross section not only generate a mechanical 'churning' or 'stirring effect but also increase the residence time of the fluid particles over a certain length of the passage. The sinuous motion would also introduce strong *axial gradients*, in addition to the transverse gradients, that increase the overall molecular transport rate of momentum, heat and mass. The effect is similar to

that of a flow in a channel with transverse baffles placed in order to create a sinuous flow pattern leads to enhanced mixing. In the present context, a similar effect is created more naturally through instabilities. This is clearly more advantageous than the use of baffles, as baffles would induce a large pressure drop and hence would require more pumping power for a given flow rate. In unsteady cases, increase in buoyancy further enhances the mixing and it is reflected in nearly 40% reduction in mixing length when (Ri_T + Ri_C) increases from 2 to 3.

Figures 3.25(a) and 3.25(b) represent graphically, the functional relation between the thermal and physical mixing lengths and the two Richardson numbers. In order to highlight the effects of buoyancy the mixing lengths have been normalized by the corresponding forced flow values. The points corresponding to unsteady flows are enclosed by squares to distinguish from points corresponding to steady flows. As established by Table 3.6(a) and 3.6(b), the affect of unsteadiness is quite prominent on the mixing of two streams, as large reduction in the mixing lengths is evident for unsteady flows.

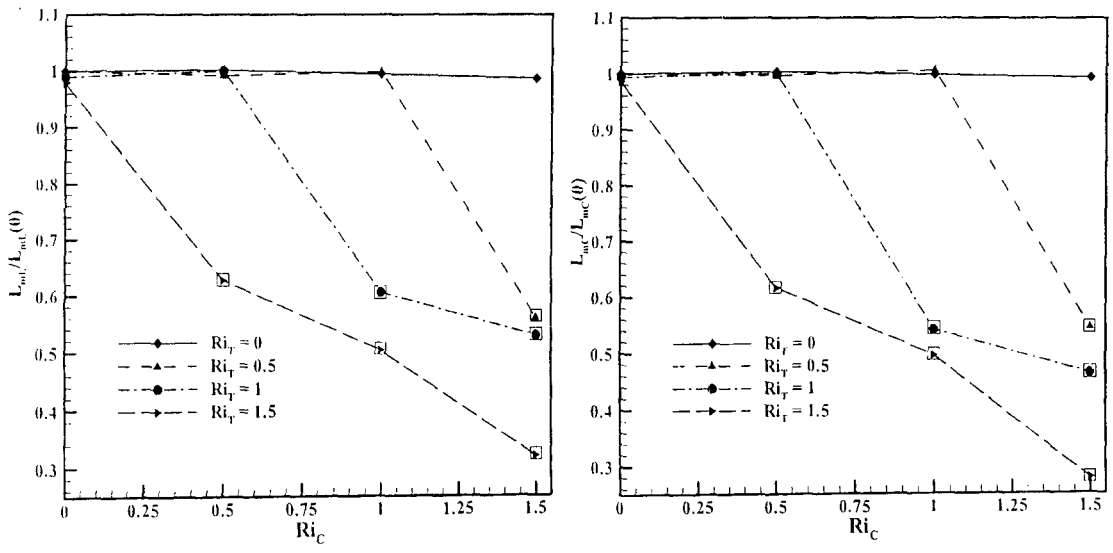

Fig. 3.25: a) Temperature and b) concentration normalized mixing lengths at different combinations of Ri_T and Ri_C

As described earlier in §3.3, another quantitative measure of mixing is Buoyancy Mixing Effectiveness (e_m). Buoyancy mixing effectiveness (e_m) gives a measure of how effective buoyancy is, in controlling the mixing of two interacting jets. A positive value of e_m means buoyancy is effective in enhancing the mixing and vice versa. Tables 3.7(a) and 3.7(b) provide the data of temperature and concentration buoyancy mixing effectiveness

(Ri_T, Ri_C)	e_{mT} (%)	e_{mC} (%)
(0, 0.5)	4.85	1.88
(0.5, 0)	5.37	2.37
(0, 1)	5.15	1.99
(1, 0)	6.22	3.00
(0, 1.5)	5.55	2.18
(1.5, 0)	7.18	3.73
(0.5, 1)	2.87	0.37
(1, 0.5)	3.55	2.80
(0.5, 0.5)	5.69	2.49

Table 3.7a: Thermal and physical buoyancy mixing effectiveness for different combinations of Ri_T and Ri_C in the steady flow regime

for the steady and unsteady flow regimes respectively. As already explained, the buoyancy forces do not effect mixing significantly in the steady flow regime. However, in the unsteady regime, the instabilities leading to the formation of a standing wave, drastically enhance the thermal as well as the physical mixing.

(Ri_T, Ri_C)	e_{mT} (%)	e_{mC} (%)
(0.5, 1.5)	50.55	49.01
(1.5, 0.5)	44.03	42.11
(1, 1.5)	59.81	58.53
(1.5, 1)	58	57
(1, 1)	49	48
(1.5, 1.5)	82.02	82.01

Table 3.7b: Thermal and physical buoyancy mixing effectiveness for different combinations of Ri_T and Ri_C in the unsteady flow regime

For unsteady cases, there is more than ten-fold increase in both thermal and physical buoyancy mixing effectiveness, as compared to the steady cases. Increase in buoyancy in the unsteady regime, further enhances mixing and nearly 60 % increase in effectiveness is observed at $(Ri_T + Ri_C) = 3$ as compared to $(Ri_T + Ri_C) = 2$.

3.4 Summary

After carrying out appropriate numerical tests to ensure channel length independence and grid independence of the numerical results, a value of $\ell = 100$ employing a 379×129 grid is considered appropriate.

Forced flow ($Ri_T = 0$, $Ri_C = 0$) case is considered to highlight the effect of thermal and intrinsic buoyancy on flow dynamics. The forced flow case settled into a long term steady non-symmetric state about the channel centerline.

The effect of thermal and intrinsic buoyancy on the structure and dynamics of the flow due to impingement of two equal velocity jets is established by varying the thermal and concentration Richardson numbers. In the range of Ri_T and Ri_C considered, two different flow regimes, namely, steady and unsteady regimes, are obtained. For all the cases considered, a combined buoyancy value of $(Ri_T + Ri_C) \leq 1.5$ (irrespective of their individual values), the flow pattern is observed to be steady in the long term. For $(Ri_T + Ri_C) \geq 2$, the flow showed an unsteady, oscillatory behavior with vortex-shedding.

It is established using Landau theory that the transition from the steady regime to the unsteady regime is a *supercritical Hopf bifurcation.* A complete regime map, within the parametric space of the present study, is generated by plotting the critical values of Ri_T and Ri_C (neutral curve obtained by using the Landau theory). The regime map clearly identifies the steady and the unsteady flow regimes in the parametric space of $(Ri_T$-$Ri_C)$. A curve fit relation representing the neutral curve is obtained as,

$$(Ri_C)_{crit} = A + B \times Ri_T + C \times Ri_T^2 + D \times Ri_T^3$$

where; A = 1.900, B = -1.827, C = 0.8123, D = -0.1868.

Flow patterns in the steady regime show an exact upper and lower half symmetry, apart from left right symmetry which is maintained for all flow simulations taken. The symmetry breaking exchange of stability observed for the forced flow is suppressed by buoyancy. The effect of interchanging the values of the two Richardson numbers, keeping the combined buoyancy fixed, is very weak on the flow dynamics in the steady flow regime.

The plots of temperature and concentration profiles at several axial locations reveal that both thermal and concentration gradients are observed in a narrow region on either side of the channel centerline. This is indicative of the fact that mixing is essentially confined in a narrow region around the channel center. The temperature and concentration profiles at a given axial location are nearly mirror images of each other or reflectionally symmetric which can be attributed to the boundary conditions chosen as well as the nearly similar values of Pr and Sc chosen.

The change in wall pressure gives a measure of the power required to pump the fluids in the channel. As the effect of buoyancy is to aid the fluid inertia, therefore increase in the two buoyancy forces is accompanied by a decrease in the wall pressure. This effect is significant only in the region where two streams are not fully mixed ($x < 60$). Once the two streams are mixed, the effect of buoyancy on the wall pressure is not significant.

In the unsteady flow regime, the instantaneous v-velocity profile along the channel centerline at different time instants over one temporal cycle exhibit oscillatory spatial growth of the unstable mode with the perturbation growing rapidly between $x = 10$ along the flow direction while the flow remains steady in the upstream zone $x < 10$. This

suggests that the flow becomes *convectively unstable* at sufficiently large buoyancy forces.

The structure of the unsteady flow field is examined further via Proper Orthogonal Decomposition (POD) analysis. The POD eigenspectrum obtained with a data ensemble of 32 snapshots over one temporal cycle of the flow establishes the presence of *standing waves* in the flow domain as no degeneracy is observed and all the eigenvalues are distinct.

It is shown that the thermal and physical mixing process along *the channel length* can be effectively monitored by the scalar measure termed as 'Mixing Index' utilized in the present work. For the purpose of design and performance assessment of such flow systems or mixing devices, a performance parameter termed as 'Mixing Length' is proposed in the present work. The parameter is shown to be effective in characterizing the overall mixing process. In the steady flow regime, the mixing length is not very sensitive to the two Richardson numbers. The acceleration of the fluid streams, caused by the buoyancy forces, increases the fluid velocities in the channel. This, in turn, increases the transverse gradients and hence the molecular transport rates of mass and energy. However, concurrently, this is offset to a large extent by the corresponding decrease in the residence time of the fluid particles between two sections of the channel. Therefore, the effect of buoyancy forces on the mixing process and the associated length is not very significant in the steady regime.

For the unsteady periodic flow with standing waves the mixing process is significantly enhanced with the mixing length for $(Ri_T + Ri_C) = 3$ reducing by almost 70% than the corresponding forced flow value. The formation of standing waves lead to a sinuous flow pattern with the fluid particles following a wavy path. This has a two-fold effect; i) an increase in axial and transverse velocity gradients and, ii) a significant

increase in residence time. Both of these factors contribute to the enhanced mixing. Further, in the unsteady regime, increase in buoyancy further accelerates the mixing and it is reflected in nearly 40 % reduction in mixing length when (Ri_T + Ri_C) increases from 2 to 3.

Another quantitative measure which quantifies the effectiveness of buoyancy, termed as 'Buoyancy Mixing Effectiveness' (e_m) is also proposed. A positive value of e_m means buoyancy enhances mixing as compared to the forced flow under similar conditions and vice versa. For unsteady cases, both thermal and physical buoyancy mixing effectiveness is roughly 10 times (in some cases more than 10 times) than that for the steady cases. Increase in buoyancy in the unsteady regime, further enhances mixing and nearly 60 % increase in effectiveness at (Ri_T + Ri_C) = 3 as compared to (Ri_T + Ri_C) = 2, is observed.

In the next chapter, the effect of velocity ratio (VR) on the flow structure and dynamics, along with its effect on thermal and physical mixing of the two jets / streams is examined.

Chapter 4

Effect of Velocity Ratio on Flow Dynamics and Mixing

In this chapter the effect of velocity ratio (VR) on the flow dynamics as well as mixing of the two jets in the forced as well as the mixed convection regime is presented. For this purpose, numerical simulations are carried out for VR = 0.5 and VR = 2.0 and compared with the equal velocity cases presented in the previous chapter. This chapter is divided into four sections. The forced flow ($Ri_T = Ri_C = 0$) cases for different Velocity Ratios are reported in §4.1. The effect of Velocity Ratio on the flow structure (temporal and spatial) and its subsequent effect on the thermal and physical mixing is examined in §4.2. Finally a brief summary of the chapter is given in §4.3.

4.1 Forced Flow

The case of forced flow i.e. ($Ri_T = 0$, $Ri_C = 0$) for different velocity ratios has been included in order to assess the difference in the forced flow dynamics as well as to isolate the effects of thermal and intrinsic buoyancy forces on the flow. As reported in §3.2 that forced flow case for VR = 1, exhibited multiple steady states (symmetric and unsymmetric), with transition from the steady symmetric flow pattern for shorter times ($\tau < 700$) to *steady stable non-symmetric state* for long time integrations ($\tau > 1000$). However no such transition is recorded for unequal velocity jets (VR = 0.5, 2) and both cases of unequal velocity ratio exhibit a single long time steady states. Therefore, the instability that causes transition from one steady state to another, for VR = 1, is suppressed when the velocities of the two impinging jets are different. The growth of the instability and the transition from the steady symmetric unstable mode to a steady non-

symmetric stable mode for VR = 1 and long time stable steady state for VR = 0.5, 2 is captured in the time history of u-velocity at (-15.56, 0) as shown in Fig. 4.1.

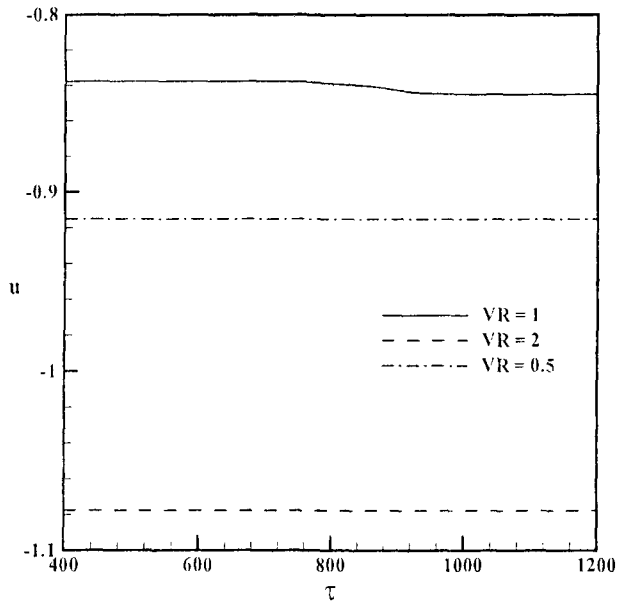

Fig. 4.1: The time history of u(-15.56, 0) at (Re = 200, h = 2.0) for VR =0.5, 1 and 2

Figure 4.2 depicts forced flow steady state streamline plots for VR = 0.5, 2 and 1.

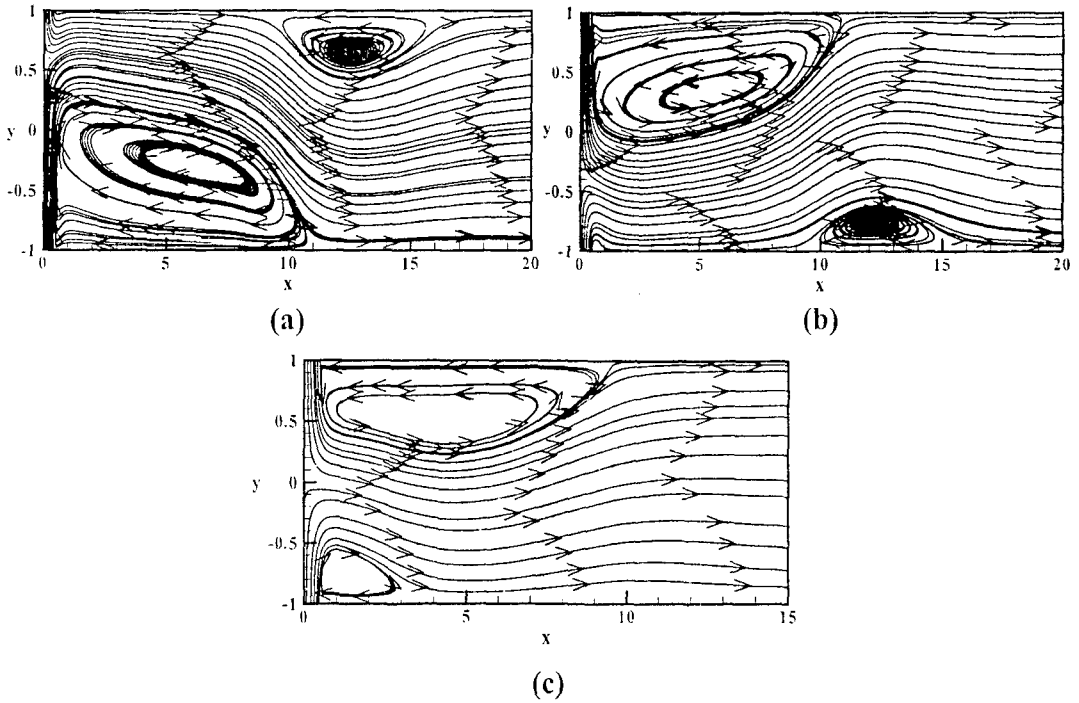

Fig. 4.2: Forced flow steady state streamline plots for a) VR = 0.5, b) VR = 2 and c) VR = 1

When the velocities of the two jets are equal, the impingement point is at (0, 0) or center of the channel as seen in Fig 4.2 (c), but when the velocities of the two jets become unequal, the impingement point gets shifted towards the side of lower speed jet as depicted in Figs. 4.2 (a), (b). The stream patterns for VR = 0.5 and 2 exhibit a reflectional symmetry about the channel centerline (about x-axis). This is expected considering that there is no buoyancy.

Figure 4.3 depict steady state lower-wall pressures at VR = 0.5, 1 and 2 for forced flow case. As evident from Figs. 4.2(a) and 4.2(b), larger recirculating zone is attached to the wall (upper or lower) opposite to the jet having lesser velocity (upper wall for VR = 0.5 and lower wall for VR = 2). So the wall pressure, for unequal velocity ratio jet cases, is expected to be higher on the wall where smaller or no recirculating zone exists i. e. on lower wall at VR = 2 (Fig. 4.3) and on upper wall at VR = 0.5 (not shown).

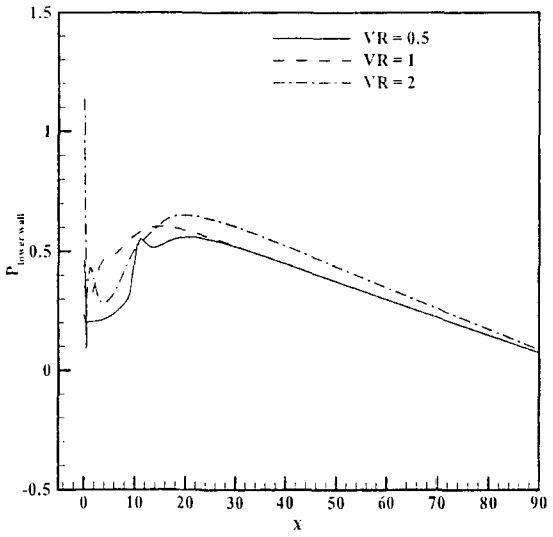

Fig.4.3: Steady state lower wall pressure plots for forced flow at VR = 0.5, 1 and 2

4.2 Buoyancy Effects

The effects of buoyancy at different velocity ratios, on the structure and dynamics of the flow are reported in this section and compared to those for the equal velocity jets

presented in the previous chapter. A complete regime map with neutral curve is obtained, within the parametric space of thermal and concentration Richardson numbers, for different velocity ratios, using the approach described in the previous chapter. Flow structure for both steady and unsteady regimes is investigated by generating plots of instantaneous streamlines, isotherms and iso-concentration contours. In addition to these plots, temperature, concentration and u-velocity profiles are also generated at different streamwise or axial locations. Wall pressure plots are presented to illustrate the effect of change in velocity ratio on the pumping pressure. The mixing characteristics are reported and compared with those for equal velocity jets.

4.2.1 Flow regimes

Within the parametric domain of the current study, all cases of lower jet with double velocity (VR = 0.5) are steady, where as for VR = 2, three cases with (Ri_T, Ri_C) combinations, namely, (1, 1.5), (1.5, 1) and (1.5, 1.5) are unsteady. As reported in §3.3.1, all combinations of thermal and intrinsic Richardson numbers with combined value (Ri_T + Ri_C) greater than 2 are unsteady for equal velocity ratio jets.

The approach of obtaining the critical Richardson number: (Ri_T or Ri_C) using Landau theory (described in the previous chapter) is employed to obtain approximately the neutral curve separating the steady and unsteady flow regimes in the parametric space spanned by $0 \leq Ri_T \leq 3$ and $0 \leq Ri_C \leq 3$. The regime map, within the parametric space of the present study, is obtained by plotting the 3rd order polynomial fit neutral curve and depicting the steady and the unsteady flow regimes as shown in Fig. 4.4. The functional relation representing the neutral curve of the regime map is obtained by fitting a polynomial of order 3 given as,

$$Ri_C = A + B \times Ri_T + C \times Ri_T^2 + D \times Ri_T^3 \qquad (4.1)$$

where, A = 2.360, B = -1.214, C = 0.2102, D = -0.0266.

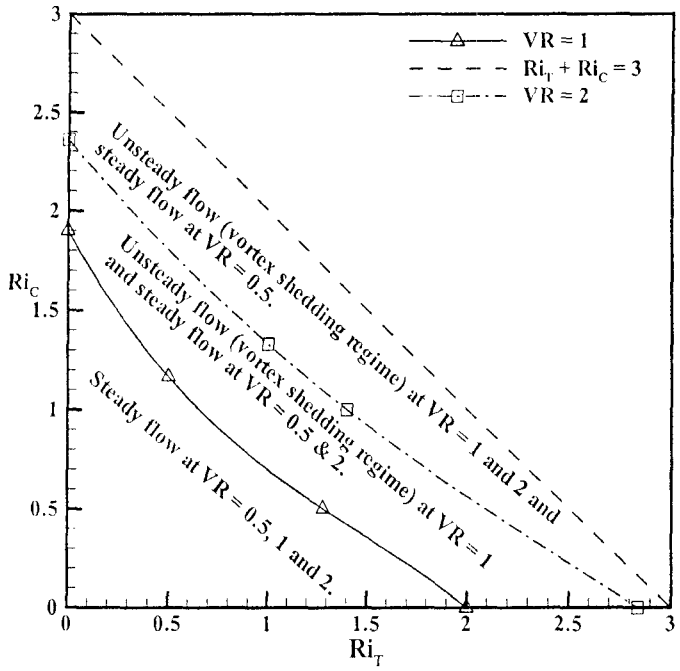

Fig.4.4: Regime map showing the different flow regimes and the neutral curve at VR = 1 and 2

The critical value of Ri_T at $Ri_C = 0$ is 2.84 where as critical Ri_C at $Ri_T = 0$ is only 2.36. The corresponding critical values at VR = 1, as reported in §3.3.1 are $Ri_T = 2$ (at $Ri_C = 0$) and $Ri_C = 1.9$ (at $Ri_T = 0$). So the plot presented in Fig. 4.4 and / or Eq. 3.9 and Eq. 4.1 can be used to predict whether a flow will be steady or unsteady for any combination of values of Ri_T and Ri_C within the range $0 \leq Ri_T \leq 3$, $0 \leq Ri_C \leq 3$ at VR = 1 and VR = 2. The regime map shows that the neutral curve for VR = 2.0 shifts towards higher values of (Ri_T, Ri_C) suggesting that the asymmetry introduced in the flow due to the unequal bulk velocities of the two jets results in a more stable flow than the flow caused by the interaction of equal velocity jets. In fact for VR = 0.5, no instabilities are encountered within the range of Ri_T and Ri_C considered. Therefore, the onset of the bifurcation / instability causing the transition from the steady to the unsteady regime is delayed for the unsymmetric flow scenarios.

4.2.2 Steady flow dynamics

Figures 4.5 (a)-(c) present steady state streamline patterns for VR = 0.5, 2 and 1 respectively at Ri_T = 0.5 and Ri_C = 1.0. The streamline patterns for unequal velocity jets (VR =0.5, 2) show a single large vortex formed on the side of jet having higher speed while the vortex on the opposite side is nearly negligible. On comparing Figs. 4.5 (a) and 4.5(b) with Figs. 4.2(a) and 4.2(b), it is evident that the larger vortex has grown in size as

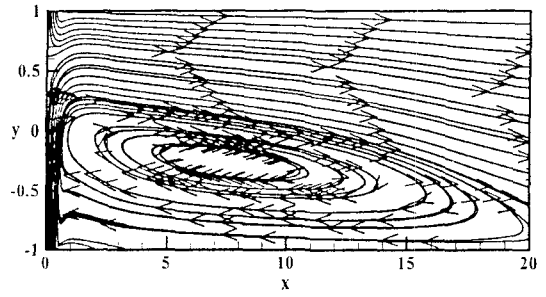

(a) VR = 0.5

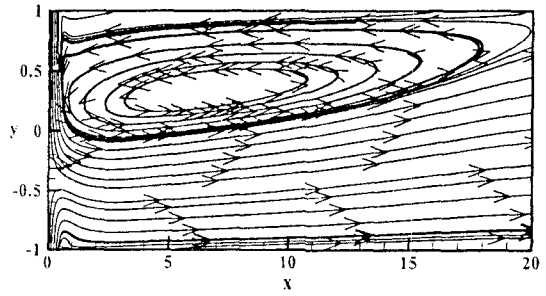

(b) VR = 2

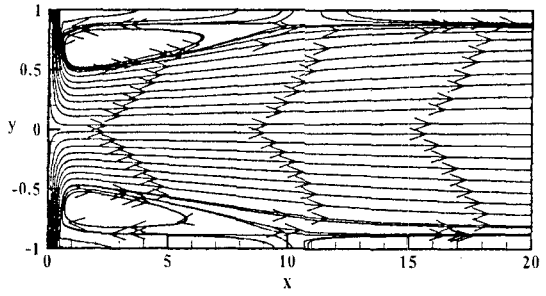

(c) VR = 1

Fig. 4.5: The streamline patterns at Ri_T = 0.5, Ri_C = 1.0 for a) VR = 0.5, b) VR = 2 and c) VR = 1

regards to forced flow, for both unequal velocity jet cases. For VR = 1, the upper and lower vortex formed near the impingement region cause the stream after impingement to

expand like flow through a venturi. For unequal velocity ratio cases, the vortex, on the side of lower velocity jet, is eliminated and therefore the basic flow dynamics of equal and unequal velocity ratio cases is different. From a geometric viewpoint, the streamline patterns for VR = 0.5 and VR = 2.0 appear to be mirror images or reflectionally symmetric about y = 0. For lower buoyancy case too, streamline patterns for VR = 0.5 and VR = 2 remain reflectionally symmetric as is reported for forced flow cases (refer Fig. 4.2 and Figs. 4.5(a)-(b)).

To examine the effect of interchanging the Richardson number (Ri_T, Ri_C) for a fixed combined buoyancy level, the streamline patterns and u-velocity profiles at different axial locations at $Ri_T = 1$ and $Ri_C = 0.5$ for VR = 0.5 (left) and VR = 2 (right) are shown in Fig.

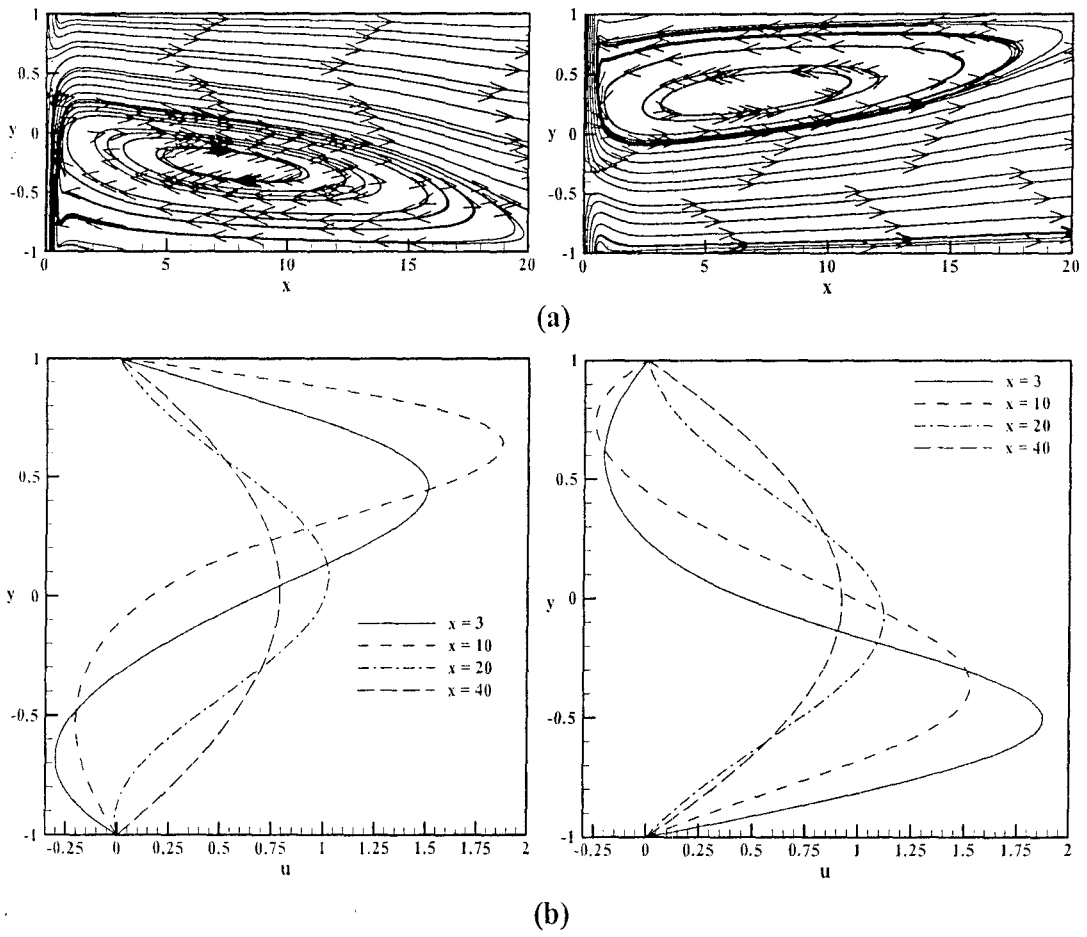

Fig. 4.6: The a) streamline patterns and b) u-velocity profiles at different axial locations at $Ri_T = 1$, $Ri_C = 0.5$ for VR = 0.5 (left) and VR = 2 (right)

4.6(a) and Fig. 4.6(b) respectively. On comparison of stream plots at $Ri_T = 0.5$, $Ri_C = 1$ (Figs. 4.5(a), (b)) and at $Ri_T = 1$, $Ri_C = 0.5$ (Fig 4.6 (a)), it is quite evident that switching of Richardson number does not qualitatively effect the flow pattern for unequal velocity ratio jets in steady regime. Therefore at other Richardson numbers, for steady flow regime, the effect of interchanging the Richardson numbers on flow structures is not explicitly reported.

The u-velocity profiles at different axial locations for VR = 0.5 (left) and VR = 2 (right) at $Ri_T = 1$, $Ri_C = 0.5$ are presented in Fig. 4.6(b). While the streamline patterns for VR = 0.5 and VR = 2.0 may appear to be reflectionally symmetric, it is quite evident from the profiles that the actual flowfield, in the quantitative sense, does not exhibit such a symmetry. This is along expected lines as the buoyancy forces will in general not permit such symmetries.

Figures 4.7(a) and 4.7(b) compare the steady state isotherm and iso-concentration patterns for VR = 0.5, 2 and 1 at $Ri_T = 0.5$, $Ri_C = 1$ respectively. High rates of heat and mass transfer are observed near the impingement point which is shifted in upper half for VR = 0.5 and in lower half for VR = 2. Further, the functional anti symmetry about y = 0 for isotherms and iso-concentration plots as seen in equal velocity ratio cases is removed in unequal velocity ratio cases. Also the spatial structure of isotherms and iso-concentration plots for same VR are similar owing to nearly same rates of heat and mass transfer as dictated by nearly equal Pr and Sc numbers.

In order to demonstrate the mixing of two streams, the steady state temperature and concentration profiles for VR = 0.5, 1 and 2 at $Ri_T = 0.5$, $Ri_C = 1$ at several axial locations have been recorded and shown in Figs. 4.8 (a)-(c). Near the stagnation point, at x = 3.0, large thermal and concentration gradients are observed for all velocity ratios. This

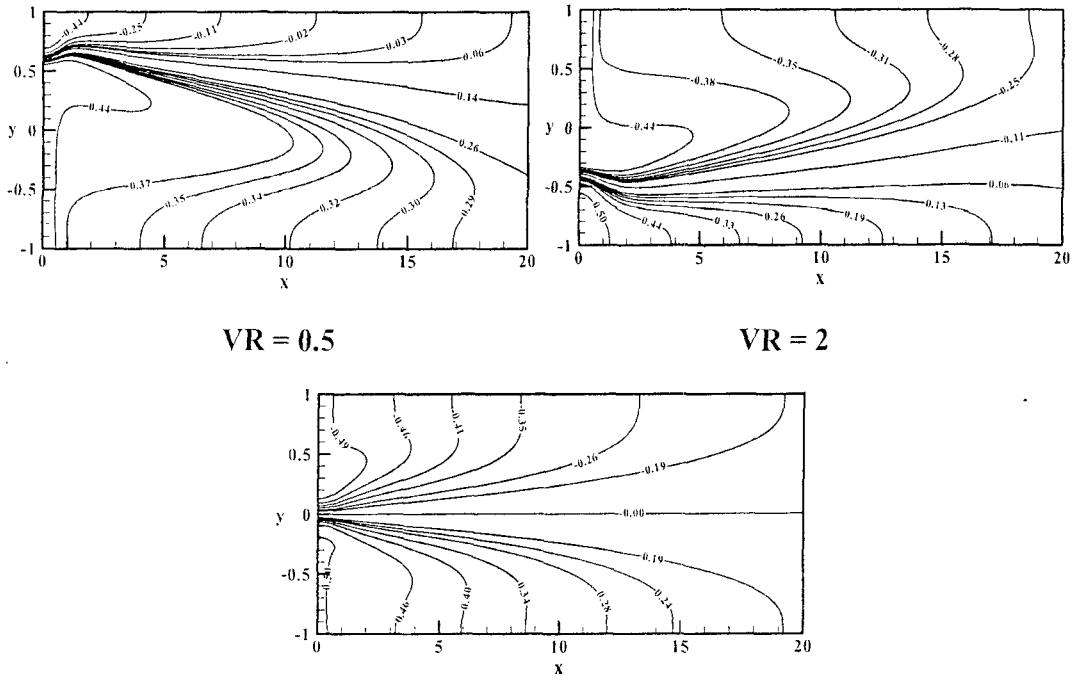

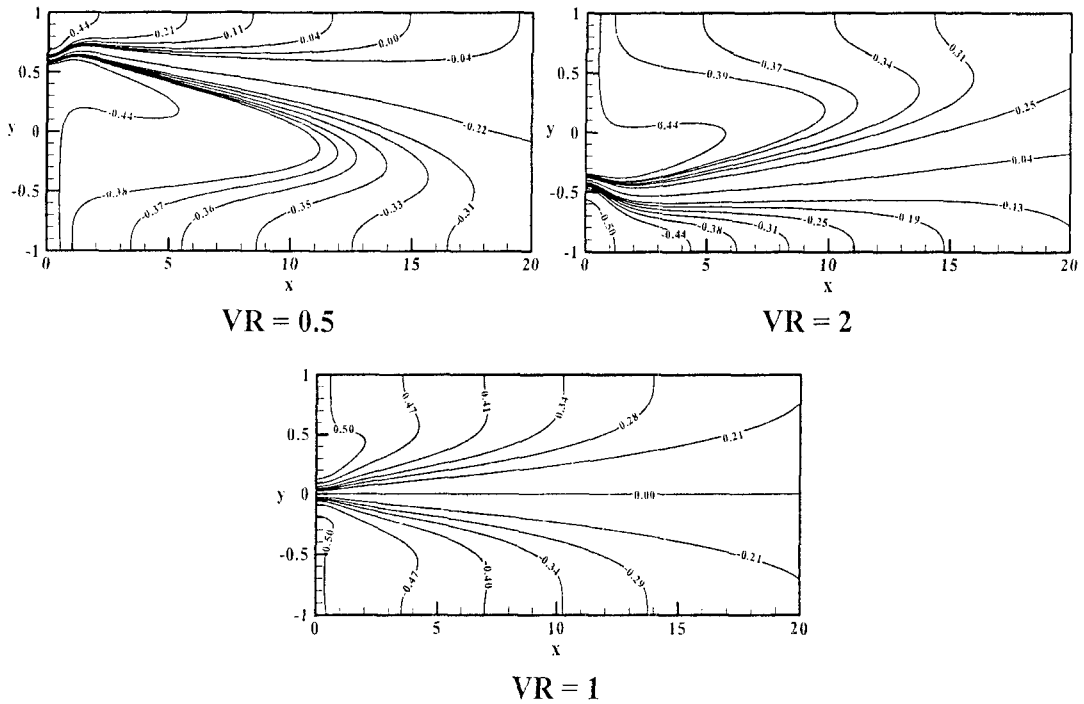

Fig 4.7: Steady state a) Isotherm patterns and b) Iso-concentration patterns at $Ri_T = 0.5$, $Ri_C = 1$ for VR = 0.5, VR = 2 and VR = 1 respectively

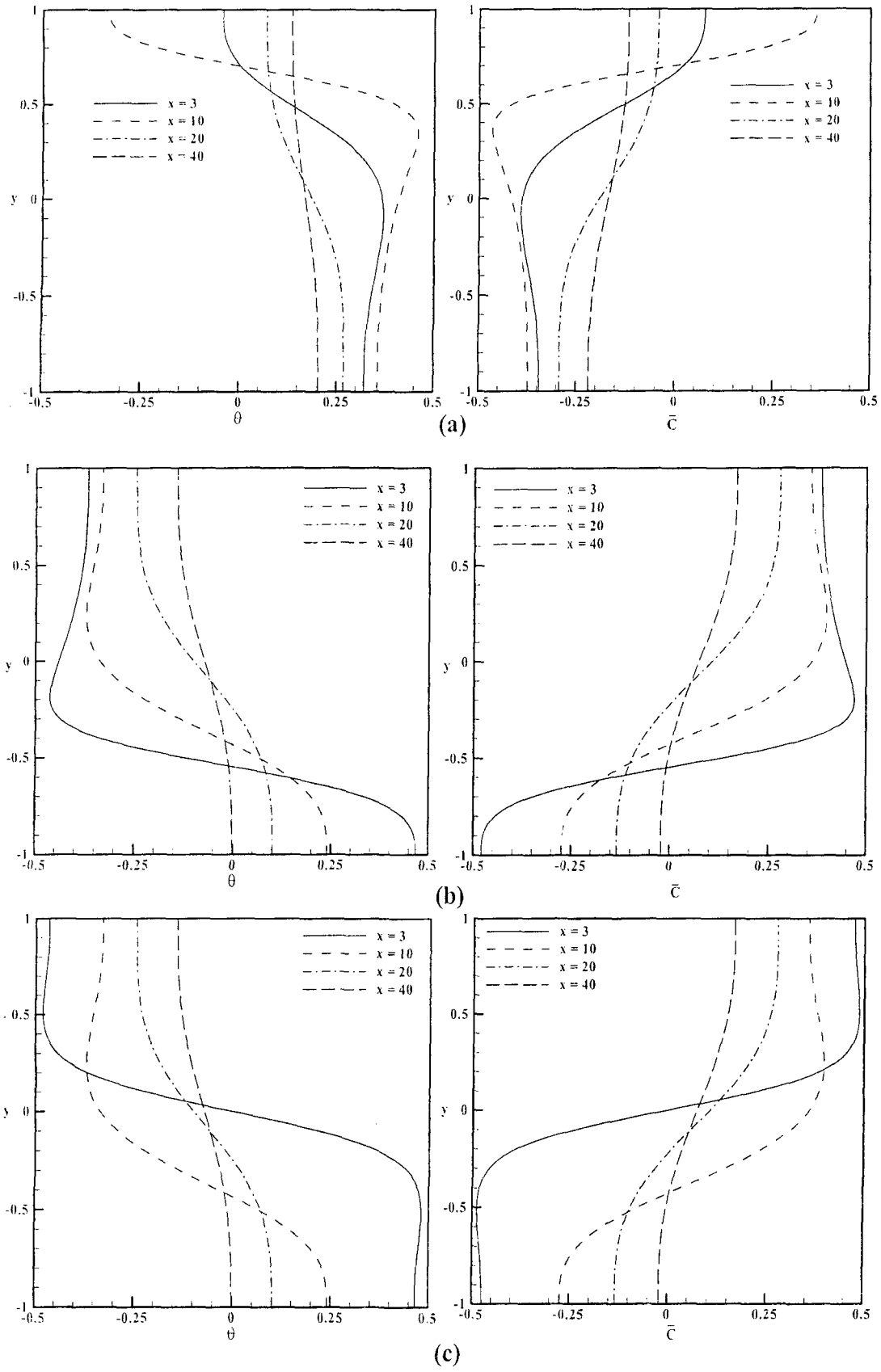

Fig. 4.8: Steady state temperature (left) and concentration (right) profiles respectively for a) VR = 0.5, b) VR = 2 and c) VR = 1 at $Ri_T = 0.5$, $Ri_C = 1$

indicates that mixing is essentially confined in a narrow region around the stagnation point, whether the velocity ratios are equal or different. As the mixing proceeds along the channel length, the profiles progressively flatten out. At x = 40, the profiles become nearly flat with temperature and concentration values very close to their mean (= 0) values. The anti-symmetry about y = 0 for VR =1 as reported earlier, is removed for unequal velocity ratio cases due to shift in impingement point on either side of y = 0. However, as the mixing proceeds along the channel length, the profiles become more and more anti-symmetric. Further, the temperature and concentration profiles at a given axial location are nearly mirror images of each other or anti-symmetric. Therefore, the combined buoyancy or (Ri_T + Ri_C) would play a dominant role in controlling the flow dynamics at unequal velocity ratios too.

Figures 4.9(a)-(b) depict the steady state upper and lower wall pressures at Ri_T = 1 and Ri_C = 0.5 at VR = 0.5, 1 and 2 respectively. It is evident form Figs. 4.9(a), (b) that wall-pressures for upper-wall are highest at VR = 0.5 whereas, for lower wall, the wall-pressures are highest at VR = 2. This is expected as per the velocity boundary condition, as the stagnation point zone (zone of higher pressure) shifts towards the wall associated

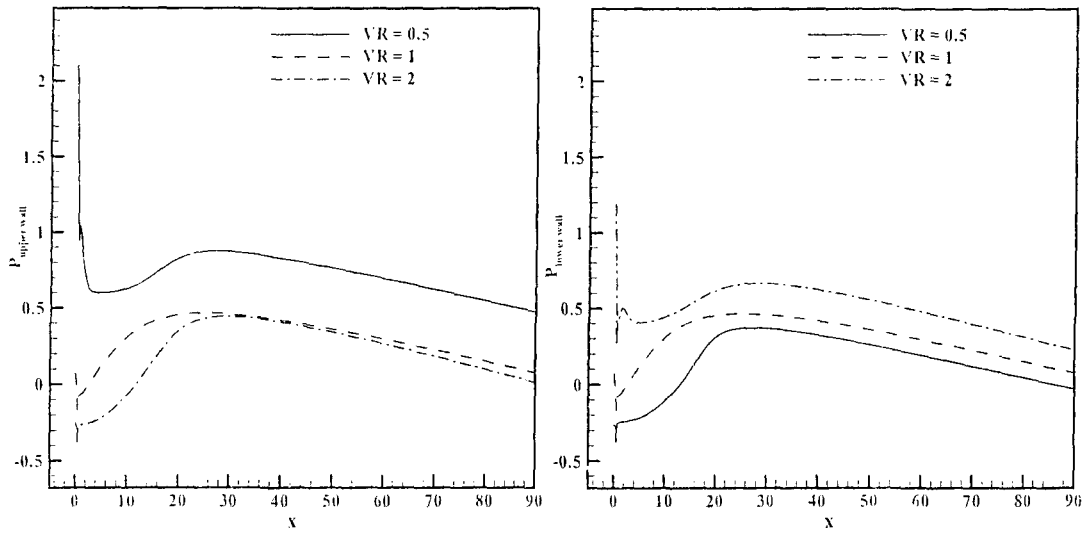

Fig. 4.9: Variation of steady state a) upper-wall and b) lower-wall pressures at Ri_T =1 and Ri_C = 0.5 at different VRs

with the lower velocity jet.

The observed size of the separated zones as represented by the re-attachment lengths for different values of VR in the steady flow regime are summarized in Table 4.1. It is observed that by doubling the velocity of the stream on one side, the separation on the opposite side can be reduced to insignificant proportion or eliminated completely. Further, for a two-fold increase in the velocity of one of the streams, the separation zone on the side of the higher velocity stream also exhibits a nearly two-fold increase in its length. It is also observed that, in contrast to the VR = 1 scenario, the unequal velocity scenarios exhibit a weak sensitivity to the individual values of the Richardson numbers for a given combined buoyancy level.

	VR= 0.5		**VR = 1**		**VR = 2**	
(Ri_T, Ri_C)	L_{ru}	L_{rl}	L_{ru}	L_{rl}	L_{ru}	L_{rl}
(0, 0)	6.82	10.33	9.07	2.80	10.31	6.27
(0, 0.5)	0	15.50	8.36	8.36	15.57	0.46
(0.5, 0)	0	14.96	8.49	8.49	15.32	0.46
(0, 1)	0	18.51	9.54	9.54	18.55	0.48
(1, 0)	0	17.82	9.80	9.80	18.25	0.47
(0.5, 0.5)	0	18.21	9.68	9.68	18.41	0.47
(0, 1.5)	0	20.85	10.89	10.89	21.07	0.48
(1.5, 0)	0	19.99	11.25	11.25	20.64	0.47
(0.5, 1)	0	20.57	10.61	10.61	20.94	0.48
(1, 0.5)	0	20.29	10.99	10.99	20.80	0.47
(1, 1)	0	22.32	-	-	23.06	0.46
(0.5, 1.5)	0	22.57	-	-	23.20	0.47
(1.5, 0.5)	0	22.08	-	-	22.92	0.46
(1, 1.5)	0	23.74	-	-	-	-
(1.5, 1)	0	23.85	-	-	-	-
(1.5, 1.5)	0	25.09	-	-	-	-

Table 4.1: Separation lengths of recirculation zones for VR = 0.5, 1 and 2 within the steady flow regime

4.2.3 Unsteady flow dynamics

A. *Spatio-temporal data analysis*

To examine the combined effect of unequal stream velocities and buoyancy forces on the flow dynamics, numerical simulations for cases of VR = 0.5, 1 and 2, are carried out at (Ri_T = 1, Ri_C = 1.5) and at (Ri_T = 1.5, Ri_C = 1). In both these cases, in the limit of large times, the flow develops an oscillatory instability and settles into a periodic state for VR = 1 and 2, where as for VR = 0.5 the flow is long time steady as reported earlier in §4.2.1.

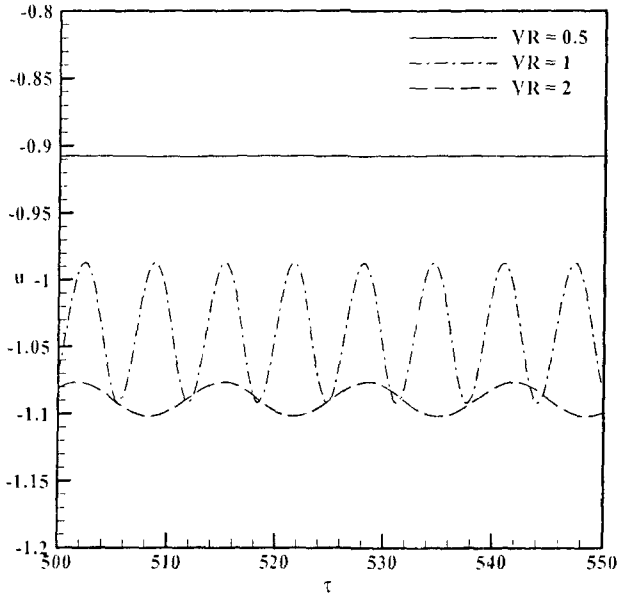

Fig. 4.10: Time history of u (-15.56, 0) at (Ri_T = 1, Ri_C = 1.5) for VR = 0.5, 2 and 1

The periodic nature of the flow for VR = 1 and 2 and steady nature of flow for VR = 0.5 are clearly depicted in Fig. 4.10 which shows the time history of u-velocity at (-15.56, 0) for the three cases of VR under investigation. The time history clearly shows that the oscillation frequency is decreased with increase in VR beyond unity.

The mean streamline patterns, isotherms and iso-concentration patterns at Ri_T = 1, Ri_C = 1.5 for both unsteady cases of VR = 2 and VR = 1 are shown in Figs. 4.11 (a)-(c) respectively. It is quite evident from Figures 4.11(a)-(c) that although both cases of VR considered here are unsteady and show oscillatory periodic nature, the mean flow of plots

are qualitatively different for the two cases considered. The spatial structure of mean flow as represented by plots of streamlines, isotherms and iso-concentration contours for VR = 2 is qualitatively similar to that of the steady flow structure at same velocity ratio, which is not the case for VR=1. For VR = 1 instability in the form of standing wave is already established using POD analysis in §3.3-B. As the mean flow structure for VR = 2 is different from that at VR = 1, it indicates that the nature of instability is somewhat different from that at VR = 1.

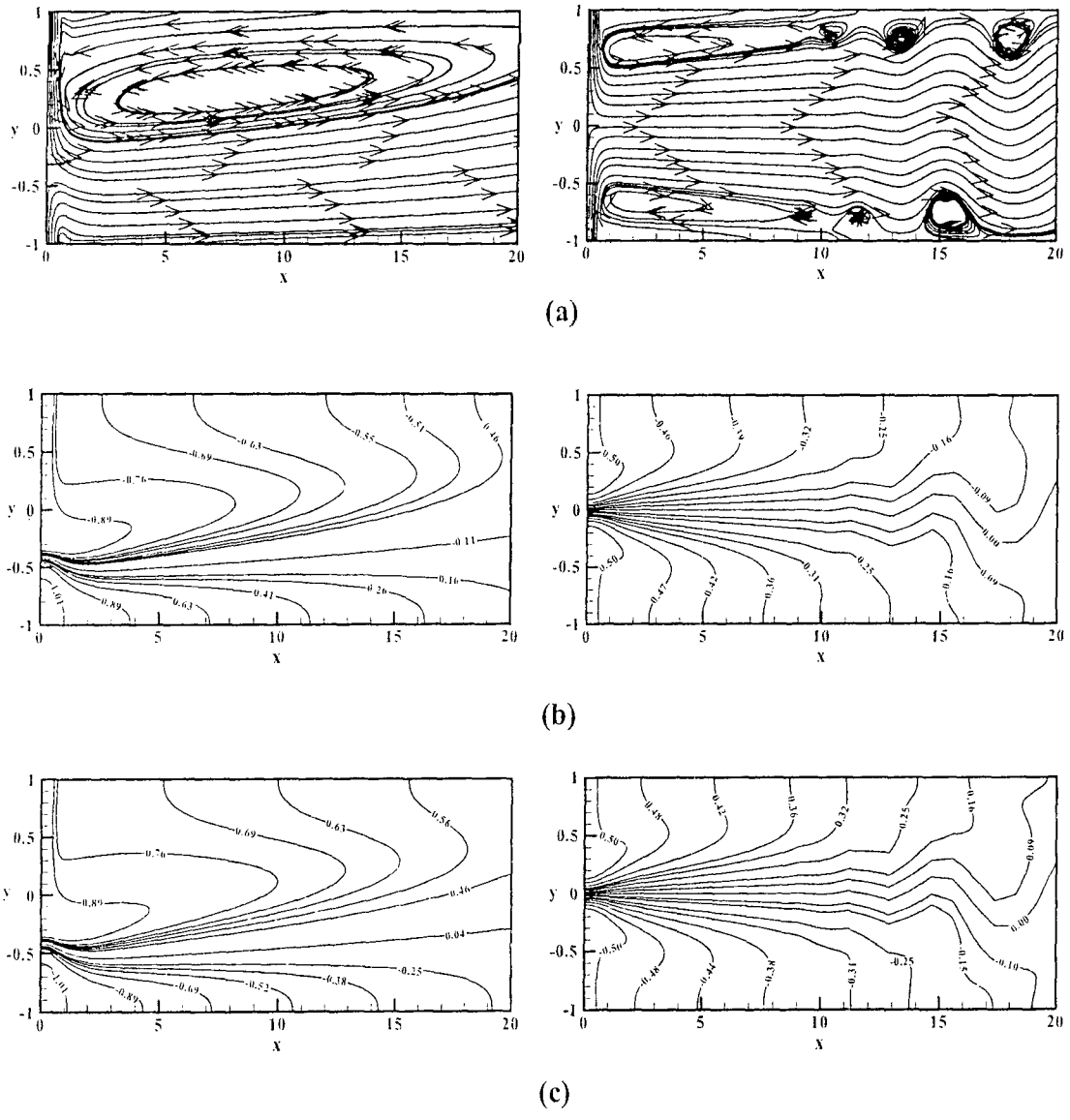

Fig. 4.11: Mean flow patterns as represented by a) streamlines, b) isotherms and c) iso-concentration for VR = 2 (left) and VR = 1 (right) respectively at Ri_T = 1 and Ri_C = 1.5

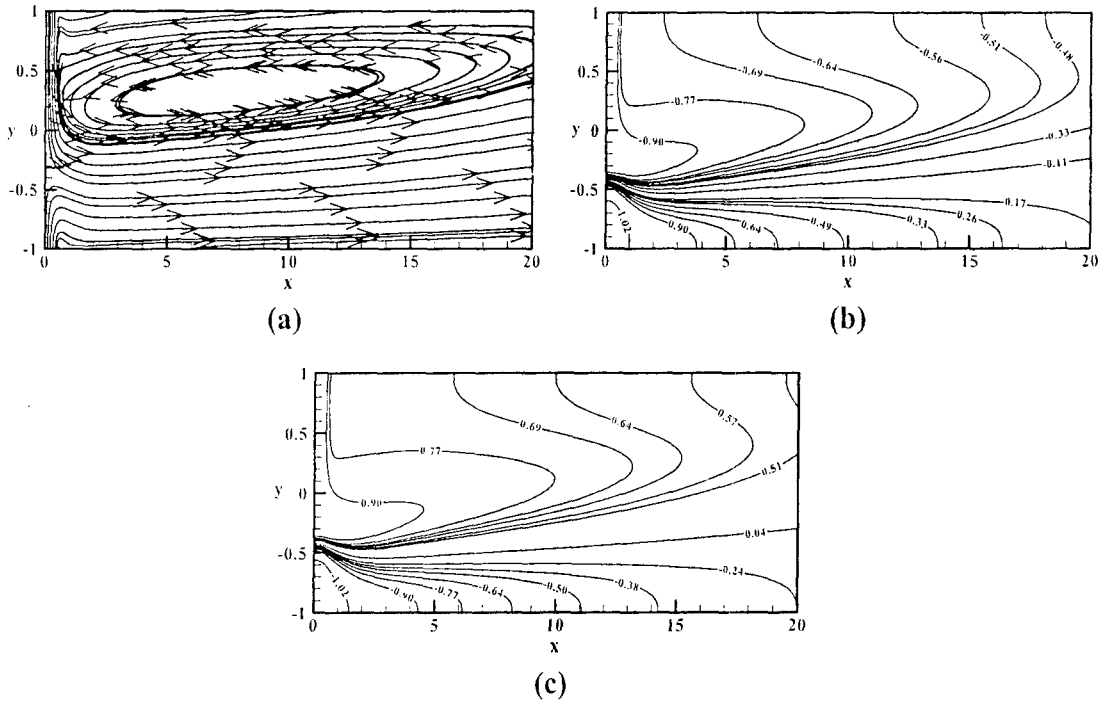

Fig. 4.12: Mean flow patterns for a) streamlines, b) isotherms and c) iso-concentration for VR = 2 at Ri_T = 1.5 and Ri_C = 1

In order to examine the sensitivity of the mean flow structure to the individual thermal and concentration Richardson numbers for VR = 2, the spatial structure of mean flow field for VR = 2 at Ri_T = 1.5, Ri_C = 1 is depicted in Figs. 4.12(a)-(c). On comparison with spatial structures at Ri_T = 1, Ri_C = 1.5 (Figs. 4.11 (a)-(c)), it is evident that there is no qualitative difference in the mean flow structure for unsteady cases as well.

The spatial structure of the periodic flow in the unsteady regime is captured through instantaneous streamline patterns over one cycle of oscillations as shown in Figs. 4.13(a)-(h), respectively at VR = 2 for (Ri_T = 1, Ri_C = 1.5). The instantaneous snapshots show sinuous streamlines beyond x > 15. At (Ri_T = 1, Ri_C = 1.5) for VR = 1 (refer Fig. 3.18), the streamlines become sinuous in character for x > 10 only. This indicates that the instability grows less rapidly in space for VR = 2.0 than for VR = 1.0. For x < 15, the streamlines appear to be steady in the flow, therefore the unstable perturbation or mode appears as a spatially growing mode characterizing a convective instability which is similar to the finding reported for VR = 1 at Ri_T = 1, Ri_C = 1.5 (refer §3.3.3). The time

history of u-velocity at (-0.90, 0) shown in Fig. 4.14(a). Fig. 4.14(a) clearly shows that the flow is locally steady.

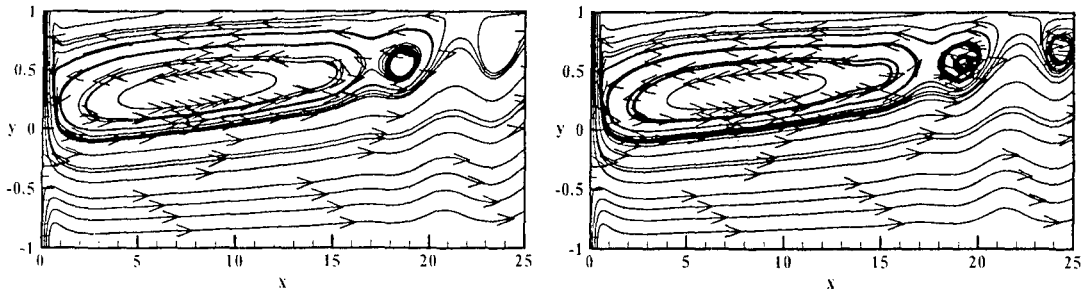

(a) $\tau = 3327.88$ (b) $\tau = 3329.57$

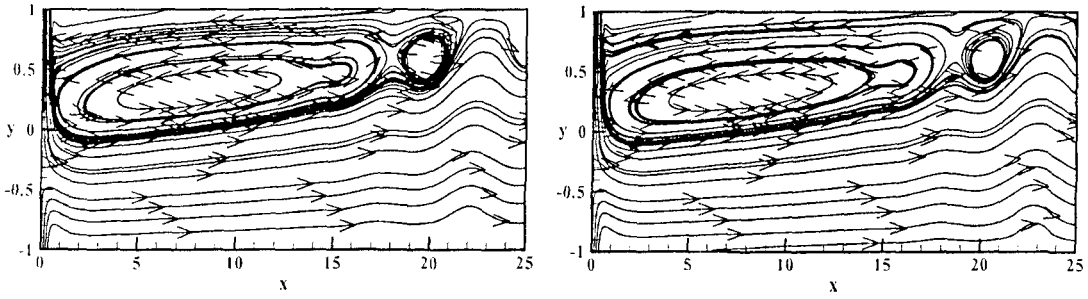

(c) $\tau = 3331.26$ (d) $\tau = 3332.95$

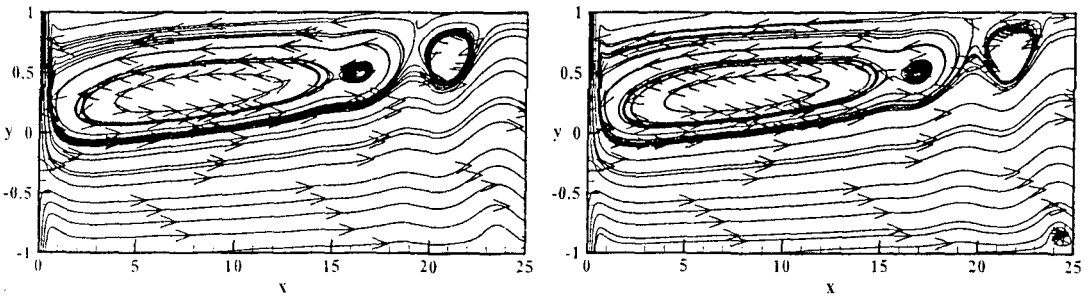

(e) $\tau = 3334.63$ (f) $\tau = 3336.32$

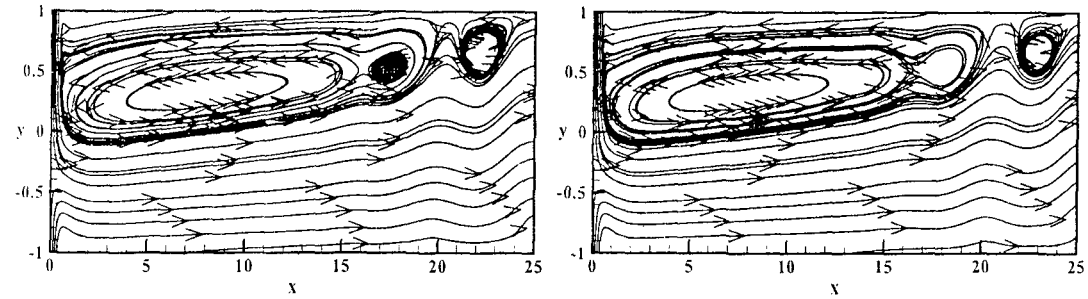

(g) $\tau = 3338.01$ (h) $\tau = 3339.70$

Fig. 4.13: Instantaneous streamline patterns over one temporal cycle for VR = 2 at $Ri_T = 1$, $Ri_C = 1.5$

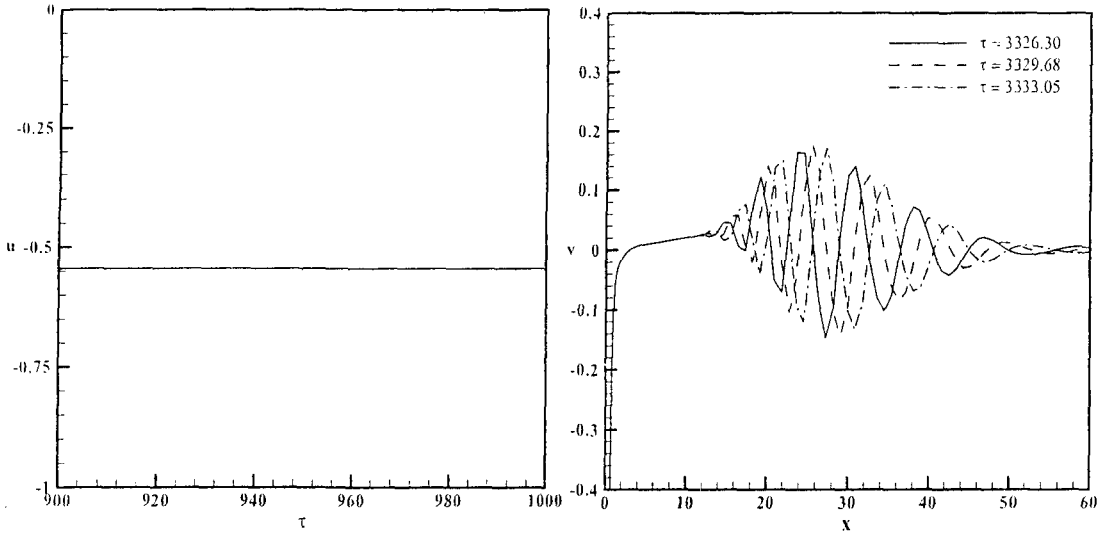

Fig. 4.14: a) Time history of u (+0.90, 0) and b) the instantaneous v-velocity along channel centerline at different instants of time at $Ri_T = 1$, $Ri_C = 1.5$

The oscillatory spatial growth of the unstable mode is captured in the instantaneous v-velocity profile along the channel centerline at different time instants over one temporal cycle as shown in Fig. 4.14(b). The profiles show that the perturbation grows rapidly beyond x = 15, reaches a maximum amplitude at around x = 25 and then decreases to very small values for x > 60.

The mean temperature, concentration and u-velocity profiles at four different axial locations, for both VR = 2 (left) and VR = 1 (right) at $Ri_T = 1$, $Ri_C = 1.5$, are shown in Figures 4.15(a)-(c) respectively. Temperature profiles for both VR = 2 and 1 are nearly mirror images of the corresponding concentration profiles. Therefore, it is expected that switching the values of the two Richardson numbers for a fixed combined buoyancy level should not have a significant effect on flow dynamics. This is similar to the findings reported in §4.2.2 for the steady flow regime.

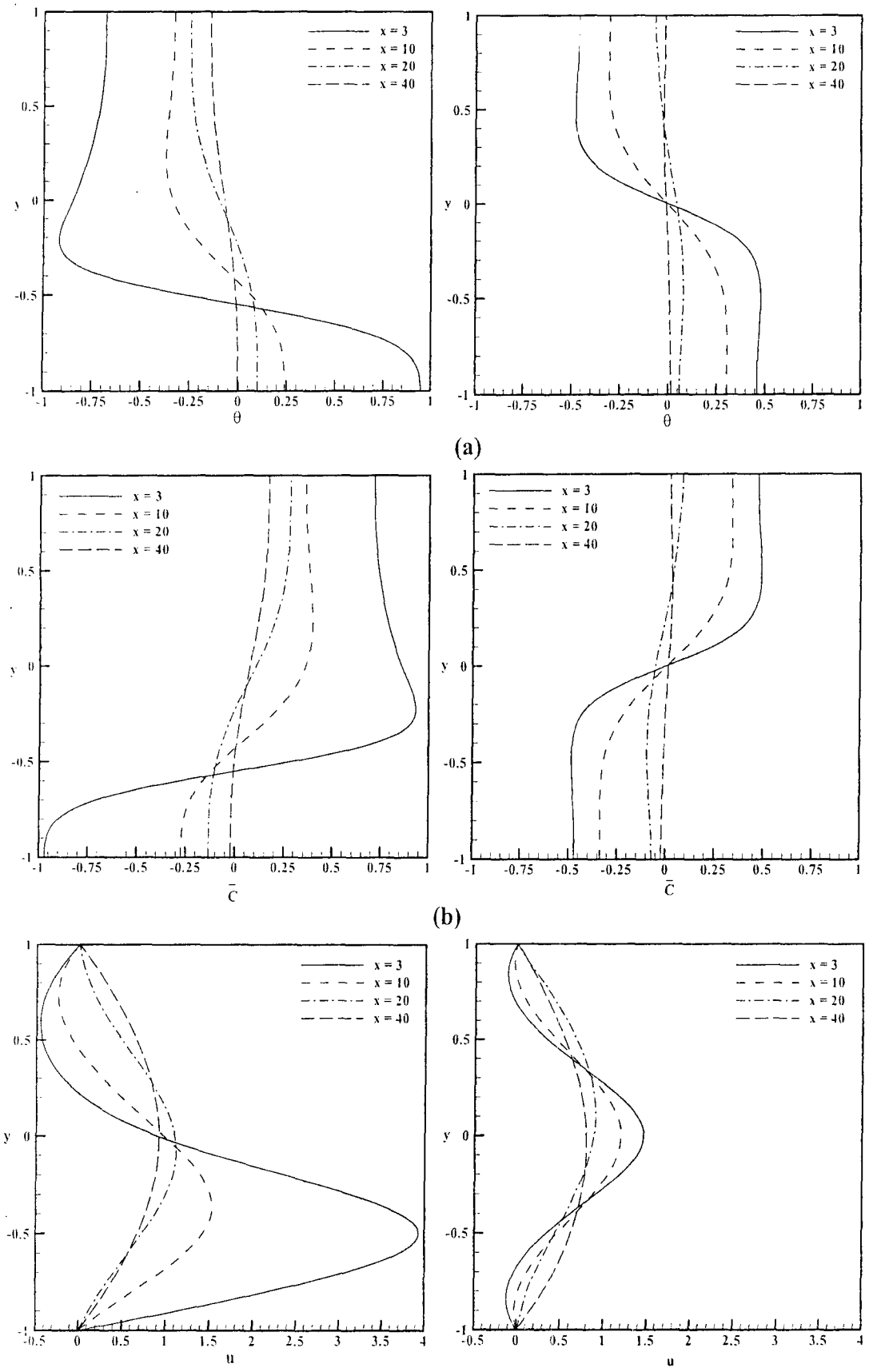

Fig. 4.15: Mean a) temperature, b) concentration and c) u-velocity profiles for VR = 2 (left) and VR = 1 (right) at $Ri_T = 1$, $Ri_C = 1.5$

Figures 4.16(a)-(b) compare the mean upper-wall and lower-wall pressures, respectively, for (Ri_T =1 and Ri_C = 1.5) at VR = 1 and 2. The trends in the mean wall pressure are similar to those in the steady flow regime.

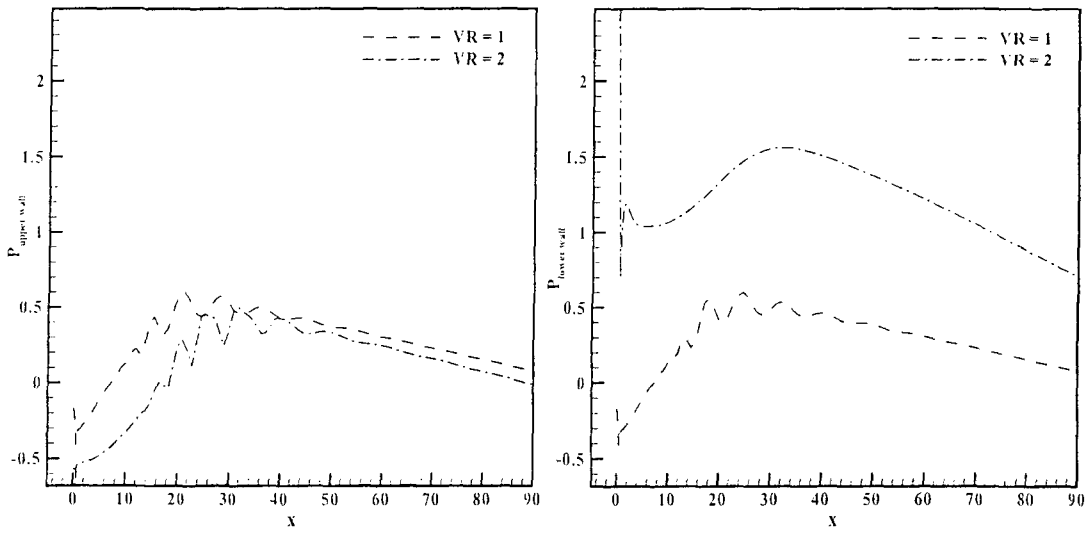

Fig. 4.16: Variation of mean a) upper-wall and b) lower-wall pressures at Ri_T =1 and Ri_C = 1.5 at VR = 1 and 2

The reattachment lengths associated with the top and bottom recirculating zones and the frequencies of the fluctuating velocity field for unsteady cases at VR = 1 and VR = 2 are summarized in Table 4.2. The blanks in the table indicate that the operating point does not lie in the unsteady regime for VR = 2 cases. The tabulated values clearly indicate that the reattachment lengths are only weakly affected by interchanging the values of the Richardson numbers for a fixed combined buoyancy level. Not much increase in the lengths of upper-right recirculating zones at VR = 1, is observed for finite buoyancy cases as compared to the forced flow, whereas, for VR = 2 more that two fold increase in upper-right recirculating zones length is reported. Interestingly, the flow frequency is nearly double at VR = 1 as compared to that recorded at VR = 2. This hints that the

structure of the unstable mode that leads to the transition from steady to unsteady at VR = 2 could be somewhat different than at VR = 1. This examined via POD analysis presented in the next section.

	VR=1			VR=2		
(Ri_T, Ri_C)	L_{ru}	L_{rl}	Frequency	L_{ru}	L_{rl}	Frequency
(0, 0)	9.07	2.80	0	10.31	6.27	0
(1, 1.5)	11.33	11.91	0.152	23.84	0.48	0.074
(1.5, 1)	10.82	10.23	0.153	24.11	0.47	0.074
(1.5, 1.5)	10.90	11.02	0.183	24.21	0.47	0.078

Table 4.2: Comparison of the salient features of the flow patterns in the unsteady flow regime at VR = 1 and 2

B. *POD Analysis*

POD analysis is carried out to further examine the structure of the unsteady flow field and to confirm the presence of travelling waves in the unsteady flow domain. Figure 4.17

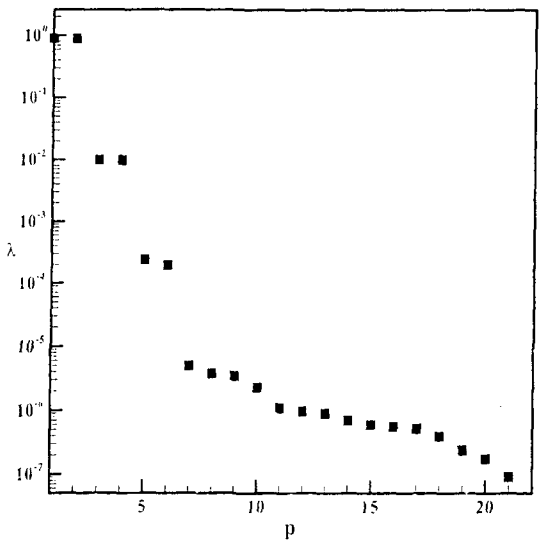

Fig. 4.17: The POD eigenspectrum obtained from the unsteady fluctuating field data for VR = 2 at Ri_T = 1.0, Ri_C = 1.5

shows the eigenspectrum obtained with a data ensemble of 32 snapshots over one temporal cycle of the flow VR = 2 at Ri_T = 1, Ri_C = 1.5. The presence of atleast two ((1, 2) and (3, 4)) degenerate pairs, having significant energy, in the spectrum clearly confirms the presence of travelling waves in the flow domain [70, 67, 71].

The temporal and spatial structure of the first three leading POD modes is shown in Fig. 4.18(a) and Fig. 4.18(b) respectively. The temporal structure of the POD modes is captured by the temporal coefficients $a^{(1)}(\tau)$, $a^{(2)}(\tau)$ and $a^{(3)}(\tau)$ while the spatial structure is captured by the associated eigenfunctions. Figure 4.18(b) depicts the spatial structure of the temperature eigenfunctions along the channel centerline for the three leading modes.

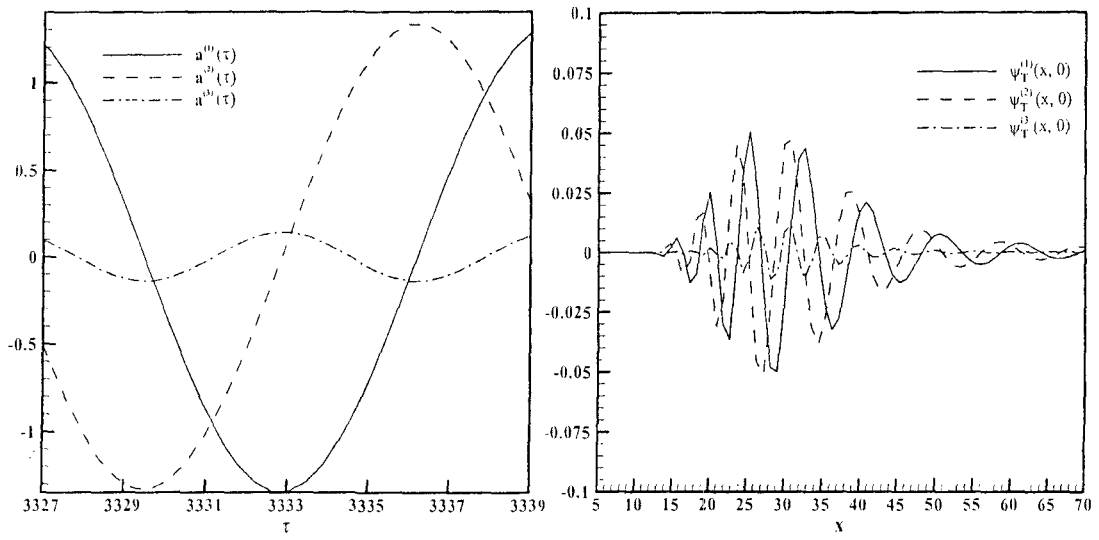

(a) (b)

Fig. 4.18: The (a) temporal and (b) spatial structure of the leading three POD modes for VR = 2 at (Ri_T = 1, Ri_C = 1.5)

Referring to Fig. 4.17, the eigenvalue spectra reveal that atleast four eigenvalues are degenerate, i.e. occur in pairs. The eigenvalues for modes (1, 2), and (3, 4) are some of the more energetic degenerate pairs. The degeneracy of the eigenspectrum is due to the spatio-temporal symmetries of the flow solution as reported in detail by Hasan and Sanghi [65].

To observe such symmetries, time histories of the temporal coefficients of a degenerate pair of modes ($a^{(q)}(\tau)$, $a^{(q+1)}(\tau)$) and the contributions of the individual modes of the selected degenerate pair to the flow field at an instant are compared. Figure 4.19(a), (b) compares the time histories of the coefficients for first and second degenerate pairs of modes. It is readily seen that the pair of coefficients $a^{(1)}(\tau)$ and $a^{(2)}(\tau)$ as well as $a^{(3)}(\tau)$ and $a^{(4)}(\tau)$ are almost identical except for a phase shift in time.

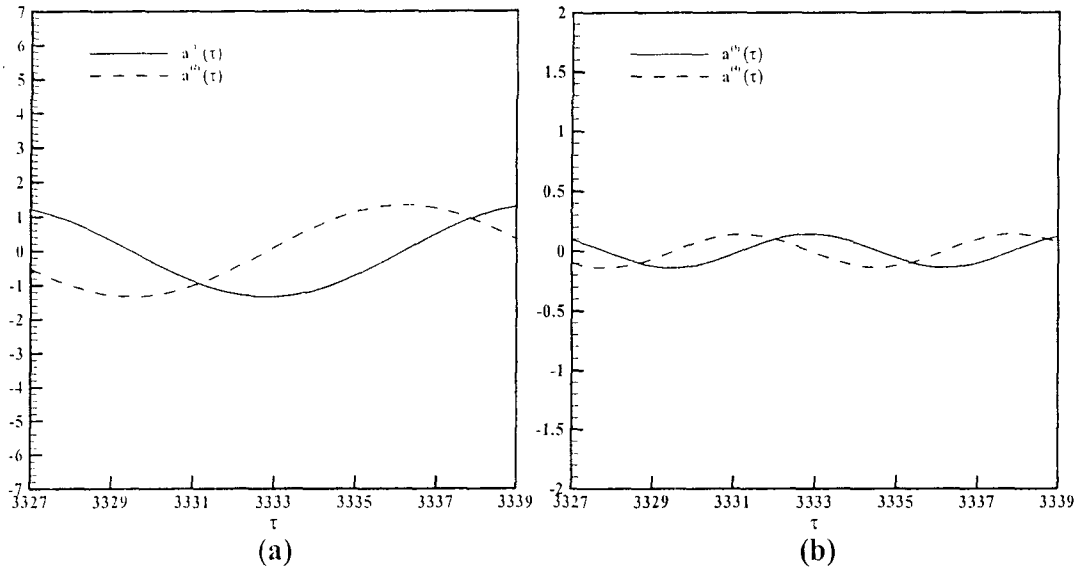

Fig. 4.19: The time evolution of temporal coefficients of degenerate pairs of modes for VR = 2 at Ri_T = 1, Ri_C = 1.5

Figure 4.20 shows the spatial structure of the individual contributions of POD modes having nearly equal eigenvalues to the temperature field at τ = 3326.30 at Ri_T = 1 and Ri_C = 1.5.

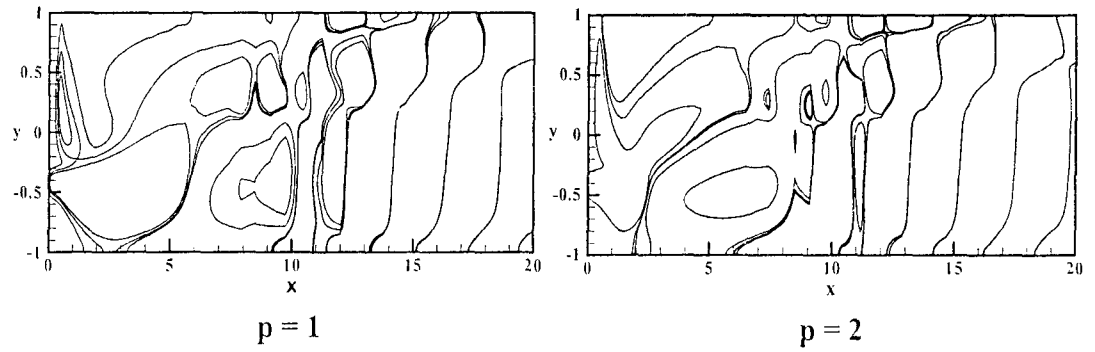

Fig. 4.20: The spatial structures of the contributions of pairs of POD modes having equal eigenvalues to the temperature field at τ = 3326.30 at Ri_T = 1 and Ri_C = 1.5

It is observed that the two thermal contour patterns are similar but shifted in the positive x-direction owing to the presence of travelling waves. Some distortion is expected due to non-linear convective interactions and diffusive effects.

The spatial shift in the x-direction of the structures of the degenerate pairs of eigenfunctions ($\psi_T^{(1)}$, $\psi_T^{(2)}$) and ($\psi_T^{(3)}$, $\psi_T^{(4)}$) are highlighted through plots shown in Figure 4.21(a)-(b). The spatial structures of $\psi_T^{(1)}$ and $\psi_T^{(2)}$ reveal translational symmetry in the x-direction. From Fig.4.19 and Fig. 4.21 it is evident that mode 1 leads mode 2. This clearly suggests that the degenerate pair (1, 2) represents a propagating structure or a travelling wave in the x-direction with the flow.

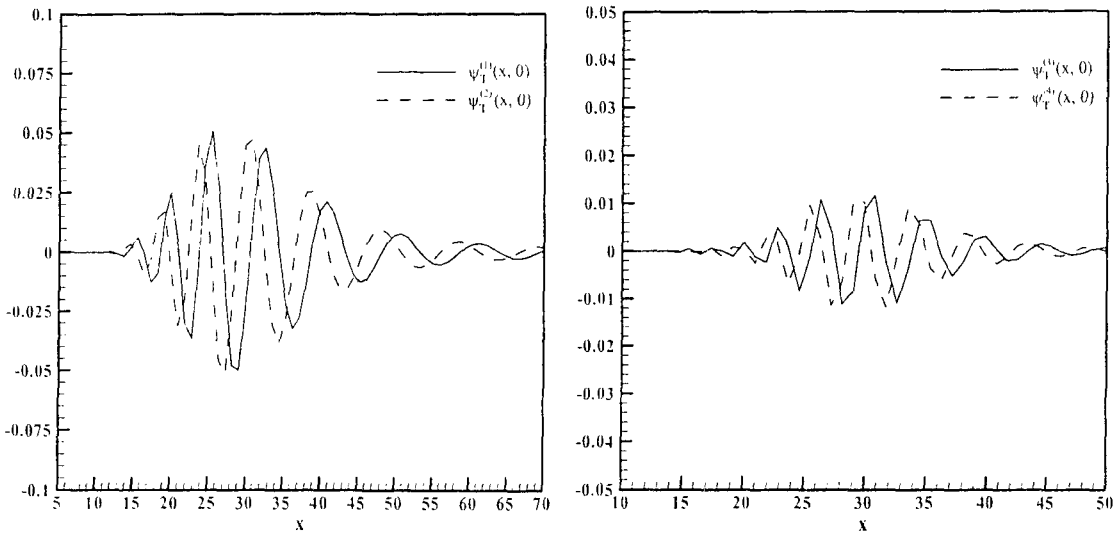

Fig. 4.21: Spatial structure degenerate of the temperature eigenfunctions a) ($\psi_T^{(1)}$, $\psi_T^{(2)}$) and (b) ($\psi_T^{(3)}$, $\psi_T^{(4)}$) in the x-direction along the channel centreline

Similar space-time symmetries are exhibited by other degenerate pairs for other two unsteady cases for VR = 2 ((Ri_T = 1.5, Ri_C = 1) and (Ri_T = 1.5, Ri_C = 1.5)).

For the case of a traveling wave, as pointed out by Aubry et al. [72] and demonstrated by Hasan and Sanghi [65], the space-time shifts in the POD eigenfunctions and the temporal coefficients for a given degenerate pair of modes can be exploited to determine the wave speed (phase speed of the wave). For a uniformly travelling one-dimensional

wave, the phase speed of the wave is given by the ratio of the spatial and the temporal shifts observed in the eigenfunctions and the temporal coefficients of the degenerate pair of modes. In the present context, it has been shown that wave is predominantly in x-direction. The major issue regarding the estimation of the wave speeds is the fact that the translational shifts in the temporal coefficients and the spatial eigenfunctions for a degenerate pair are not uniform in time and space respectively. Therefore, estimates of the average translational wave speed ($\bar{c}$), at a three different locations of y viz. y = -0.5, 0, 0.5, are made on the basis of the average translational shifts (both in space and time) in the structure of the degenerate pair of modes.

(Ri_T, Ri_C)	Degenerate pairs (q, q+1)	y location	Wave speed $\bar{c}$	Fluid velocity $\bar{\bar{u}}$	$\frac{\bar{c}}{\bar{\bar{u}}}$
(1, 1.5)	1, 2	0	0.589	1.484	0.397
		-0.5	0.494	1.112	0.444
		0.5	0.494	0.944	0.523
(1.5, 1)	1,2	0	0.532	1.505	0.353
		-0.5	0.470	1.129	0.416
		0.5	0.578	0.946	0.611
(1.5, 1.5)	1,2	0	0.490	0.732	0.669
		-0.5	0.463	0.552	0.839
		0.5	0.458	0.461	0.993

Table 4.3: Average phase speeds of the travelling waves (x-direction) at different y locations in the channel for different (Ri_T, Ri_C), combinations

Table 4.3 compares these wave speeds to the time-mean spatially averaged flow velocity in x-direction ($\bar{\bar{u}}$) at different y locations (y = -0.5, 0, 0.5) in order to obtain some insight into the wave properties. It is interesting to observe that the ratio $\frac{\bar{c}}{\bar{\bar{u}}}$ lies in the range 0.35–0.99.

4.2.4 Mixing Characteristics

In order to assess the impact of velocity ratio parameter on the thermal and physical

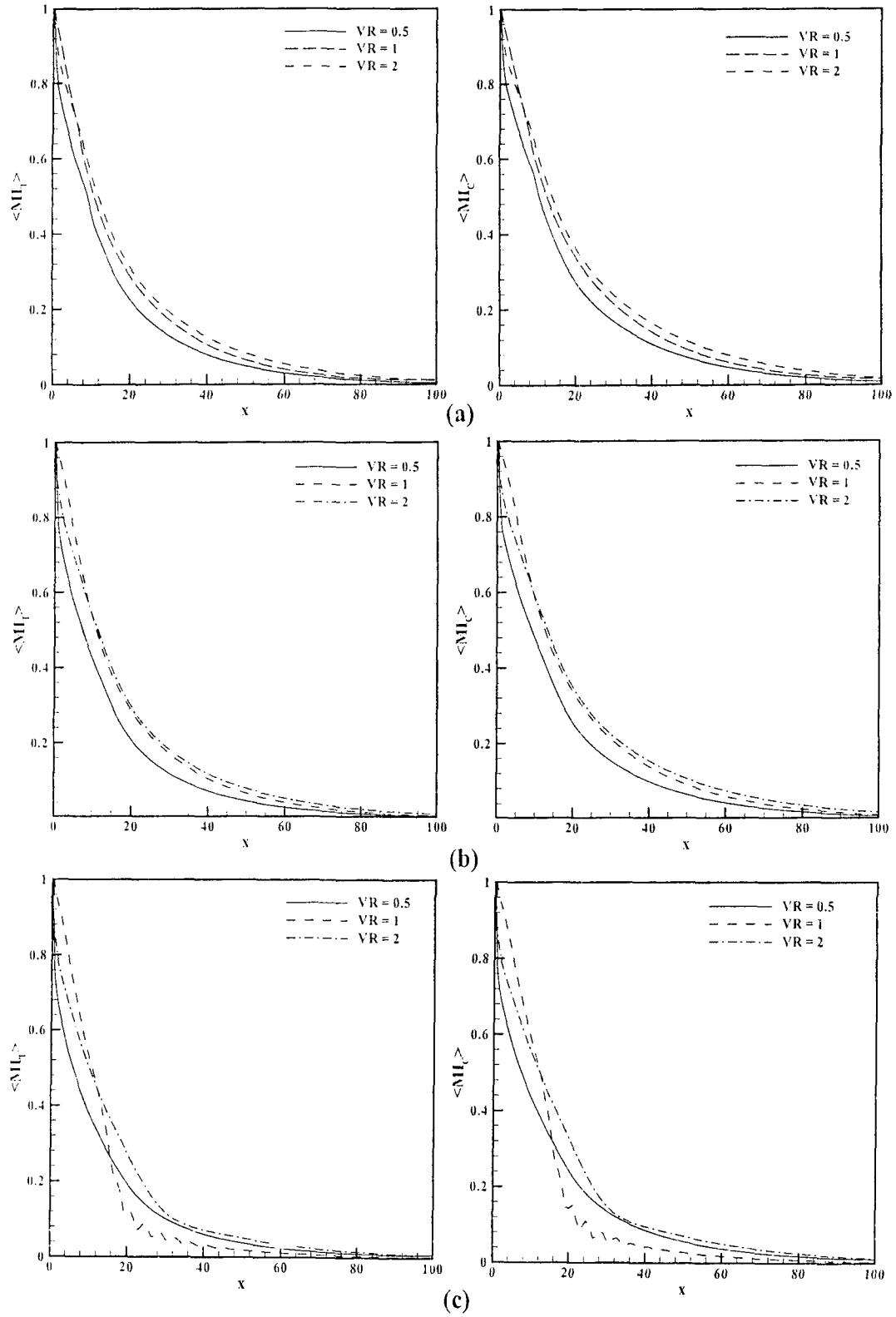

Fig. 4.22: Thermal (left) and physical (right) normalized mixing indices for a) (Ri_T = 0, Ri_C = 0), b) (Ri_T = 1, Ri_C = 0) and c) (Ri_T = 1, Ri_C = 1.5) at VR = 0.5, 1 and 2

mixing characteristics of the two jets, plots of temperature (left) and concentration (right) of normalized mixing indices for forced flow, (Ri_T = 1, Ri_C = 0) and (Ri_T = 1, Ri_C = 1.5) are shown in Figs. 4.22(a)-(c) respectively. For the forced flow (Fig. 4.22(a)), it is interesting to observe that the thermal and physical mixing is slightly better for VR = 0.5 than VR = 1 and VR = 2 cases. Maximum impact on both thermal and concentration mixing is of formation of standing waves in the channel for VR = 1. Mixing is also enhanced by the formation of travelling waves for VR = 2 but the effect is less as compared to that of standing wave (VR = 1). For the steady cases, where standing / travelling waves are absent, the mixing is adversely effected by the increase in the velocity ratio and from Fig. 4.22(b) it is evident that mixing is maximum at VR = 0.5 and minimum at VR = 2.

Table 4.4 and Table 4.5 summarizes the values of mixing lengths estimated as for the three different velocity ratios in unsteady and steady flow regimes respectively. The forced flow case has been included for comparison purposes. It is evident from Table 4.5 that for forced flow and steady regime cases, shortest mixing lengths, for any combination

	VR = 1		VR = 2	
(Ri_T, Ri_C)	L_{mT}	L_{mC}	L_{mT}	L_{mC}
(0, 0)	41.26	48.10	45.57	53.60
(0.5, 1.5)	23.18	26.30	-	-
(1.5, 0.5)	25.92	29.67	-	-
(1, 1)	25.03	26.11	-	-
(1, 1.5)	21.89	22.42	32.37	38.65
(1.5, 1)	20.81	23.92	34.38	41.72
(1.5, 1.5)	13.20	13.39	30.11	34.34

Table 4.4: Thermal and physical mixing lengths for different combinations of Ri_T and Ri_C for unsteady flow regime at VR = 0.5, 1 and 2

of Ri_T and Ri_C, are obtained at VR = 0.5. Also the effect of buoyancy on the mixing lengths for all steady regime cases at different VR is insignificant. This is a direct

consequence of the fact that in the steady flow regime, for the cases investigated, the flow features do not exhibit a strong sensitivity to the buoyancy effects (see Table 4.1).

For unsteady flow cases that involve the formation of standing waves (VR = 1 cases only), the drop in the mixing lengths is more in comparison to the unsteady cases of VR = 2, where travelling waves are present. Thus it is concluded that standing waves yield higher mixing rates than the travelling waves in the context of the problem investigated.

	VR = 0.5		VR = 1		VR = 2	
(Ri_T, Ri_C)	L_{mT}	L_{mC}	L_{mT}	L_{mC}	L_{mT}	L_{mC}
(0, 0)	35.36	42.18	41.26	48.10	45.57	53.60
(0, 0.5)	34.29	41.10	41.34	48.27	44.75	52.85
(0.5, 0)	34.24	41.03	41.24	48.14	44.67	52.75
(0, 1)	33.19	39.94	41.04	48.04	43.94	52.10
(1, 0)	33.09	39.82	40.81	47.80	43.75	51.87
(0.5, 0.5)	33.14	39.88	40.92	47.92	43.85	51.99
(0, 1.5)	32.18	38.84	40.71	47.80	43.15	51.35
(1.5, 0)	32.03	38.66	40.37	47.41	42.84	50.99
(0.5, 1)	32.13	38.78	41.21	48.42	43.05	51.23
(1, 0.5)	32.07	38.72	41.26	48.10	42.95	51.11
(1, 1)	31.14	37.67	-	-	42.13	50.31
(0.5, 1.5)	31.21	37.73	-	-	42.25	50.44
(1.5, 0.5)	31.10	37.61	-	-	42.02	50.18
(1. 1.5)	30.32	36.67	-	-	-	-
(1.5, 1)	30.26	36.60	-	-	-	-
(1.5, 1.5)	29.52	35.65	-	-	-	-

Table 4.5: Thermal and physical mixing lengths for different combinations of Ri_T and Ri_C for steady flow regime at VR = 0.5, 1 and 2

This can be explained by closely examining the instantaneous flow patterns for VR = 1 and 2 (ref. Fig 3.18(a)-(h) and Fig. 4.13(a)-(h) respectively). Figure 3.18(a)-(h) shows that for VR =1, the mechanical mixing / churning, as represented by sinuous streamlines, starts at x = 10 where as for VR = 2 (refer Fig. 4.13(a)-(h)), the sinuous streamlines are

not seen before x = 15. Further the mixing / churning phenomenon is more rigorous at VR = 1 as compared to that at VR = 2 which is qualitatively evident from the instantaneous streamline plots for both cases. As reported in §3.3.4, about 40 % reduction in mixing length is observed when (Ri_T + Ri_C) increases from 2 to 3 for VR = 1, whereas, only 25% reduction is reported for same increase in (Ri_T + Ri_C) for VR = 2.

Figures 4.23(a), (b) and 4.24(a), (b) present graphically the trends in normalized

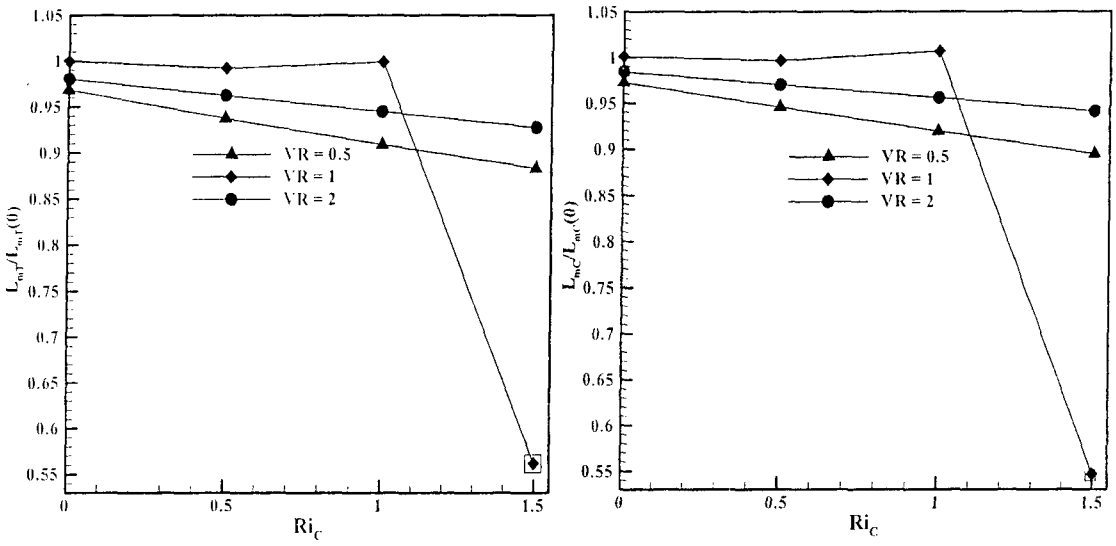

Fig. 4.23: a) Temperature and b) concentration normalized mixing lengths at Ri_T = 0.5 for different VRs

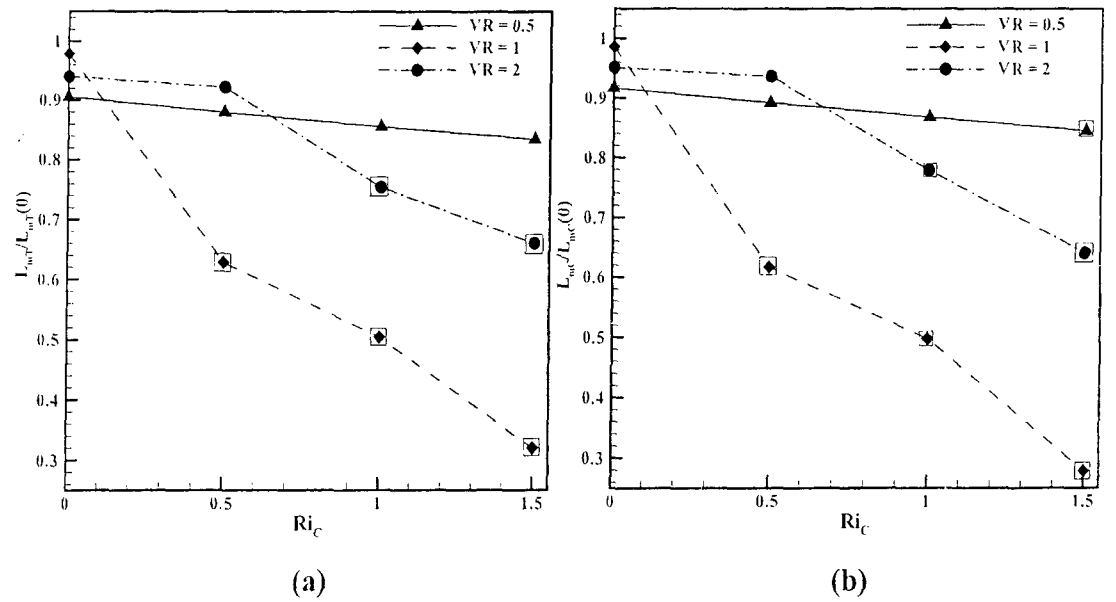

Fig. 4.24: a) Temperature and b) concentration normalized mixing lengths at Ri_T = 1.5 for different VRs

thermal and concentration mixing lengths, for different Ri_C (within parametric domain of present study) at $Ri_T = 0.5$ and $Ri_T = 1.5$ respectively. The unsteady cases are identified by enclosing the corresponding points in squares. The trend with regards to mixing lengths described in Tables 4.4 and 4.5 are evident in these plots.

Table 4.6 and Table 4.7 presents the temperature and concentration buoyancy mixing effectiveness values for both steady and unsteady flow cases at VR = 0.5, 1 and 2

	VR = 0.5		**VR = 1**		**VR = 2**	
(Ri_T, Ri_C)	e_{mT} (%)	e_{mC} (%)	e_{mT} (%)	e_{mC} (%)	e_{mT} (%)	e_{mC} (%)
(0, 0.5)	3.76	3.49	4.85	1.88	2.47	2.17
(0.5, 0)	4.04	3.77	5.37	2.37	2.87	2.5
(0, 1)	6.85	6.47	5.15	1.99	4.54	3.98
(1, 0)	7.64	7.16	6.22	3.00	5.44	4.79
(0.5, 0.5)	7.25	6.82	5.69	2.49	4.99	4.39
(0, 1.5)	8.70	8.68	5.55	2.18	6.43	5.65
(1.5, 0)	10.1	9.86	7.18	3.73	7.84	6.94
(0.5, 1)	9.16	9.07	2.87	3.68	6.91	6.08
(1, 0.5)	9.65	9.46	3.55	2.80	7.38	6.51
(0.5, 1.5)	10.4	10.7	-	-	8.82	7.81
(1.5, 0.5)	13	12.3	-	-	9.78	8.70
(1, 1)	12.1	11.4	-	-	9.31	8.26
(1, 1.5)	10.4	12.7	-	-	-	-
(1.5, 1)	14.5	12.8	-	-	-	-
(1.5, 1.5)	12.9	17	-	-	-	-

Table 4.6: Thermal and physical buoyancy mixing effectiveness for different combinations of Ri_T and Ri_C in the steady flow regime at VR = 0.5, 1 and 2

respectively. As already explained, buoyancy does not effect mixing in the steady flow regime significantly but greatly effects in the unsteady regime where standing / travelling

waves are present. The values of both thermal and concentration mixing effectiveness, presented in Tables 4.6, 4.7 are indicative of the above said fact. Maximum buoyancy mixing effectiveness of nearly 82 % is obtained for VR = 1 at Ri_T = 1.5, Ri_C = 1.5 where standing waves are found to exist. For same values of (Ri_T, Ri_C) at VR = 2, the corresponding value of buoyancy mixing effectiveness is nearly 37% much lower than that for the equal velocity case.

	VR = 1		VR = 2	
(Ri_T, Ri_C)	e_{mT} (%)	e_{mC} (%)	e_{mT} (%)	e_{mC} (%)
(0.5, 1.5)	50.55	49.01	-	-
(1.5, 0.5)	44.03	42.11	-	-
(1, 1)	49	48	-	-
(1, 1.5)	59.81	58.53	30.6	29.4
(1.5, 1)	58	57	26.3	24.9
(1.5, 1.5)	82.02	82.01	37.3	36

Table 4.7: Thermal and physical buoyancy mixing effectiveness for different combinations of Ri_T and Ri_C in the unsteady flow regime at VR = 1 and 2

4.3 Summary

For the forced flow (Ri_T = 0, Ri_C = 0) case, the instability which caused the flow to change from one steady symmetric state to another steady unsymmetric state at VR = 1.0 is suppressed for unequal velocity ratio cases (VR ≠ 1).

Within the range of Ri_T and Ri_C considered, steady and unsteady flow regimes are obtained for VR = 1 and 2, whereas only steady flow regime is obtained for VR = 0.5. On the basis of Landau theory, the nature of bifurcation encountered at both VR = 1 and 2 is established as a *supercritical Hopf bifurcation*. A complete regime map, within the parametric space of the present study, is obtained by plotting the neutral curves for

different values of VR. A curve fit relation representing the neutral curve at VR = 2 is obtained as,

$$Ri_C = A + B \times Ri_T + C \times Ri_T^2 + D \times Ri_T^3$$

where, A = 2.360, B = -1.214, C = 0.2102, D = -0.0266.

The flow structure in the steady as well as the unsteady flow regimes for different values of VR is not affected significantly by interchanging the values of the two Richardson numbers for a fixed combined buoyancy level. It is strongly influenced by *the combined value of* (Ri_T + Ri_C). *The reattachment lengths of top and bottom* recirculating zones are nearly same for equal velocity jets while for unequal velocity cases the recirculating zone on the lower velocity side is either eliminated or is very small. As per earlier observations, the net buoyancy aids the fluid inertia for all cases of VR (= 0.5, 1, 2); thereby causing an increase in the lengths of the recirculation zones with increase in the net buoyancy level.

The plots of temperature and concentration profiles at several axial locations reveal that both thermal and concentration gradients are observed in a narrow region on either side of the stagnation zone. This is indicative of the fact that mixing is higher in a narrow region around the stagnation zone for all VR cases considered in the present study.

The instantaneous v-velocity profile along the channel centerline at different time instants over one temporal cycle for VR = 2, shows oscillatory spatial growth of the unstable mode with the perturbation growing rapidly between x = 15 and x = 60. This type of structure of the unstable mode suggests the formation of waves in the flow domain for x > 15, which is similar to VR = 1 case where standing wave is the cause of unsteadiness.

In order to further examine the structure of the unsteady flow field and to confirm the character or nature of the waves in the flow domain for VR = 2, a Proper orthogonal

decomposition (POD) analysis is carried out. The presence of degenerate pairs in the eigenspectrum obtained with a data ensemble of 32 snapshots over one temporal cycle of the flow clearly confirms the presence of *travelling* waves in the flow domain. At VR = 2, the waves predominantly propagate in positive x-direction. The space–time symmetry of the degenerate pair of modes is utilized to estimate the average translational wave speeds for these cases. These travelling waves are always slower than the average fluid velocity at all locations considered with respect to the channel centerline.

For forced flow and steady flow regime cases, VR = 0.5 represents the best mixing system, with regards to both thermal and physical mixing, as indicated by normalized mixing index plots and mixing lengths. The thermal and physical mixing goes on decreasing with increase in velocity ratio for forced flow and in steady flow regime. For the unsteady periodic flow with standing waves as reported for VR = 1, the mixing process is significantly enhanced with the mixing length for $Ri_T + Ri_C = 3$ reducing by almost 70% than the corresponding forced flow values. This is attributed to the formation of standing waves leading to a sinuous flow pattern with the fluid particles following a wavy path. The effect of buoyancy for unsteady cases, where travelling waves are observed (VR = 2), are less as compared to unsteady cases where standing wave is present (VR = 1).

Presented in the next chapter are salient conclusions drawn from the present study with the parametric domain chosen. Scope for extension of present problem and similar studies are also reported.

Chapter 5

Conclusions and Recommendations

The problem of interaction of non-isothermal, opposed jets / streams of different fluids in a 2D adiabatic channel has been formulated by considering the fluid as a binary mixture. Both thermal and intrinsic buoyancy has been considered through the Boussinesq approximation. As the focus of the present study is to investigate the effects of thermal and intrinsic buoyancy, the effect of variation of thermal and concentration Richardson numbers (Ri_T and Ri_C) and velocity ratio (VR) of the two interacting jets / streams on the flow dynamics and thermal and physical mixing of two jets is examined.

The flow system under consideration can be regarded as a mixing device, as both thermal and physical mixing of two impinging jets / streams takes place. Therefore one of the objectives of the present study is to quantitatively describe the mixing phenomena and also to utilize different scalar measures of mixing, such as Mixing Index (MI), Mixing Length (L_M) and Buoyancy Mixing Effectiveness (e_M), the examine the effect of Ri_T, Ri_C and VR on thermal and physical mixing.

In order to obtain physically realizable solutions, the values of Re, Pr and Sc is fixed at 200, 0.7 and 0.8 respectively. The half-length of the channel (ℓ) is taken as 100 so that the effect of exit boundary is not felt on the flow solutions. The non-dimensional height (h) is fixed at 2. The range of the two Richardson numbers namely, Ri_T and Ri_C, is chosen to vary between 0 and 1.5 which lies in mixed convection regime. To examine the effect of difference of flow rate and momentum of the two jets, three different cases of velocity ratios, VR, are considered, typically, 0.5, 1 and 2.

Essentially, two different aspects of the problem have been investigated. These are,

a) Spatio-temporal flow dynamics, and b) the mixing characteristics. The changes in the flow structure, both in the spatial and the temporal domains, as the different parameters are varied, have been studied through two distinct methods of analysis. In the first approach, the computational data obtained from the numerical simulations is utilized to directly examine the spatio-temporal structure of the flow, by generating plots of streamlines, isotherms, iso-concentration patterns, profiles of temperature, concentration and velocity at different axial locations, wall-pressures and time histories of unsteady flows. In the second approach, proper orthogonal decomposition (POD) has been employed specifically to examine the structure of unsteady flows, in order to identify the dominant structures. The mixing characteristics are examined by plotting and / or tabulating both thermal and concentration Mixing Indices, Mixing Lengths and Buoyancy Mixing Effectiveness.

The present chapter is organized in three sections. Section 5.1 presents the main conclusions drawn from the study of the spatio-temporal flow dynamics which includes analysis of raw computational data and POD post-processing to study the dominant structures associated with the unsteady flows. The conclusions regarding mixing characteristics are presented in §5.2. Finally, suggestions for further studies are provided in §5.3.

5.1 Spatio-temporal flow dynamics

The main conclusions drawn from the present study are enumerated as follows:

1) The instability leading to a transition from a symmetric steady state to an asymmetric steady state for the forced flow at VR = 1, is *suppressed* by buoyancy and when the velocities of the two jets are different.

2) Within the parametric range of the present study two different flow regimes are obtained: (i) long term *steady flow* regime and (ii) the *unsteady flow* regime having *oscillatory* behavior with vortex-shedding.

3) The transition from steady to the unsteady flow takes place via a *supercritical Hopf bifurcation.*

4) A complete regime map, within the parametric space of (Ri_C - Ri_T), is obtained by plotting the neutral curves for different values of VR. The regime map clearly identifies the steady and the unsteady flow regimes for all cases of VR within the parametric range of thermal and concentration Richardson numbers considered.

5) The neutral curves separating the steady and the unsteady flow regimes can be represented in the form of cubic polynomial curve fit relation between critical concentration Richardson number and thermal Richardson number for different velocity ratios. The neutral curves can be expressed as,

$$\left(Ri_C\right)_{crit} = A + B \times Ri_T + C \times Ri_T^2 + D \times Ri_T^3$$

The various constants for different VR values are summarized as,

VR = 1: A = 1.900, B = -1.827, C = 0.8123, D = -0.1868

VR = 2: A = 2.360, B = -1.214, C = 0.2102, D = -0.0266

6) At VR = 0.5, for all combinations of Ri_T and Ri_C considered, the flow is long term steady.

7) It is observed that the transition from steady to unsteady flow regime is caused by a spatially growing unstable perturbation or mode that grows along the flow direction only and does not affect the upstream flow. This shows that the nature of instability associated with unsteady flows is of *convective type.*

8) For the range of parameters considered, the flows (steady as well as unsteady) always exhibit a symmetry about the mid-plane x = 0. This can be attributed to

symmetry of boundary conditions and the absence of any symmetry breaking, oscillating or flapping jets / streams instabilities for the chosen set of parameters.

9) In the context of the present problem, the physical action of the two buoyancy forces is to accelerate the two fluid streams as the direction of the net buoyancy force aids the fluid inertia. This is directly inferred from the observed trends in lengths of recirculation zones on the top and bottom walls.

10) In the steady flow regime, for all velocity ratio cases, the thermal and concentration fields possess an interesting *reflectional symmetry* property (approximately) with respect to each other. It is shown that this makes the flow dynamics weakly sensitive to the individual values of Ri_T and Ri_C for a given combined buoyancy level. Instead, the dynamics is strongly influenced (approximately) by the net buoyancy ($Ri_T + Ri_C$). This character can be attributed to the boundary conditions as well as the choice of the parameters Pr and Sc (Le ~ 1.0).

11) The reattachment length of the recirculating zone on the lower velocity side is either eliminated or is very small for unequal velocity ratio cases.

12) Owing to the relatively high thermal and concentration gradients on either side of the stagnation point, the mixing rates are high in a narrow region around the stagnation zone for all VR cases considered in the present study.

13) Due to the acceleration imparted to the two jets by the buoyancy forces, the wall pressures decrease with the increase in buoyancy forces. This effect is significant only in the region where two streams are not fully mixed ($x < 60$). Once the two streams are mixed, the effect of buoyancy on the wall pressure is not evident.

14) POD analysis of the unsteady flows establishes the presence of *standing* waves at VR=1 and *travelling* waves at VR = 2.

15) The space–time symmetry of the degenerate pair of modes is utilized to estimate the average translational wave speeds in the unsteady regime at VR = 2.

5.2 Mixing characteristics

The conclusions related to mixing characteristics as follows:

1) The thermal and physical mixing process along *the channel length* can be effectively monitored by the scalar measure termed as 'mixing index' employed in the present work.
2) For the purpose of design and performance assessment of such flow systems, a 'Mixing Length' parameter is proposed in the present work. The parameter is shown to be effective in characterizing the overall mixing process.
3) In the steady flow regime, the Mixing Length is not very sensitive to the two Richardson numbers.
4) For the unsteady periodic flow with standing waves (VR = 1), the mixing process is significantly enhanced with the mixing lengths reducing by almost 70% at (Ri_T + Ri_C) = 3 with respect to the forced flow values. The formation of standing waves lead to a sinuous flow pattern with the fluid particles following a wavy path. This has a two-fold effect; i) an increase in axial and transverse velocity gradients and, ii) a significant increase in residence time. Both of these factors contribute to the enhanced mixing.
5) For steady flow cases in the mixed convection regime, VR = 0.5, gives relatively better rates of both thermal and physical mixing than the other velocity ratios.
6) In the unsteady regime, the formation of waves enhances the rates of mixing significantly. The effect is more for standing waves than the travelling waves.

7) A quantitative measure which quantifies the effectiveness of buoyancy towards controlling the mixing phenomenon, termed as 'Buoyancy Mixing Effectiveness' (e_m) is also proposed. It is defined such that, a positive value of e_m implies that buoyancy improves mixing as compared to the forced flow under similar conditions and vice versa.

8) At VR = 1, for unsteady cases, both thermal and physical Buoyancy Mixing Effectiveness is almost 10 times than that for the steady cases. Further, increase in buoyancy in the unsteady regime, enhances mixing and nearly 60 % increase in effectiveness at $(Ri_T + Ri_C) = 3$ as compared to $(Ri_T + Ri_C) = 2$, is observed.

9) Maximum buoyancy mixing effectiveness of nearly 82 % is obtained for VR = 1 at $Ri_T = 1.5$, $Ri_C = 1.5$ where standing waves are found to exist in the flow. In comparison, for same values of (Ri_T, Ri_C) at VR = 2, the corresponding value of buoyancy mixing effectiveness is nearly 37% where travelling waves are found to exist.

The flow dynamics and the mixing characteristics of the system under consideration have been correlated to the operating parameters as represented by the thermal and concentration Richardson numbers and the bulk velocity ratios of the two jets. It is established that mixing is favored at sufficiently higher Richardson numbers so as to trigger instabilities leading to the formation of waves in the flow. These waves and particularly, the standing waves, greatly enhance the thermal and physical mixing of the two jets quite naturally via an action similar to mechanical mixing / churning effects caused by placing 'Baffles' in the channel. However, baffles, used to create mechanical mixing / churning also cause large pressure drop along the channel length and hence more pumping power is required for such systems. A similar effect is produced naturally in the present mixing system, by the standing / travelling wave instability and also without any

significant increase in the pressure drop along the channel length. Therefore buoyancy can be effectively exploited to design efficient mixing systems with minimum energy loss.

5.3 Recommendations for further study

The present study can be further extended by carrying out the following investigations.

1) The range of Ri_T and Ri_C can be extended to include values greater than 1.5. It would be interesting to explore the dynamics at Ri_T and $Ri_C > 1.5$ as a strong possibility of further bifurcations in the unsatedy flow regimes controlled by the two buoyancy force exists.
2) Similarily, studies can be carried out for Pr and Sc values different than 0.7 and 0.8, to cover a wider application range.
3) Also the values of Pr and Sc number chosen in the present study are nearly same (Le ~ 1.0). It would be interesting to observe the effect of large difference in the values of Pr and Sc on flow dynamics and mixing, as in that case the molecular rates of transport of energy and mass would be different (Le $\neq$ 1.0).
4) More values of velocity ratios can be taken up to obtain a large range of momentum imbalance and its subsequent effect on flow dynamics.
5) The effect of change of Re on flow structure and mixing of the two jets / streams is not considered in the present study. The dynamics at larger values of Re (in both laminar and turbulent regimes) is likely to be different and its effect on mixing can be investigated.
6) The effect of change of channel height (h) on flow structure and subsequent mixing is not investigated in the present problem. Flapping mode instability is reported by Pawlowski et al [44] at larger values of h for isothermal jet interaction

in a channel. It will be interesting to carry out detailed POD analysis of such instability, if it is present, for impingement of non-isothermal jets of different fluids in a channel.

7) A stability analysis of the steady flows can be carried out to gain more insight into the various instabilities encountered.

In addition to these extensions of the present work, some new studies based on similar methodology could be carried out. In this regard the following suggestions are made.

1) Similar investigations in *micro channels* can also be carried out as detailed information regarding the flow dynamics in such geometries is not available in the literature.
2) A *three-dimensional* version of the present study can be carried out as it would be more practically relevant.

References

1. R. Sherman, J. Grob, W. Whitlock, Dry Surface Cleaning Using Carbon Dioxide Snow, J. Vac. Sci. Technol. B 9 (4) (1991) 1970-1977.
2. C. V. Tu, D. H. Wood, Wall Shear Stress Measurements Beneath an Impinging Jet, Exp. Therm. Fluid Sci. 13 (4) (1996) 364-373.
3. M. Bouainouche, N. Bourabaa, B. Desmet, Numerical Study of the Wall Shear Stress Produced by the Impingement of a Plane Turbulent Jet on a Plate, Int. J. Numer. Methods Heat Fluid Flow 7 (6) (1997) 548-564.
4. B. E. Russ, J. B. Talbot, A Method for Measuring the Adhesion Strength for Powder Coatings, J. Adhesion 68 (3-4) (1998) 257-268.
5. D. J. Phares, J. K. Holt, G. T. Smedley, R. C. Flagan, Method for Characterization of Adhesion Properties of Trace Explosives in Fingerprints and Fingerprint Simulations, J. Forensic Sci. 45 (2000) 762.
6. R. Gardon, J. C. Akfirat, The Role of Turbulence in Determining the Heat Transfer Characteristics of Impinging Jets, J. Heat Mass Transfer 8 (1965) 1261-1272.
7. R. Gardon, J. C. Akfirat, Heat Transfer Characteristics of Impinging Two-Dimensional Air Jets, ASME Journal of Heat Transfer 88 (1966) 101–108.
8. H. Miyazaki, E. Silberman, Flow and Heat Transfer on a Flat Plate Normal to a Two-Dimensional Laminar Jet Issuing from a Nozzle of Finite Height, Int. J. Heat Mass Transfer 15 (1972) 2097-2107.
9. E. M. Sparrow, T. C. Wong, Impingement Transfer Coefficients Due to Initially Laminar Slot Jets, Inter. J. Heat Mass Transfer 18 (1975) 597-605.

10. R. P. Van Heiningen, A. S. Mujumdar, W. J. M. Douglas, Numericai Prediction of the Flow Field and Impingement Heat Transfer Caused by a Laminar Slot Jet, Trans. ASME J. Heat Transfer 98 (1976) 654-658.

11. J. H. Masliyah, T. T. Nguyen, Mass Transfer Due to an Impinging Slot Jet, Int. J. Heat Mass Transfer 22 (1979) 237-244.

12. V. K. Garg, S. Jayaraj, Boundary Layer Analysis for Two-Dimensional Slot Jet Impingement on Inclined Plates, Trans. ASME J. Heat Transfer 110 (1988) 577-582.

13. Z. H. Lin, Y. J. Chou, Y. H. Hung, Heat Transfer Behaviours of a Confined Slot Jet Impingement, Int. J. Heat Mass Transfer 40 (5) (1997) 1095-1107.

14. H. Beitelmal, M. A. Saad, C. D. Patel, The Effect of Inclination on the Heat Transfer Between a Flat Surface and an Impinging Two-Dimensional Air Jet, International Journal of Heat and Fluid Flow 21 (2000) 156-163.

15. Y. M. Chung, K. H. Luo, Unsteady Heat Transfer Analysis of an Impinging Jet, Journal of Heat Transfer 124 (2002) 1039-1048.

16. Y. L. Shi, M. B. Ray, A. S. Mujumdar, Effects of Prandtl Number on Impinging Jet Heat Transfer Under a Semi-Confined Laminar Slot Jet, Int. Comm. Heat Mass Transfer 30 (4) (2003) 455-464.

17. Z. Q. Lou, A. S. Mujumdar, C. Yap, Effects of Geometric Parameters on Confined Impinging Jet Heat Transfer, Applied Thermal Engineering 25 (2005) 2687–2697.

18. J. Y. San, W. Z. Shiao, Effects of Jet Plate Size and Plate Spacing on the Stagnation Nusselt Number for a Confined Circular Air Jet Impinging on a Flat Surface, International Journal of Heat and Mass Transfer 49 (2006) 3477–3486.

19. W. Burwash, W. Finlay, E. Matida, Deposition of Particles by a Confined Impinging Jet onto a Flat Surface at Re = 10^4, Aerosol Science and Technology, 40 (3) (2006) 147-156.

20. H. M. Hofmann, R. Kaiser, M. Kind, H. Martin, Calculations of Steady and Pulsating Impinging Jets - An Assessment of 13 Widely Used Turbulence Models, Numerical Heat Transfer, Part B: Fundamentals 51 (6) (2007) 565–583.

21. T. D. Yuan, J. A. Liburdy, T. Wang, Buoyancy Effects on Laminar Impinging Jets, Int. J. Heat Mass Transfer 31 (1988) 2137-2145.

22. K. Ichimiya, Y. Yamada, Three-Dimensional Heat Transfer of a Confined Circular Impinging Jet with Buoyancy Effects, Journal of Heat Transfer 125 (2003) 250-256.

23. D. Sahoo, M. A. R. Sharif, Mixed-Convective Cooling of an Isothermal Hot Surface by Confined Slot Jet Impingement, Numerical Heat Transfer, Part A: Applications 45 (9) (2004) 887-909.

24. W. Zhao, K. Kumar, A. S. Mujumdar, Impingement Heat Transfer for a Cluster of Laminar Impinging Jets Issuing from Noncircular Nozzles, Drying Technology 23 (1) (2005) 105-130.

25. A. Tamir, Impinging Stream Reactors: Fundamentals and Applications (Transport Processes in Engineering), Elsevier, 1994.

26. E. Erkoç, R. J. Santos, M. I. Nunes, M. M. Dias, J. C. B. Lopesa, Mixing Dynamics Control in RIM Machines, Chemical Engineering Science 62 (2007) 5276–5281.

27. M. Kakuta, F. G. Bessoth, A. Manz, Micro-fabricated Devices for Fluid Mixing and Their Application for Chemical Synthesis, The Chemical Record 1 (2001) 395–405.

28. V. A. Denshchikov, V. N. Kontratev, A. N. Romashev, Interaction Between Two Opposed Jets, Fluid Dynamics 6 (1978) 924–926.

29. V. A. Denshchikov, V. N. Kontratev, A. N. Romashev, V. M. Chubarov, Auto-Oscillations of Planar Colliding Jets, Fluid Dynamics 3 (1983) 460–462.

30. N. S. Nosseir, B. Shabtay, Characteristics of Jet Impingement in a Side-Dump Combustor, AIAA Journal 24 (11) (1986) 1752-1757.

31. N. Nosseir, U. Peled, G. Hildebrand, Pressure Field Generated by Jet-on-Jet Impingement, AIAA Journal 25 (10) (1987) 1312-1317.

32. J. C. Rolon, D. Veynante, J. P. Martin, Counter Jet Stagnation Flows, Exps. in Fluids 11 (1991) 313–324.

33. P. Wood, A. Hrymak, R. Yeo, D. Johnson, A. Tyagi, Experimental and Computational Studies of the Fluid Mechanics in an Opposed Jet Mixing Head, Phys. Fluids A 3 (1991) 1362–1368.

34. S. M. Hosseinalipour, A. S. Mujumdar, Comparative Evaluation of Different Turbulence Models for Confined Impinging and Opposing Jet Flows, Numerical Heat Transfer, Part A: Applications 28 (6) (1995) 647 - 666

35. W. P. Jones, B. E. Launder, The Calculation of Low-Reynolds-Number Phenomena with a Two-Equation Model of Turbulence, Int. J. Heat Mass Transfer 16 (1973) 1119-1130.

36. S. M. Hosseinalipour, A. S. Mujumdar, Flow, Heat Transfer and Particle Drying Characteristics in Confined Opposing Turbulent Jets: A Numerical Study, Drying Technology 13 (3) (1995) 753-781.

37. S. M. Hosseinalipour, A. S. Mujumdar, Flow and Thermal Characteristics of Steady Two Dimensional Confined Laminar Opposing Jets: Part I. Equal Jets, Int. Comm. Heat Mass Transfer 24 (1) (1997) 27-38.

38. S. M. Hosseinalipour, A. S. Mujumdar, Flow and Thermal Characteristics of Steady Two Dimensional Confined Laminar Opposing Jets: Part II. Unequal Jets, Int. Comm. Heat Mass Transfer 24 (1) (1997) 39-50.

39. A. Yoshida, An Opposed Jet Burner for the Study of High-Intensity Combustion, Meas. Sci. Technol. 10 (1999) N149–N151.

40. D. A. Johnson, Experimental and Numerical Examination of Confined Laminar Opposed Jets: Part I. Momentum Imbalance, Int. Comm. Heat Mass Transfer 27 (4) (2000) 443-454.

41. D. A. Johnson, Experimental and Numerical Examination of Confined Laminar Opposed Jets: Part II. Momentum Balancing, Int. Comm. Heat Mass Transfer 27 (4) (2000) 455-463.

42. S. J. Wang, A. S. Mujumdar, A Numerical Study of Flow and Mixing Characteristics of Three-Dimensional Confined Turbulent Opposing Jets: Unequal Jets, Chemical Engineering and Processing 44 (2005) 1068–1074.

43. S. J. Wang, S. Devahastin, A. S. Mujumdar, A Numerical Investigation of Some Approaches to Improve Mixing in Laminar Confined Impinging Streams, Applied Thermal Engineering 25 (2005) 253-269.

44. R. P. Pawlowski, A. G. Salinger, J. N. Shadid, T. J. Mountziaris, Bifurcation and Stability Analysis of Laminar Isothermal Counter-Flowing Jets, J. Fluid Mechanics 551 (2006) 117–139.

45. S. Devahastin, A. S. Mujumdar, A Numerical Study of Mixing in a Novel Impinging Stream In-Line Mixer, Chemical Engineering and Processing 40 (2001) 459-470.

46. S. Devahastin, A. S. Mujumdar, A Numerical Study of Flow and Mixing Characteristics of Laminar Confined Impinging Streams, Chemical Engineering Journal 85 (2002) 215-223.

47. S. J. Wang, S. Devahastin, A. S. Mujumdar, Effect of Temperature Difference on Flow and Mixing Characteristics of Laminar Confined Opposing Jets, Applied Thermal Engineering 26 (2006) 519-529.

48. C. M. Rhie, W. L. Chow, Numerical Study of the Turbulent Flow Past an Airfoil with Trailing Edge Separation, AIAA J. 21 (1983) 1525-1532.

49. J. H. Ferziger, M. Peric, Computational Methods for Fluid Dynamics, Springer-Verlag, Berlin, 1996, pp. 95-98.

50. C. Hirsch, Numerical Computation of Internal and External Flows, Wiley Interscience Publication, John Wiley and Sons Ltd., Chap 23, 1990, pp. 661-663.

51. A. A. Amsden, F. H. Harlow, The SMAC Method: A Numerical Technique for Calculating Incompressible Fluid Flows, Los Alamos Scientific Report, LA 4370, 1970.

52. N. Hasan, S. Sanghi, The Dynamics of Two-Dimensional Buoyancy Driven Convection in a Horizontal Rotating Cylinder, J. Heat Transfer 126 (2004) 963-984.

53. L. Cheng, S. Armfield, A Simplified Marker and Cell Method for Unsteady Flows on Non-Staggered Grids, Int. J. for Num. Meth. in Fluids 21 (1995) 15-34.

54. N. Hasan, S. F. Anwer, S. Sanghi, On the Outflow Boundary Condition for External Incompressible Flows: A New Approach, Journal of Computational Physics 206 (2) (2005) 661-683.

55. P. G. Drazin, W. H. Reid, Hydrodynamic Stability, 2nd ed., Cambridge University Press, UK, 2004.

56. P. Holmes, J. L. Lumley, G. Berkooz, Turbulence, Coherent Structures, Dynamical Systems and Symmetry, Cambridge University Press, 1996.

57. A. Papoulis, Probability, Random Variables, and Stochastic Processes, McGraw-Hill, New York, 1965.

58. A. Rosenfeld, A. C. Kak, Digital Picture Processing, Academic Press, New York, 1982.

59. V. R. Algazi, D. J. Sakrison, On the Optimality of the Karhunen-Loève Expension, IEEE trans. Inform. Theory 15 (1969) 319-321.

60. C. A. Andrews, J. M. Davies, G. R. Schwartz, Adaptive Data Compression, Proceedings of IEEE 55 (1967) 267-277.

61. D. H. Gay, W. H. Ray, Application of Singular Value Methods for Identification and Model Based Control of Distributed Parameter Systems, Proc. IFAC Workshop on Model Based Process Control, Atlanta, GA (1988) 95-102.

62. R. W. Preisesendorfer, Principal Component Analysis in Meteorology and Oceanography, Elsevier, Amsterdam, 1988.

63. J. L. Lumley, The Structure of Inhomogeneous Turbulence, Atmospheric Turbulence and Wave Propagation, Nauka, Moscow (1967) 166-178.

64. N. Hasan, S. F. Anwer, S. Sanghi, Natural Convection in a Bottom Heated Horizontal Cylinder, Physics of Fluids 17 (064105) (2005).

65. N. Hasan, S. Sanghi, Proper Orthogonal Decomposition and Low-Dimensional Modelling of Thermally Driven Two-Dimensional Flow in a Horizontal Rotating Cylinder, J. Fluid Mech. 573 (2007) 265–295.

66. A. A. Mishra, N. Hasan, S. Sanghi, R. Kumar, Two-Dimensional Buoyancy Driven Thermal Mixing in a Horizontally Partitioned Adiabatic Enclosure, Physics of Fluids 20 (063601) (2008).

67. B. Podvin, P. L. Quéré, Low-Order Models for the Flow in a Differentially Heated Cavity, Phys. of Fluids, 13 (11) (2001) 3204-3214.

68. L. Sirovich, Turbulence and the Dynamics of Coherent Structures, Part I: Coherent Structures, Proc. Soc. Exp. Stress Anal. 45 (1987) 561.

69. J. L. Lumley, A. Poje, Low-Dimensional Models for Flows with Density Fluctuations, Phys. of Fluids 9 (1997) 2023-2031.

70. D. Rempfer, H. Fasel, Evolution of Three-Dimensional Coherent Structures in a Flat Plate Boundary Layer, J. Fluid Mech. 260 (1994) 351-375.

71. N. Aubry, P. Holmes, J. L. Lumley, E. Stone, The Dynamics of Coherent Structures in the Wall Region of a Turbulent Boundary Layer, J. Fluid Mech. 192 (1988) 115-173.

72. N. Aubry, R. Guyonnet, R. Lima, Spatio-Temporal Symmetries and Bifurcations Via Bi-Orthogonal Decompositions. J. Nonlin. Sci. 2 (1992) 183–215.

Appendix A

The various discretizations schemes employed on a non-uniform structured Cartesian mesh have been obtained by employing the Taylor's series expansions. The five-point central scheme for the second derivatives in the diffusion terms and the five-point central or four-point skewed schemes (upwind schemes) for the convective terms are given in this appendix. These schemes have been employed in the interior of the flow domain. The expressions for the spatial derivatives are given along one of the coordinate directions (x-direction) only. Analogous expressions can be employed for the other coordinate direction.

Let χ represent the flow variable whose derivatives are to be computed at a grid point (i, j). The computational molecule is shown in fig. A.1 along with the standard compass notation. The spatial derivatives of χ in the x-direction at the grid

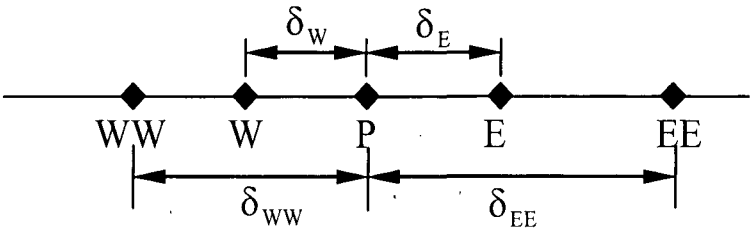

Fig. A.1: Illustration of the computational molecule employed for the different discretisation schemes together with the notation for the different grid spacings

point P can be expressed in terms of their neighbouring values as,

$$D_P(\chi) = \sum_j \eta_j(\chi_j - \chi_P), \quad j = W, E, WW, EE. \tag{A.1}$$

In the above expression η_j are the weights calculated from the grid spacings, χ_j are values of the variable at the neighbouring grid points. The above expression is general in nature and by utilizing suitable values of the weights, the approximations

for the first as well as the second derivatives can be constructed from Eq. (A.1). The values of the weights for the various schemes employed for the first and the second derivatives are given below.

Second derivative central approximations

$$\eta_{WW} = -\frac{2(\delta_{EE}\delta_W - \delta_{EE}\delta_E + \delta_E\delta_W)}{\delta_{WW}(\delta_{WW} - \delta_W)(\delta_{WW} + \delta_{EE})(\delta_{WW} + \delta_E)}$$

$$\eta_W = \frac{2(\delta_{EE}\delta_{WW} - \delta_{EE}\delta_E + \delta_E\delta_{WW})}{\delta_W(\delta_{WW} - \delta_W)(\delta_W + \delta_{EE})(\delta_W + \delta_E)}$$

$$\eta_E = \frac{2(\delta_{EE}\delta_W - \delta_{WW}\delta_W + \delta_{EE}\delta_{WW})}{\delta_E(\delta_{EE} - \delta_E)(\delta_{WW} + \delta_E)(\delta_W + \delta_E)}$$

$$\eta_{EE} = -\frac{2(\delta_E\delta_W - \delta_{WW}\delta_W + \delta_E\delta_{WW})}{\delta_{EE}(\delta_{EE} - \delta_E)(\delta_W + \delta_{EE})(\delta_{WW} + \delta_{EE})}$$

First derivative central and skewed (upwind) approximations

a) Central scheme

$$\eta_{WW} = \frac{2(\delta_{EE}\delta_W\delta_E)}{\delta_{WW}(\delta_{WW} - \delta_W)(\delta_{WW} + \delta_{EE})(\delta_{WW} + \delta_E)}$$

$$\eta_W = -\frac{2(\delta_E\delta_{EE}\delta_{WW})}{\delta_W(\delta_{WW} - \delta_W)(\delta_W + \delta_{EE})(\delta_W + \delta_E)}$$

$$\eta_E = \frac{2(\delta_{EE}\delta_W\delta_{WW})}{\delta_E(\delta_{EE} - \delta_E)(\delta_{WW} + \delta_E)(\delta_W + \delta_E)}$$

$$\eta_{EE} = -\frac{2(\delta_E\delta_W\delta_{WW})}{\delta_{EE}(\delta_{EE} - \delta_E)(\delta_W + \delta_{EE})(\delta_{WW} + \delta_{EE})}$$

b) Upwind scheme

If $u_P > 0$

$$\eta_{WW} = \frac{\delta_W \delta_E}{\delta_{WW}(\delta_{WW} - \delta_W)(\delta_{WW} + \delta_E)}$$

$$\eta_W = -\frac{\delta_E \delta_{WW}}{\delta_W(\delta_{WW} - \delta_W)(\delta_W + \delta_E)}$$

$$\eta_E = \frac{\delta_W \delta_{WW}}{\delta_E(\delta_{WW} + \delta_E)(\delta_W + \delta_E)}$$

$$\eta_{EE} = 0$$

If $u_P < 0$

$$\eta_{WW} = 0$$

$$\eta_W = -\frac{\delta_E \delta_{EE}}{\delta_W(\delta_{EE} + \delta_W)(\delta_W + \delta_E)}$$

$$\eta_E = \frac{\delta_W \delta_{EE}}{\delta_E(\delta_{EE} - \delta_E)(\delta_W + \delta_E)}$$

$$\eta_{EE} = -\frac{\delta_E \delta_W}{\delta_{EE}(\delta_{EE} - \delta_E)(\delta_W + \delta_{EE})}$$